

350

**NASA CONTRACTOR  
REPORT**



**NASA CR-3**

NASA CR-3

198p.

N64 12159 \*

CODE-1  
CR-55104

**EXPLORER VI AND PIONEER V DATA**

**VOLUME I: REDUCTION AND  
ANALYSIS OF DATA**

*by Alan Rosen, Edward J. Smith, C.P. Sonett,  
Eugene W. Greenstadt, R.C. Gore, and W.C. Meecham*

Prepared under Contract No. NASw-270 by  
**SPACE TECHNOLOGY LABORATORIES, INC.**  
Redondo Beach, California  
for

**NATIONAL AERONAUTICS AND SPACE ADMINISTRATION • WASHINGTON, D. C. • OCTOBER 1963**

602 1000  
819 5109

NASA, Washington, D.C.

CONTRACTOR REPORT CR-3

EXPLORER VI AND PIONEER V DATA .

VOLUME I: REDUCTION AND

ANALYSIS OF DATA

By Alan Rosen, Edward J. Smith, C. P. Sonett,  
Eugene W. Greenstadt, R. C. Gore, and W. C. Meecham (*Space Technol.*  
*Labs., Inc., Redondo Beach, Calif.*) Oct. 1963 198p *ref*

(NASA CR-55104; NASA CR-3) *ref*

(NASA)  
Prepared under Contract No. NASw-270) by  
SPACE TECHNOLOGY LABORATORIES, INC.  
Redondo Beach, California

for

NATIONAL AERONAUTICS AND SPACE ADMINISTRATION

CONTRACTOR REPORT CR-3

EXPLORER VI AND PIONEER V DATA  
VOLUME I: REDUCTION AND  
ANALYSIS OF DATA

By Alan Rosen, Edward J. Smith, C. P. Sonett,  
Eugene W. Greenstadt, R. C. Gore, and W. C. Meecham  
Space Technology Laboratories, Inc.

ABSTRACT

12159

A study of the information obtained from the instruments on the Explorer VI earth satellite and the Pioneer V deep space probe is presented. The collection includes: a discussion of the structure, composition and dynamics of radiation belts; an analysis of the observations of the geomagnetic field during magnetic storms; a compilation of Pioneer V data reduction and analysis; an investigation of signal fading in the transmission of the satellites; and fluctuations in signal strength observed in signals received from the satellites caused by ionospheric irregularity. *AUTHOR*

NATIONAL AERONAUTICS AND SPACE ADMINISTRATION

## TABLE OF CONTENTS

	Page
CHAPTER I    The Structure, Composition and Dynamics of the Radiation Belt During August and September 1959 by Alan Rosen	1
CHAPTER II   Explorer VI Satellite Observations of the Geo- magnetic Field During Magnetic Storms by Edward J. Smith and C. P. Sonett	27
CHAPTER III   Pioneer V Data Reduction and Analysis by Eugene W. Greenstadt	101
CHAPTER IV   An Investigation of Signal Fading in Explorer VI and Pioneer V Transmissions by R. C. Gore	117
CHAPTER V    Satellite Signal Fluctuation Caused by Iono- spheric Irregularity by W. C. Meecham	167



CHAPTER I

STRUCTURE, COMPOSITION, AND DYNAMICS OF THE RADIATION BELT  
DURING AUGUST AND SEPTEMBER, 1959

by

Alan Rosen

## I. INTRODUCTION

Four radiation detectors, on the Explorer VI earth satellite were used to determine the characteristics of particles trapped in the Van Allen radiation belt. Some of the results obtained from these detectors during the lifetime of the satellite (August 7 to October 6, 1959) have been discussed in detail by Rosen and Farley<sup>1,2</sup>, Farley and Rosen<sup>3</sup>, Farley and Sanders<sup>4</sup>, Arnoldy, Hoffman and Winckler<sup>5</sup>, and Fan, Meyer and Simpson<sup>6</sup>.

The orientation of the Explorer VI orbit relative to the earth and sun is shown in Figure 1 where ecliptic coordinates have been employed. The Explorer VI orbit was highly elliptic with an apogee of 48,800 km (7.5 earth radii) and a perigee of 6620 km. The period of rotation was 12-3/4 hours. The plane of the orbit was inclined at an angle of 47 degrees with respect to the geographic equatorial plane. The semimajor axis was inclined downward below the equatorial plane at an angle of 25 degrees so that the payload spent most of its period at southerly latitudes. With respect to the earth-sun direction, apogee was located on the evening side of the earth at approximately 2100 hours local time.

This orbit had the advantage of an extremely high apogee which greatly exceeded those of previous earth satellites. This enabled measurements to be made twice daily throughout most of the trapped radiation region. In addition, particle and field measurements carried out at high altitudes were in a region where a transition to interplanetary conditions might be expected.

## II. THE STRUCTURE OF THE RADIATION ZONES

The radiation detectors on Explorer VI, consisting of a Geiger counter, a proportional counter, an ionization chamber and scintillation

# EXPLORER VI ORBIT

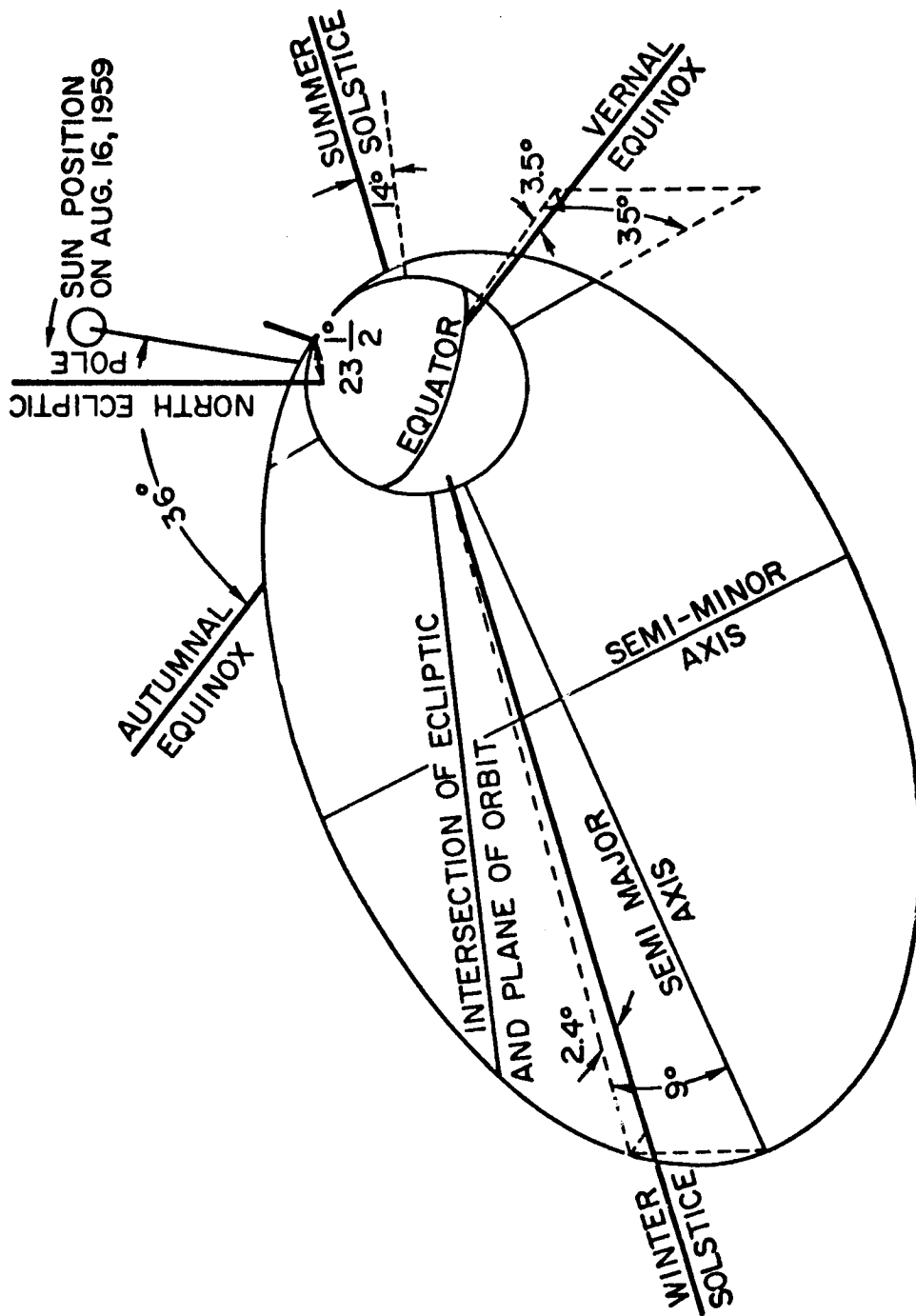


Figure 1. The Orbit of Explorer VI.



counter were calibrated prior to installation in the payload in order to determine their temperature response and energy response. In addition, since the scintillation counter efficiency was high at energies greater than 200 kev, a saturation response curve was taken prior to launch. Extensive calibration to determine the response of these four detectors to monoenergetic electrons were made with a spare set of detectors when installed in position in a spare payload. A composite plot of the efficiencies of the four detectors as a function of energy has been given by Arnoldy, Hoffman and Winckler (see JGR 67; 2595). The most noteworthy characteristics of the instruments are summarized in the following table.

TABLE I

Ratio of Efficiencies (Counts/Electron/cm<sup>2</sup>) for the Four Detectors  
As a Function of Energy

<u>Energy Range</u> <u>kev</u>	<u>Scint/GM</u>	<u>Scint/Prop</u>	<u>Prop/GM</u>	<u>Ion/GM</u>
40	2000	20,000	$10^{-1}$	$2.5 \times 10^{-2}$
50 - 100	500	2,600	$1.5 \times 10^{-1}$	$2 \times 10^{-3}$
100 - 200	26	150	$2.5 \times 10^{-1}$	$5 \times 10^{-4}$
200 - 500	100	100	1.0	$2.5 \times 10^{-4}$
500 - 1000	5000	500	8.3	$2.5 \times 10^{-4}$
1000 - 2000	1500	50	30	$10^{-1}$
2000 - 4000	5	25	$2 \times 10^{-1}$	$5 \times 10^{-4}$

It should be noted that although bremsstrahlung from electrons below about 200 kev could not in theory produce counts in the scintillation

counter, sufficiently high intensities of low-energy photons could cause pulse pile-up above its threshold. The omnidirectional electron fluxes required to produce the count rates observed in the outer zone on a quiet, prestorm day were calculated from these measurements, and were as follows: at 40 kev,  $2 \times 10^{12}$  electrons/cm<sup>2</sup> sec; at 60 kev,  $6 \times 10^{11}$  electrons/cm<sup>2</sup> sec; at 85 kev,  $3 \times 10^{11}$  electrons/cm<sup>2</sup> sec. Below 220 kev the efficiency of the scintillation counter is determined exclusively by pulse pile up. The characteristics of the ratios of efficiencies of the various instruments on Explorer VI may be summarized as follows. For electrons of 40 kev and below, the scint/GM and scint/prop ratios achieve their maximum values. These ratios decrease with increasing energy until the 500 kev scintillation counter threshold is reached. The ratios again increase in the energy range of 500 to 1500 kev however the peak value is never as high as that attained in the 0 to 50 kev energy range. At energies sufficiently high so that the GM counter responds to electrons directly, the ratios again decrease.

The following is a qualitative discussion of the dynamics of the outer radiation before, during and after the magnetic storm of August 16, 1959. The count rate  $R$  observed by any of the detectors on Explorer VI is given by

$$R = \int_0^{\infty} \frac{dJ}{dE} \epsilon(E) dE$$

where  $J(E)$  is the omnidirectional integral spectral distribution, and  $\epsilon(E)$  is the efficiency of detection of electrons for a given instrument. In the forthcoming discussion it will be assumed that the qualitative response of a given detector is predominantly from electrons in one of the energy ranges

tabulated in Table I. Then the count rate in a given energy range  $\Delta E$ , is given by

$$R_{\Delta E} = \left( \frac{\Delta J}{\Delta E} \Delta E \right) \epsilon(E) ,$$

and the ratio of two of the count rates observed by two detectors, e.g. the scintillation counter and Geiger counter is given by the ratio of the efficiencies of the two instruments

$$\frac{\text{scin}}{\text{GM}} = \frac{\epsilon(E)_{\text{scint}}}{\epsilon(E)_{\text{GM}}}$$

### III. PRIOR TO THE GEOMAGNETIC STORM OF AUGUST 16, 1959

During the lifetime of the Explorer VI earth satellite (August 7 to October 6, 1959) five magnetic storms were observed. Data taken during the storm of August 16, 1959 is most complete and therefore that storm shall be discussed. The period from August 7 to August 16 was relatively quiet. Figure 1a shows the count rates observed by the various radiation detectors on the Explorer VI earth satellite on August 16, 1959 prior to the sudden commencement of the magnetic storm. The data shown is typical of the period of August 7 to August 16. (See Volume II, A Compendium of Scintillation Counter Data.) A study of the ratios of the various instruments lead to the following conclusions.

3 Mev the Prop/GM efficiency increase steadily in going from 50 kev to 3 Mev. This ratio is therefore an excellent measure of the electron energy spectrum. Since this ratio increases to a peak at 22,000 km and then decrease again, the spectrum of electrons must harden at 22,000 km and soften at both higher and lower altitudes (see Table II). The Scin/GM and Scin/Prop ratio are consistant with such an interpretation and may furthermore be used to determine the degree of softness of the spectrum. From Table II, it is noted that the Scin/Prop ratio approaches 3000 at 28,000 kilometers. Table I indicates that such high ratios can only be achieved for energies below the scintillation counter threshold. The only possible interpretation consistent with the observed ratios is that at 28,000 km electrons of 100 kev average energy predominate. Furthermore, the intensity of these must be of the order of  $10^{11}$  electrons/cm<sup>2</sup> sec. At 22,000 km 1 Mev type electrons exist, whereas at 18,000 km the average electron energy is of the order of 400 kev.

#### IV. DURING THE GEOMAGNETIC STORM OF AUGUST 16, 1959

Figure 2 shows a comparison of the particle flux seen by the scintillation counter on passes 17 and 18, both on August 16, in the outer Van Allen zone. Pass 18 shows a very unusual amount of structure in the particle flux and a modest increase in peak intensity - evidence that new particles have appeared in the geomagnetic field at distances beyond approximately 3 earth radii. This increase in peak intensity, taking place during the main phase of the magnetic storm, is quite small compared with the 20-fold increase that had occurred by pass 21 on August 18. It is important to note however, that there is no net decrease in peak intensity in the outer zone of particles to which the scintillation counter is

PASS 17 16 AUGUST 1959  
0230-0515

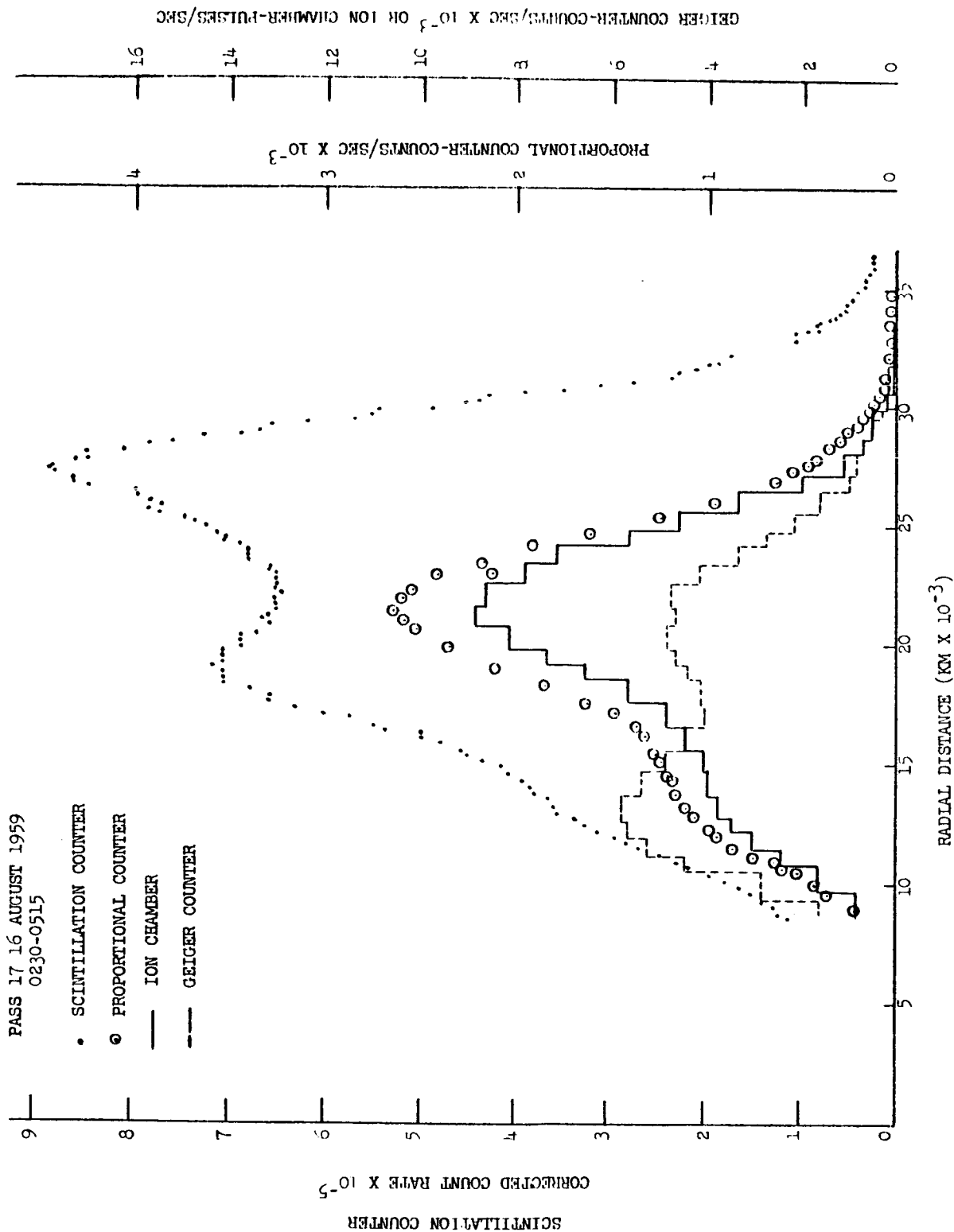


Figure 1a. The Count Rates from the Four Radiation Detectors Prior to the Magnetic Storm of August 16, 1959.

1. It is not possible to account for the observed ratios as a function of altitude with an unchanging spectrum. Either the spectrum hardens or softens or the composition of the trapped radiation changes in going from 15,000 to 30,000 kilometers radial distance.

2. In going from 15,000 km to 30,000 km radial distance, the energy spectrum of electrons must first harden and then become extremely soft. If the major contribution to the various detectors were electrons of energy greater than 3 Mev then the scin/GM ratio would become of the order of 10. It is only at low altitudes (see Table II) where the ratio

TABLE II

Ratios of Count Rates Observed by the Radiation Detectors  
for Pass 17 August 16 (Refer to Figure 2)

<u>Radial Distance Ratio</u>	<u>13,000 km</u>	<u>18,000 km</u>	<u>22,000 km</u>	<u>28,000 km</u>
$\frac{\text{Scin}}{\text{GM}}$	63	150	130	1100
$\frac{\text{Scin}}{\text{Prop}}$	320	340	240	2900
$\frac{\text{Prop}}{\text{GM}}$	0.2	0.4	0.5	0.35
$\frac{\text{Ion}}{\text{GM}}$	$7 \times 10^{-4}$	$15 \times 10^{-3}$	$2 \times 10^{-3}$	$10^{-2}$

even approaches this value. Thus we assume that a radial distances greater than 15,000 km the predominant contribution to the various detectors is from electrons of energy less than 3 Mev. At energies below

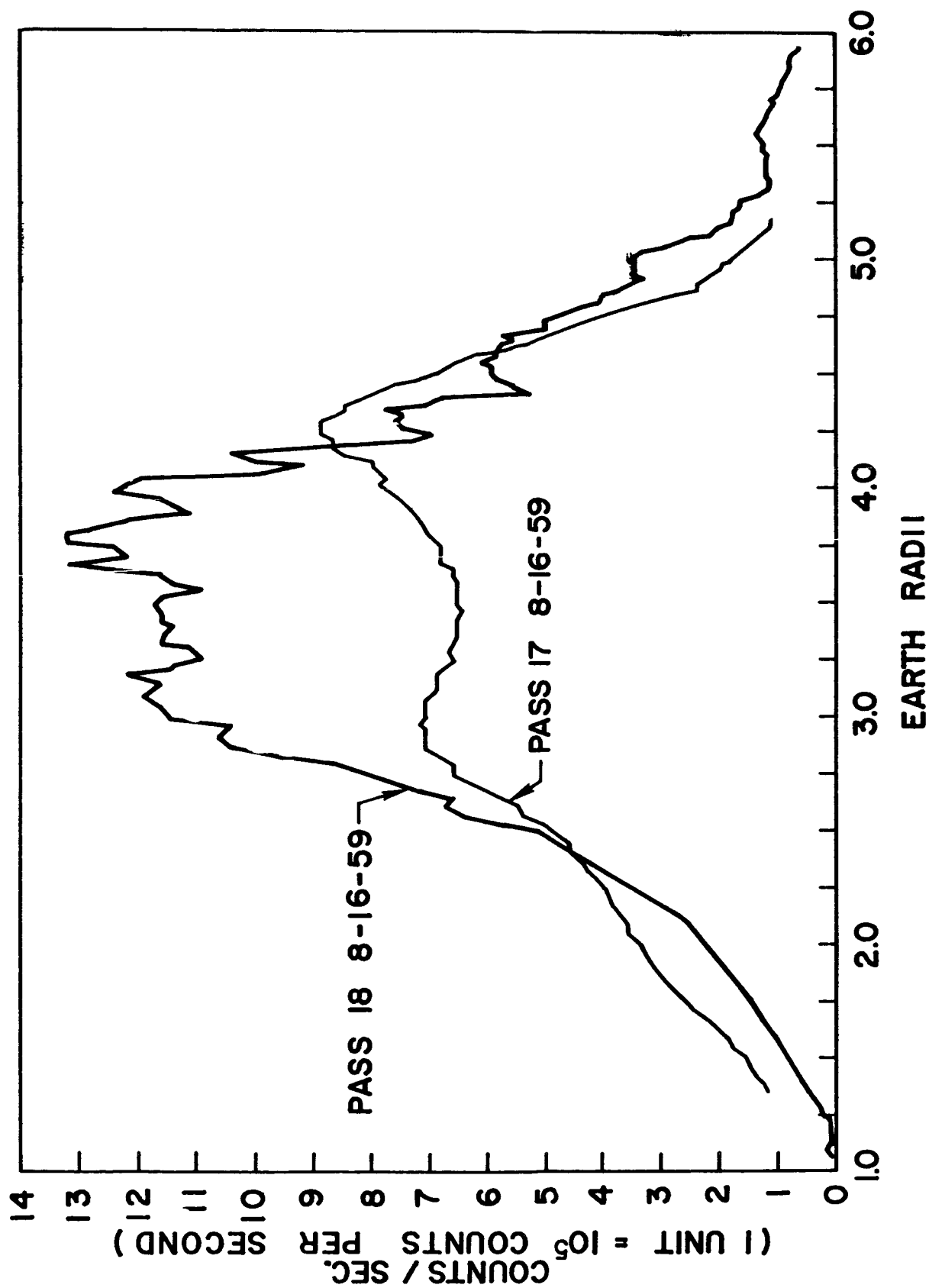


Figure 3 Comparison of Scintillation Counter Particle Fluxes for the 17th and 18th passes.

sensitive at any time during the storm, although there is a decrease at radial distances beyond the position of peak intensity. This may be contrasted with the results of Arnoldy, Hoffman, and Winckler (1960) and Fan, Meyer, and Simpson (1960), shown in Figure 3 who observe a decrease in the peak intensity of bremsstrahlung from electrons.

Since the instruments on this satellite sensitive to bremsstrahlung from electrons see a decrease in peak intensity, the increase in peak intensity seen by the scintillation counter may be accounted for by an increase of protons above 2 Mev in the geomagnetic field. However, the observed scintillation counter counting rate after the storm was  $1.8 \times 10^7$  counts/sec. Assuming this rate was due to protons of energy greater than 2 Mev, the particle energy density associated with these particles would exceed the energy density of the geomagnetic field. Thus it is unlikely that 2 Mev protons could give rise to the observed rates. If we assume the various detectors are responding to electrons, the count rate ratios lead to the hypothesis that the increase observed by the scintillation counter, while the proportional counter and Geiger counter both see a decrease, must be due to an influx of low energy electrons to radial distances of approximately  $3 R_e$ . Table III presents the ratios observed by the radiation detection instruments during pass 19 of the satellite. The most striking change is observed in the Scin/GM and Scin/Prop counter ratio at the radial distance of approximately 20,000 km. ( $3 R_e$ ) Indeed these ratios, observed at 20,000 kilometers are comparable to the ratios observed before the storm (see Table II) at 28,000 km. It is therefore proposed that during the geomagnetic storm a large influx of electrons of average energy 50-100 kev



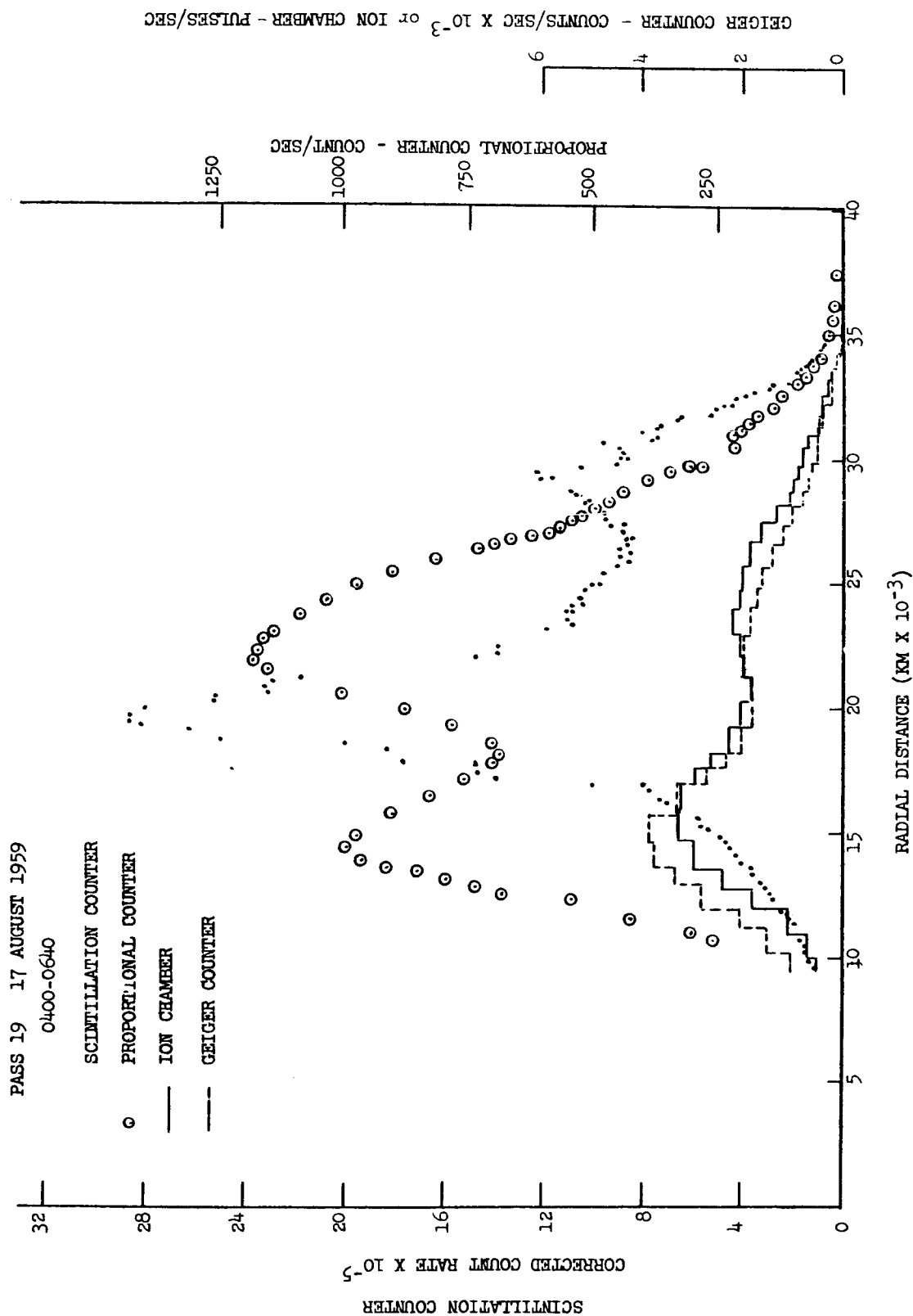


Figure 3. The Count Rates from the Four Detectors During the Magnetic Storm of August 16, 1959.

TABLE III

Ratios of Count Rates Observed by the Radiation Detectors forPass Number 19

Radial Distance Ratio	<u>15,000 km</u>	<u>20,000 km</u>	<u>22,000 km</u>	<u>26,000 km</u>	<u>30,000 km</u>
$\frac{\text{Scin}}{\text{GM}}$	120	1600	790	515	2800
$\frac{\text{Scin}}{\text{Prop}}$	450	3400	1250	1050	3400
$\frac{\text{Prop}}{\text{GM}}$	0.27	0.48	0.63	0.49	0.84
$\frac{\text{Ion}}{\text{GM}}$	$0.74 \times 10^{-3}$	$1.1 \times 10^{-3}$	$1 \times 10^{-3}$	$1.1 \times 10^{-3}$	$1.1 \times 10^{-3}$

penetrated the geomagnetic field to a radial distance of approximately  $3 R_e$ . Below  $3 R_e$  the changes in the trapped radiation are small. The decrease in count rates, seen by the Geiger counter and proportional counter may be accounted for by permitting a very small fraction of the 1-2 Mev electrons to be lost from the radiation belt. Indeed, since the efficiencies of these instruments for detection of 1 Mev electrons is of the order of  $10^8$  the efficiency for detection of 50 kev electrons, compared to  $10^4$  for the scintillation counter, an influx of  $10^{11}$  electrons/cm<sup>2</sup> sec of energy greater than 50 kev, would be equivalent to a loss of  $10^3$  electrons/cm<sup>2</sup> sec of energy greater than 1 Mev.

#### V. AFTER THE GEOMAGNETIC STORM OF AUGUST 16

The peak intensities observed in the outer radiation zone with the scintillation counter and proportional counter telescope, before, during and after the geomagnetic storm are shown in Figures 4 and 5. The scintillation counter maximum intensity is sometimes at the first outer zone peak and sometimes it is at the second outer zone peak, although the difference in peak heights is always small. While the uncertainties in the reconstruction of the intensity curves and the uncertainty in the estimate of the efficiencies for particles of various energies do not permit accurate measurements of the particle flux, the relative day-to-day changes are probably quite well represented in Figure 4. For example, the alternate increase and decrease in peak intensity starting with pass 20 was at least partly the result of traversals alternately at high and low geomagnetic latitudes. Since the period of the satellite was just slightly greater than 12 hours, consecutive passes differ in geographic longitude by approximately  $180^\circ$ . Therefore, the magnetic dipole axis was alternately tipped toward the satellite (high geomagnetic latitude pass) and away from the satellite (low latitude pass).

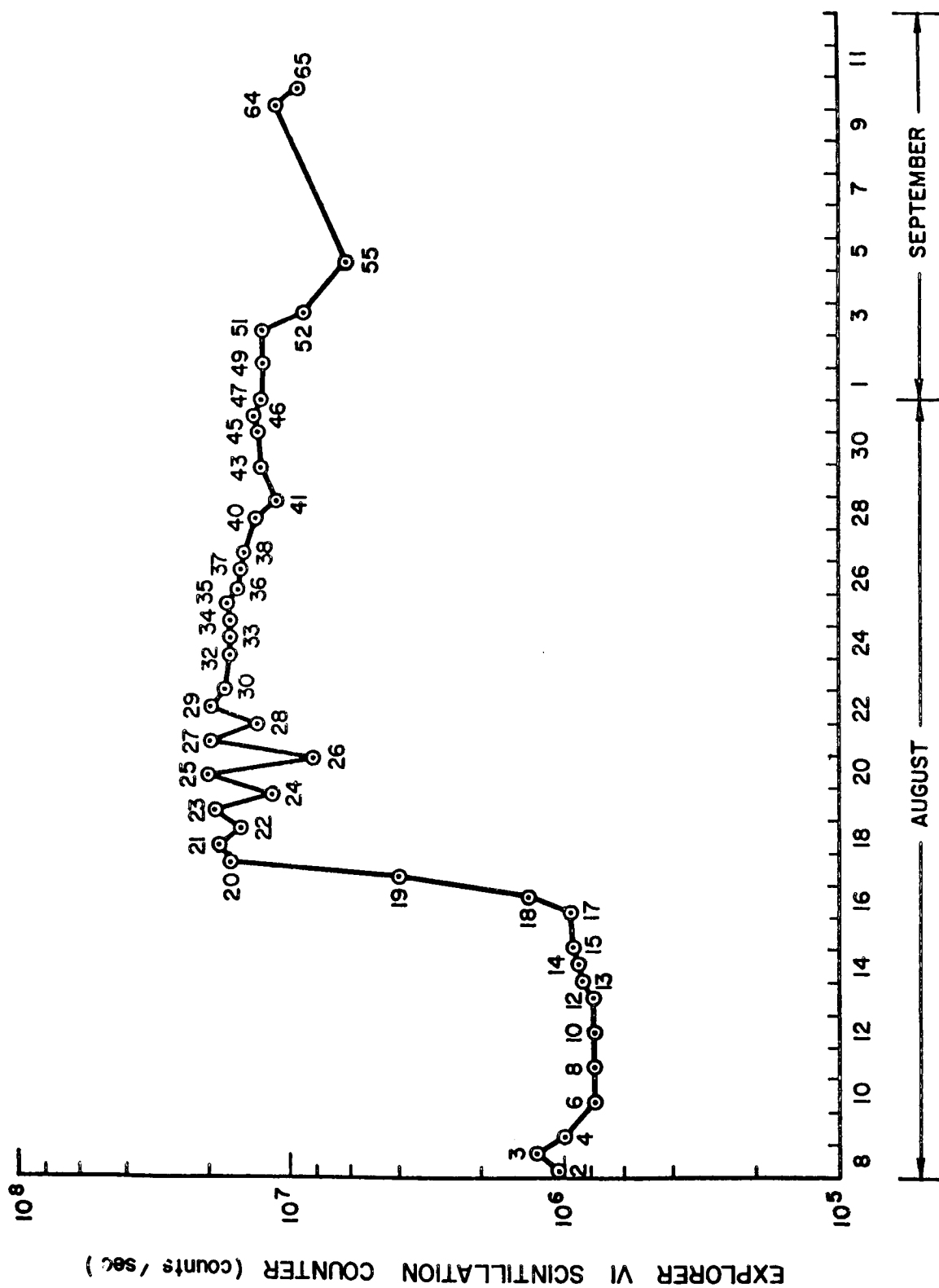


Figure 4. Peak Count Rates in the Outer Zone as Observed with the Explorer VI Scintillation Counter.

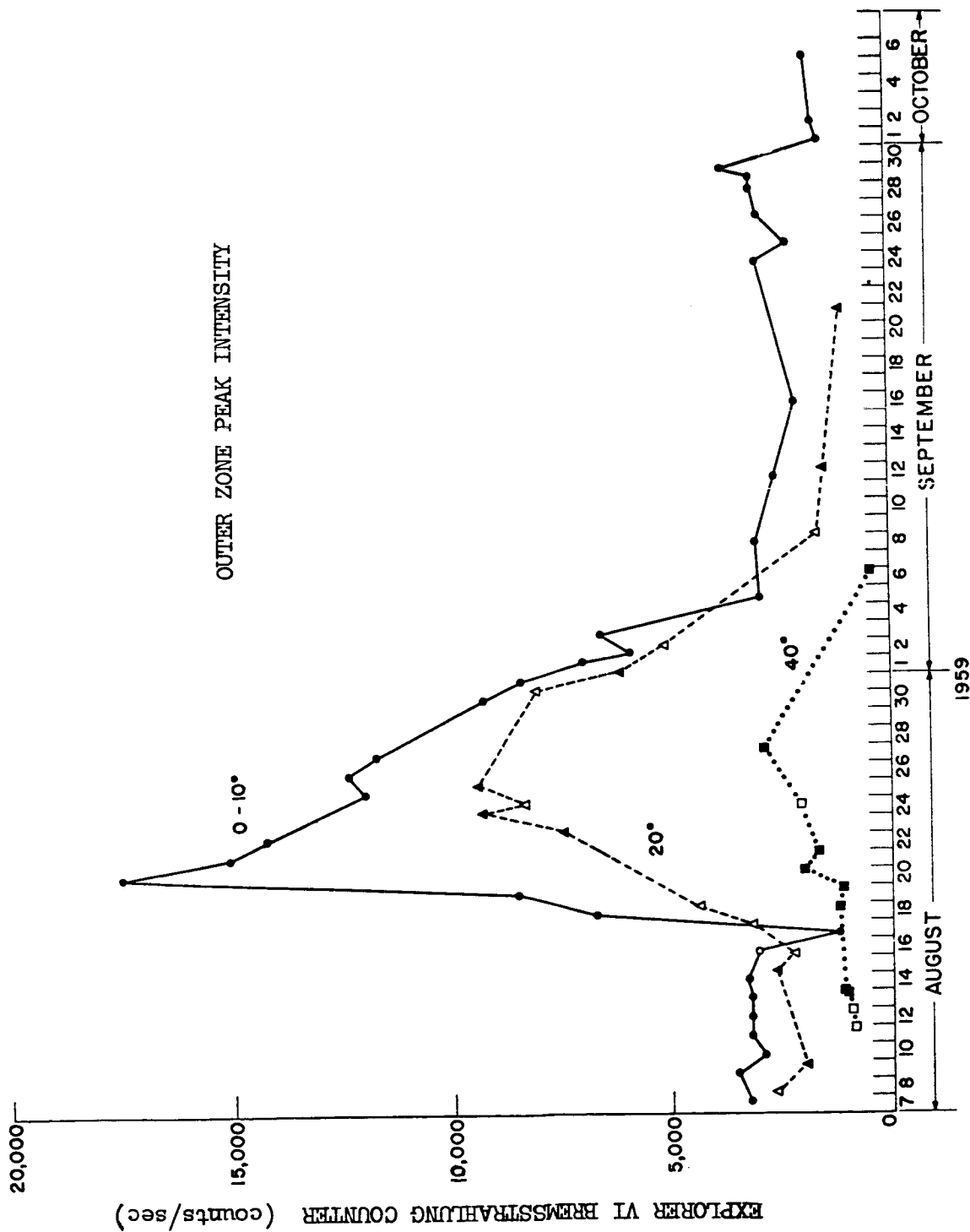


Figure 5. Peak Count Rates in the Outer Zone As Observed with the Explorer VI Proportional Counter.

A few days later, because the satellite period was incommensurate with the earth's period, the magnetic axis was tipped to the side on each traversal, and both passes were at intermediate geomagnetic latitudes. The low latitude passes produced the high count rates, and the high latitude passes, the low ones. The appearance of such expected effects supports the validity of the reconstruction of the peak intensities from the saturation curve.

The outer zone peak intensities shown in Figure 5 are separated for traversals near the equatorial plane and at high latitudes. It is apparent that the maximum increases and decreases for the August 16 storm occurred in the equatorial plane. Furthermore, a comparison of the intensities shown in Figure 4 with those shown in Figure 5 indicates that the decay in peak intensity after the storm was much more pronounced in the particles seen by the proportional counter than in the particles seen by the scintillation counter. A qualitative interpretation of the spectral character of the radiation after the geomagnetic storm may be obtained by examining the ratios of count rates of the various detectors. The ratios shown in Table IV were determined from data shown in Figures 6, 7 and 8. The scin/GM and ion/GM ratios were obtained from pass number 21 while the scin/prop ratio was obtained from the data of pass number 25. In evaluating the ratios tabulated, the general structure of the outer radiation zone as seen by the various detectors should be taken into consideration. During pass number 21, the structure apparent in the outer zone (the bi-furcation of the peak intensities) prior to the geomagnetic storm is discernable in both the scintillation counter data and the Geiger counter, ion chamber data. On pass number 22, however, the structure has disappeared and only one peak is observed in the outer zone by the two instruments (see Figure 7).

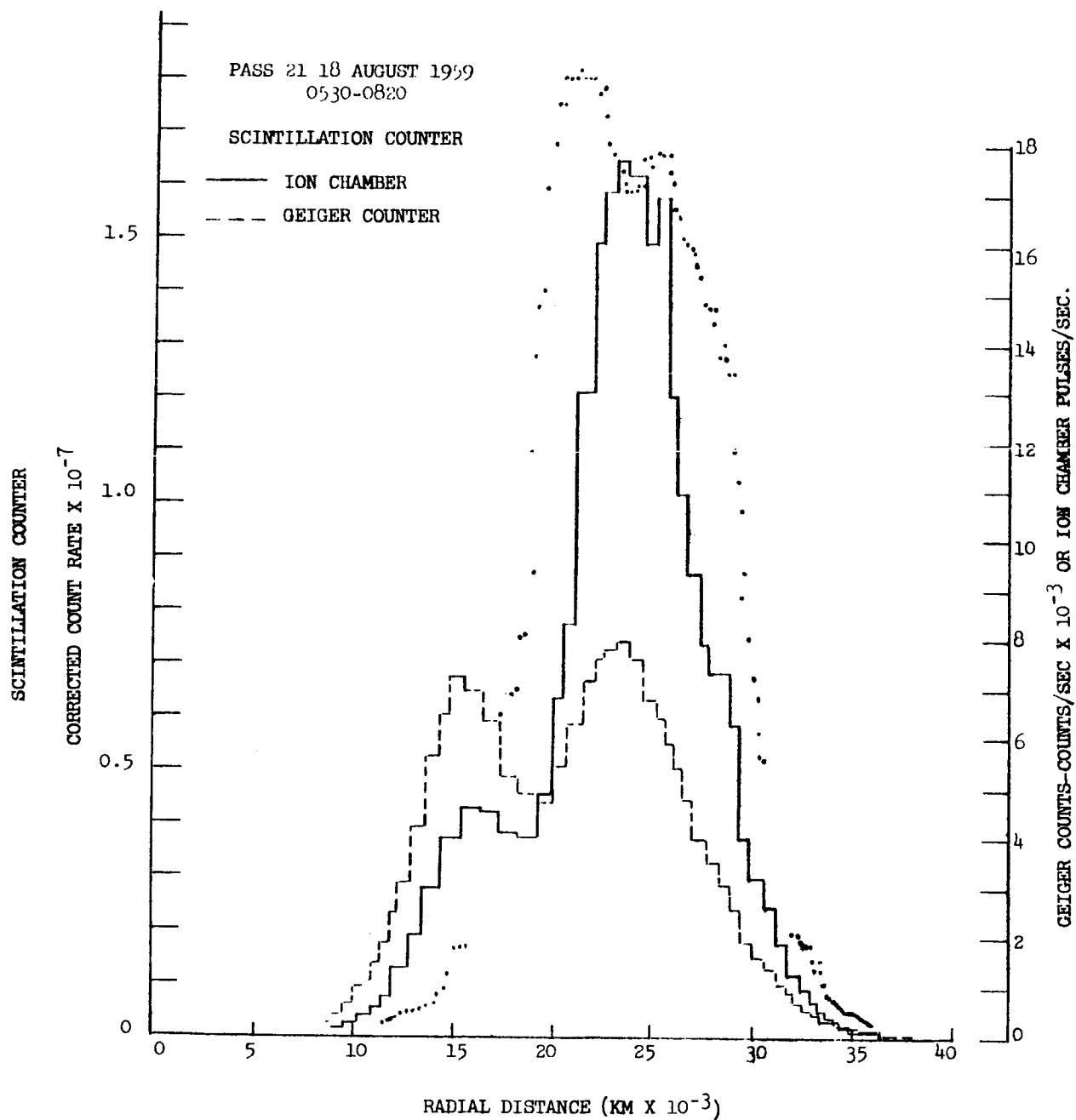


Figure 6. The Count Rates Observed by Three Radiation Detectors on Explorer VI During Pass Number 21.

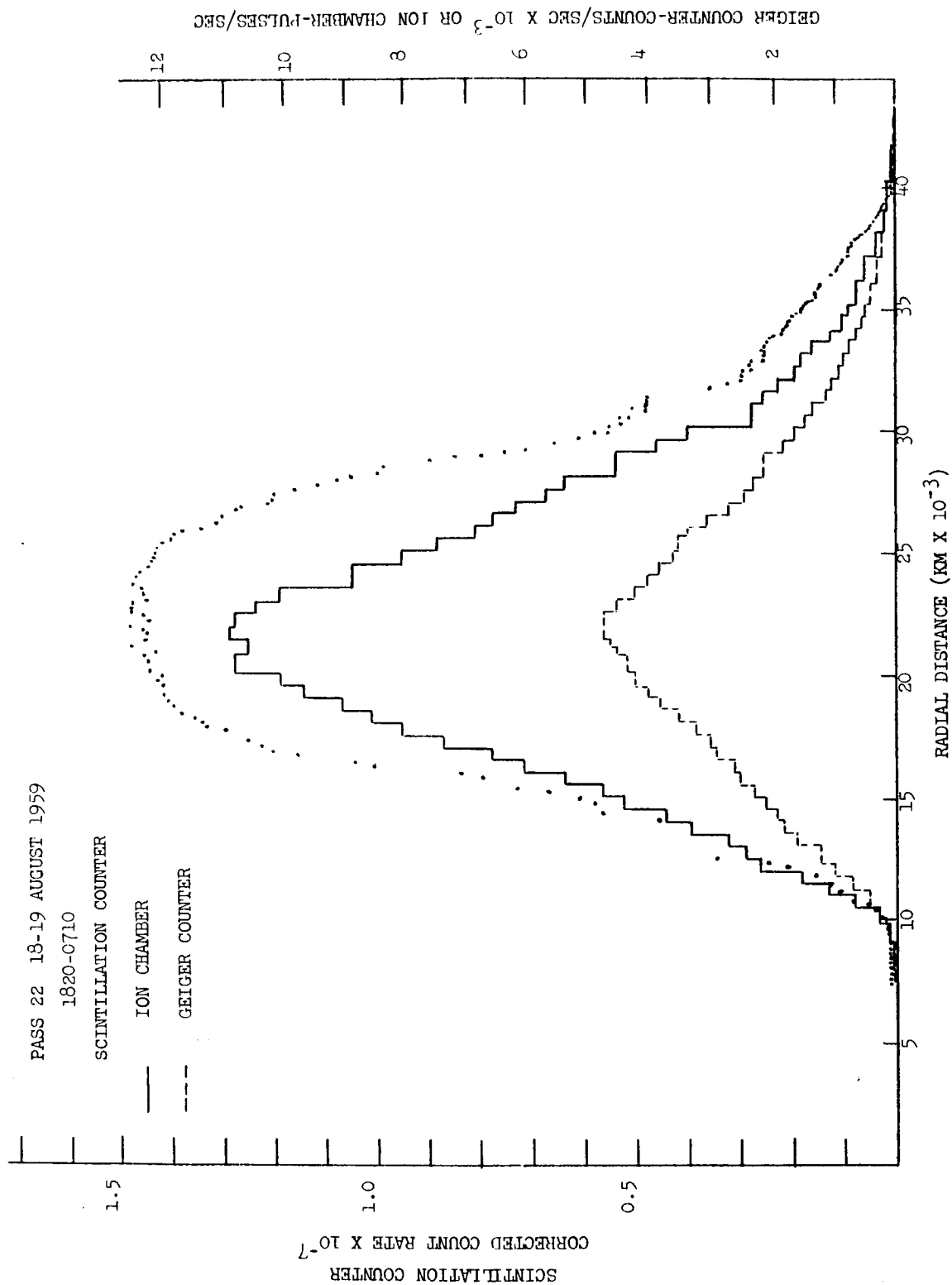


Figure 7. The Count Rates Observed by Three Radiation Detectors on Explorer VI During Pass Number 22.



PASS 25  
20 AUGUST 1959

△ SCINTILLATION COUNTER

○ PROPORTIONAL COUNTER

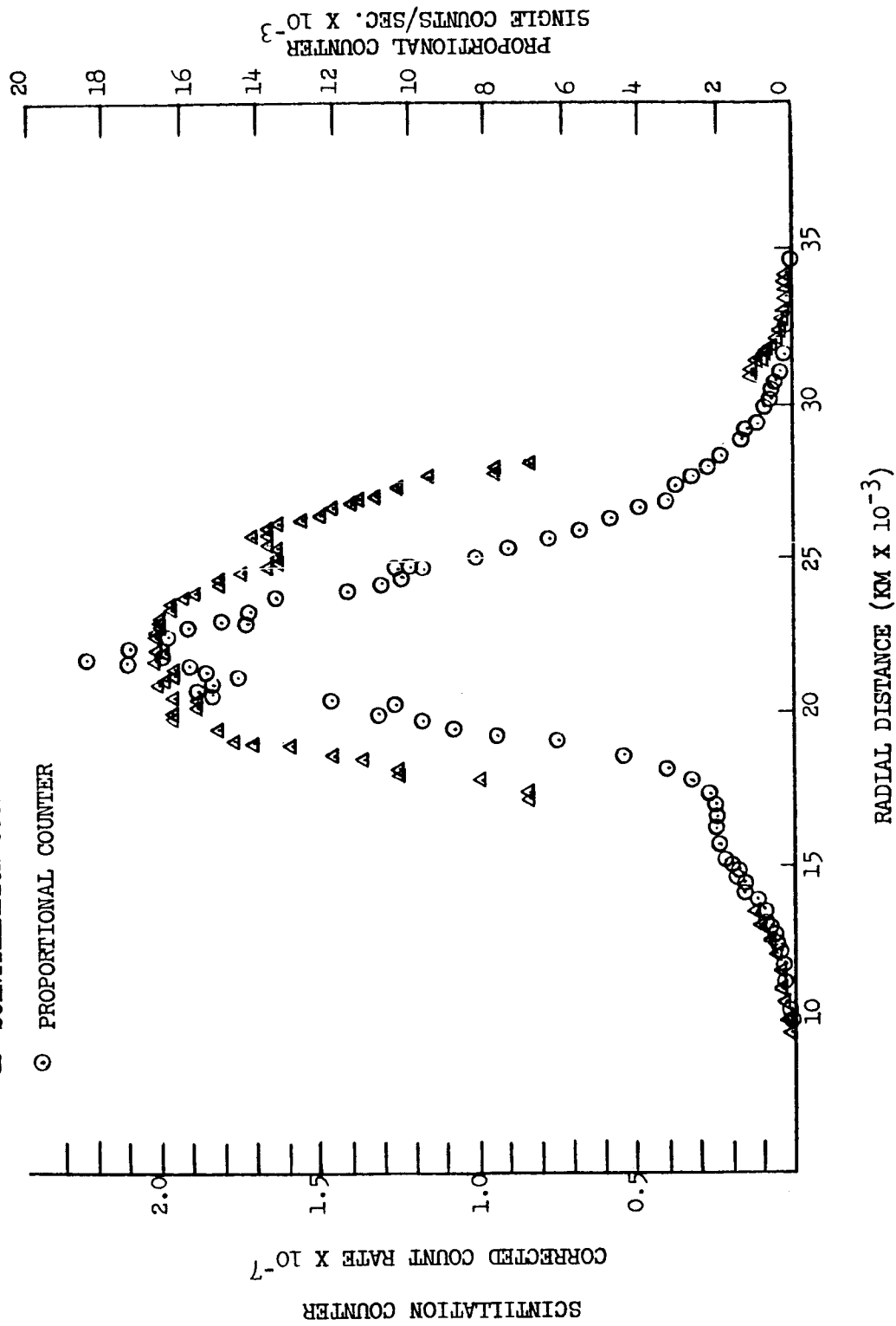


Figure 8. The Count Rates Observed by the Scintillation Counter and Proportional Counter During Pass Number 25.

TABLE IV

Ratios of Count Rates Observed by the Scintillation Counter,

Geiger Counter and Ion Chamber for Pass Number 21;

and the Scintillation Counter and Proportional Counter for Pass Number 25

Radial Distance Ratio	<u>15,000 km</u>	<u>21,000 km</u>	<u>25,000 km</u>	<u>26,000 km</u>	<u>30,000 km</u>
$\frac{\text{Scin}}{\text{GM}}$	400	1400 - 2250	930	---	4400
$\frac{\text{Ion}}{\text{GM}}$	$1.7 \times 10^{-3}$	$(0.5-0.8) \times 10^{-3}$	$.5 \times 10^{-3}$	---	$2 \times 10^{-3}$
$\frac{\text{Scin}}{\text{Prop}}$	1300	1300	1700	3400	1300

Furthermore, for the first time the positions of the peaks as seen by the two detectors seem to coincide. By August 20, during pass number 25, a slight bi-furcation, similar to the structure observed prior to the geomagnetic storm is apparant in the scintillation counter data, but not the proportional counter data. The position of the scintillation counter peak is still coincident with the position of the proportional counter peak. The ratios in Table IV are tabulated at the peaks and valleys in intensity as determined by the various instruments. The high scin/prop ratio can only be accounted for by electrons in the 20 to 40 kev energy range. These same electrons could also account for the high scin/GM ratio observed after the storm. Since this is the only consistent interpretation of the various ratios it is apparent that during pass 21, the scintillation counter peak at 30,000 km consisted of very soft electrons (the predominant contribution was from the 20 to 40 kev range). During pass 22, the 30,000 km peak was no longer discernible. At 21,000 kilometers the scin/GM ratio was of the order of 3,000, whereas during pass number 21 the ratio was approximately 1,800. The scin/prop ratio was a maximum at 26,000 kilometers during pass number 25, at the time when the bi-furcation of the outer zone peaks was becoming apparent in the scintillation counter data.

VI. DYNAMICS OF THE RADIATION ZONES ASSOCIATED WITH THE AUGUST 16, 1959  
MAGNETIC STORM

Before the storm of August 16, 1959, the radiation detectors on Explorer VI responded to two groups of electrons; a group characterized by an energy of approximately 1 Mev, and a second group characterized by an energy of approximately 50 kev. The intensity of the 1 Mev group reaches a peak at approximately 20,000 kilometers. At altitudes greater than 22,000

kilometers the 50 kev group begins to predominate and the scintillation counter response is due predominantly to that group.

During the geomagnetic storm a large influx of electrons of average energy 50-100 kev penetrate the geomagnetic field to a radial distance of approximately  $3 R_e$ . At the same time the 1 Mev group of electrons is depleted from the outer radiation zone. The build up in the low energy electron group continues during and after the geomagnetic storm, until it is no longer possible to distinguish between the two groups with the detectors on Explorer VI. After a few day, the bifurcation in the outer zone peaks is again discernable and the radiation detectors begin to respond to a more energetic component at lower altitudes. The radiation is however compressed so that the peak which was observed at 30,000 km prior to the storm is now located at 26,000 km radial distance.

The intensity of the low energy component prior to the geomagnetic storm should be approximately  $10^{12}$  electrons/cm<sup>2</sup> sec, in order to account for the ratios of count rates seen by the various instruments. During, and immediately after the storm the intensity of the low energy component would have to be in the order of  $10^{15}$  electrons/cm<sup>2</sup> sec with an average energy of approximately 30 kev. Even though the energy density associated with these intensities begin to approach the magnetic energy density of the geomagnetic field, such intensities cannot be excluded on these grounds since perturbations of the surface which may have been due to these particles may have occurred during this period.

It is difficult to reconcile these observations with the data obtained from instruments on the Explorer XII earth satellite. Pending a more thorough investigation, the most likely explanation is that the radiation belt structure changed appreciably in the period between August 1959 and September 1961.

## REFERENCES

1. Rosen, A., and T. A. Farley, "Characteristics of the Van Allen Radiation Zones as Measured by the Scintillation Counter on Explorer VI," J. Geophys. Research 66 (7), 2013 - 2028, 1961.
2. Rosen, A., T. A. Farley and C. P. Sonett, "Soft Radiation Measurements on Explorer VI Earth Satellite," Proceedings of the COSPAR Space Symposium, North Holland Publishing Company, Amsterdam, 1960.
3. Farley, T. A., and A. Rosen, "Charged Particle Variations in the Outer Van Allen Zone During a Geomagnetic Storm, J. Geophys. Research, 65, 3494-3496, 1960.
4. Farley, T. A., and W. L. Sanders, "Pitch Angle Distributions and Mirror Point Densities in the Outer Radiation Zone," J. Geophys. Research, 67, 2159-2168, 1962.
5. Arnoldy, R. L., R. A. Hoffman, and J. R. Winckler, "Observations of the Van Allen Radiation Regions During August and September 1959, Part I." J. Geophys. Research, 65 (5), 1361-1376, 1960.
6. Fan, C. Y., P. Meyer, and J. A. Simpson, "Dynamics and Structure of the Outer Radiation Belt," J. Geophys. Research, 66 (9), 2607-2640, 1961b.

CHAPTER II

EXPLORER VI SATELLITE OBSERVATIONS OF THE  
GEOMAGNETIC FIELD DURING MAGNETIC STORMS

by

Edward J. Smith

and

C. P. Sonett

## INTRODUCTION

Satellite magnetic field data were obtained by Explorer VI during a severe magnetic storm, at geocentric distances between 4 and 8  $R_E$  (earth radii). The examination of these data is restricted to questions concerning the gross characteristics of the large scale magnetic field surrounding the earth during the storm. Consideration of local storm features, such as rapid field variations, is deferred to a subsequent publication. Comparisons are made between (1) the time dependence of the distant geomagnetic field and the surface field during the storm and (2) the gross features of the distant field during storm and non-storm intervals. Long period variations in the distant field will also be compared with variations in the intensity of the outer radiation zone during the storm. Our purpose has been to develop a general description of the large scale storm field from the experimental data. The physical origin of the storm field is also investigated, including the possible existence of a main phase ring current.

There are obvious advantages in studying the behavior of the storm field at the surface and at large radial distances simultaneously, since the solar effects responsible for geomagnetic storms can be strongly modified by a complicated interaction with the earth's outer atmosphere. However, space probes, Pioneer I, Luniks I and II, and Pioneer V, (Sonett, Judge, Sims, and Kelso, 1960; Krassovsky, 1960; Coleman, Sonett, Judge, and Smith, 1960) made single traversals of the distant geomagnetic field during non-storm intervals. Vanguard III (apogee,  $\sim 10,000$  kilometers) produced field measurements above the ionosphere during an interval which included several moderate magnetic storms (Heppner, Stolarik, Shapiro, and Cain, 1960). The



Explorer VI data represent the first, repetitive measurements of the earth's field, between 4 and 8 earth radii, during a magnetic storm.

#### BACKGROUND

The following background information is necessary to understand the experimental data and our analysis of it. The nature of the experimental measurements, the satellite orbit characteristics, the surface magnetic conditions, and the characteristics of the non-storm field, obtained previously from Explorer VI data, are described below.

#### Instrumentation

The detecting element of the search coil magnetometer was a solenoid wound on a high permeability core. The detector was attached to the shell of the spin-stabilized spacecraft for which the rotation rate was 2.7 revolutions per second. Relative motion between the rotating spacecraft and the ambient stationary magnetic field, generated a sinusoidal voltage having a frequency equal to the spin rate and an amplitude proportional to  $B_{\perp}$  the component of the magnetic field perpendicular to the spacecraft spin axis (see figure 1). The coil voltage was fed to a tuned amplifier having a pass band centered at the spin frequency (see figure 2). A quasi-logarithmic amplifier gain was achieved by using an AGC loop. This extended the dynamic range of the magnetometer to 3 orders of magnitude. When the experiment was designed, theoretical inconsistencies in the predicted character of the distant field demanded that field measurements be possible over an extended range of altitudes.

The magnetometer coil constant is the numerical relation between the field strength and the voltage generated in the coil. It was determined by

---

\* Figures follow the page on which they are first mentioned. See pages 88-95 for the complete figure captions.

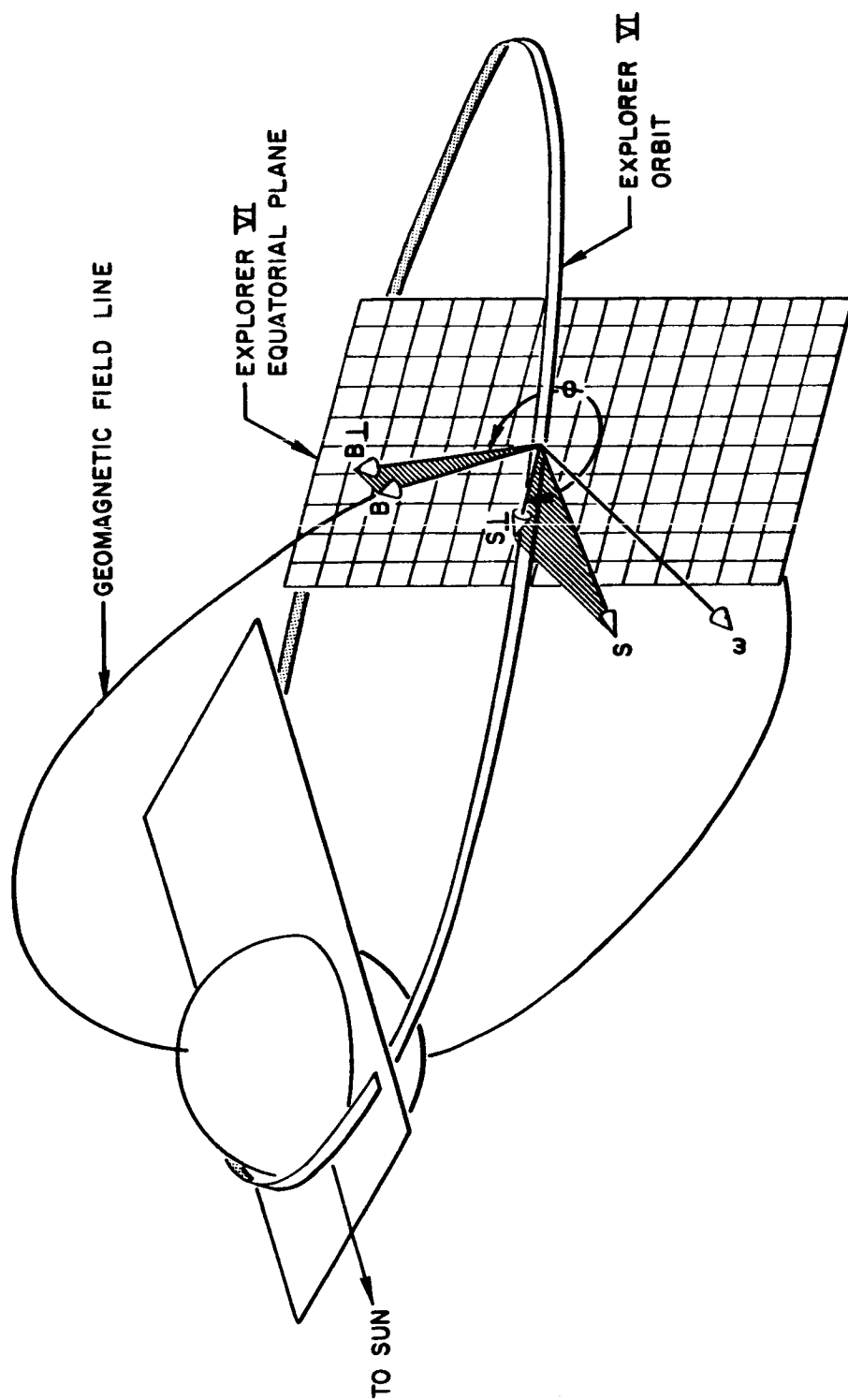


Figure 1. Spacecraft Coordinate System.

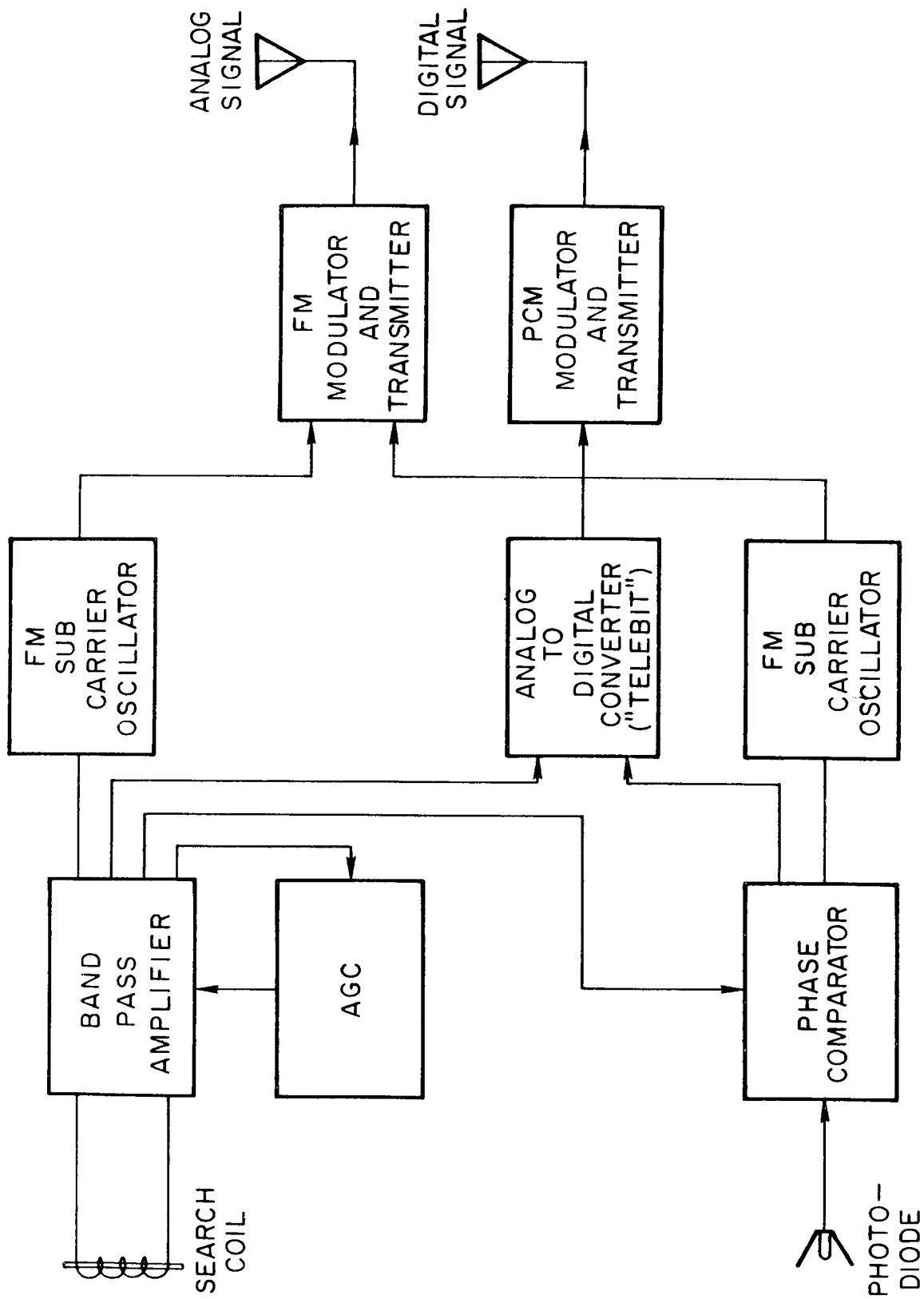


Figure 2. Block Diagram of the Search Coil Magnetometer.

comparing the voltages generated when the search coil and a standard air-core coil were simultaneously rotated in the earth's field in a region where gradients were small. Sinusoidal voltages were applied to the amplifier input to obtain the steady state calibration. (The transient response of the magnetometer is not pertinent to this paper and will be discussed elsewhere.) The details of the equipment and its calibration have been reported previously (Judge, McLeod, and Sims, 1960). For a given field magnitude, the output signal depended on the spin rate of the spacecraft and was slightly dependent on the temperature of the electronics. The spin rate was determined to a very high degree of accuracy by counting the number of cycles of the telemetered sinusoid in a given time period. The temperature of the electronics was checked, using several temperature sensors located inside the spacecraft.

Analysis of Pioneer I magnetometer data, in which large angular changes in the distant field were detected (Sonett, Judge, Kelso, 1959), indicated a need for vector field data in subsequent experiments. The data reduction program for the Pioneer I experiment provided for the analysis of the phase of the returned magnetometer signal. However, an initial phase reference was not available. Thus, the Explorer VI instrumentation included a photo diode-sunscanner and phase comparator. This provided both a phase reference, based on the solar direction, and in-flight determination of directional variations in  $B_{\perp}$ .

The phase comparator measured the angle,  $\phi$ , between  $B_{\perp}$  and  $S_{\perp}$ , where  $S_{\perp}$  is the projection into the spacecraft equatorial plane of a unit vector pointing in the direction of the sun (see figure 1). Hereafter,  $\phi$  is called the phase angle. It is the magnetic declination in the spacecraft

reference frame, measured with respect to the earth-sun direction.  $\phi$  depends on the orientation of the spacecraft spin axis.

The phase comparator utilized two input signals: the sinusoidal search coil signal and a sequence of periodic pulses from the photodiode (see figure 2). The output signal was a DC voltage proportional to the time delay between: (1) a pulse received from the photodiode when it was illuminated by solar radiation, and (2) a pulse coincident with the zero-voltage-crossing of the search coil signal. These two signals were used to drive Schmidt triggers which controlled the state of a flip-flop. A voltage, obtained by integrating the flip-flop output signal, was proportional to the time delay between the two pulses. The only characteristic of the search coil sinusoid used was the time at which the signal made a zero-voltage-crossing. Thus, except for very small field magnitudes, the phase comparator output was independent of the magnitude of the sinusoid and the measurement of  $\phi$  was independent of  $B_{\perp}$ .

The voltages were converted to frequency modulated signals (by sub-carrier oscillators) and telemetered. The data output voltages were also digitized inside the spacecraft and binary numbers were transmitted. The transmissions of digital data, which were commanded periodically from the ground, were sporadic. (The digital transmitter was checked out on Explorer VI for subsequent use on Pioneer V.) The analog transmissions were continuous and were received at one or more ground stations for approximately three-fourths of the satellite lifetime. The digital data have been used primarily to check the quality and accuracy of the telemetered analog data.

### Orbital Parameters

Since Explorer VI was launched in August 1959, much time and effort has been expended in order to refine the determination of the orbit. Refinement was a necessary consequence of perigee drag fluctuations and solar-lunar perturbations, knowledge of which was not well developed in 1959. With the establishment of an accurate orbit and a precise spin axis orientation, the more subtle effects in the data, such as the properties of the disturbance field near the geomagnetic equator, could be studied.

The Explorer VI orbit was highly eccentric (apogee = 48,800 km; perigee = 6740 km). The orbital plane was non-equatorial, being inclined  $47^{\circ}$  with respect to the geographic equatorial plane. Apogee occurred at a geographic latitude of  $-20^{\circ}$ . Figure 3 shows the projection of the orbit onto the surface of the earth. The spacecraft crossed the equatorial plane at geocentric altitudes of 7,200 and 30,000 km.

A non-equatorial orbit has important consequences for magnetometer data. An almost universal tendency to visualize such data in terms of an equatorial trajectory can lead to serious misinterpretations. Trajectory effects are an essential feature of the experimental results and are discussed in some detail in this paper.

The satellite was launched from Atlantic Missile Range at 1345 GMT on August 7, 1959. Since perigee occurred at about 0900 hours local time, apogee was located on the opposite side of the earth at 2100 hours local time. On August 7, the projection onto the geographic equatorial plane of the semi-major axis of the orbit made an angle of  $\sim 135^{\circ}$  with respect to the earth sun direction. This angle decreased by approximately  $1^{\circ}$  per

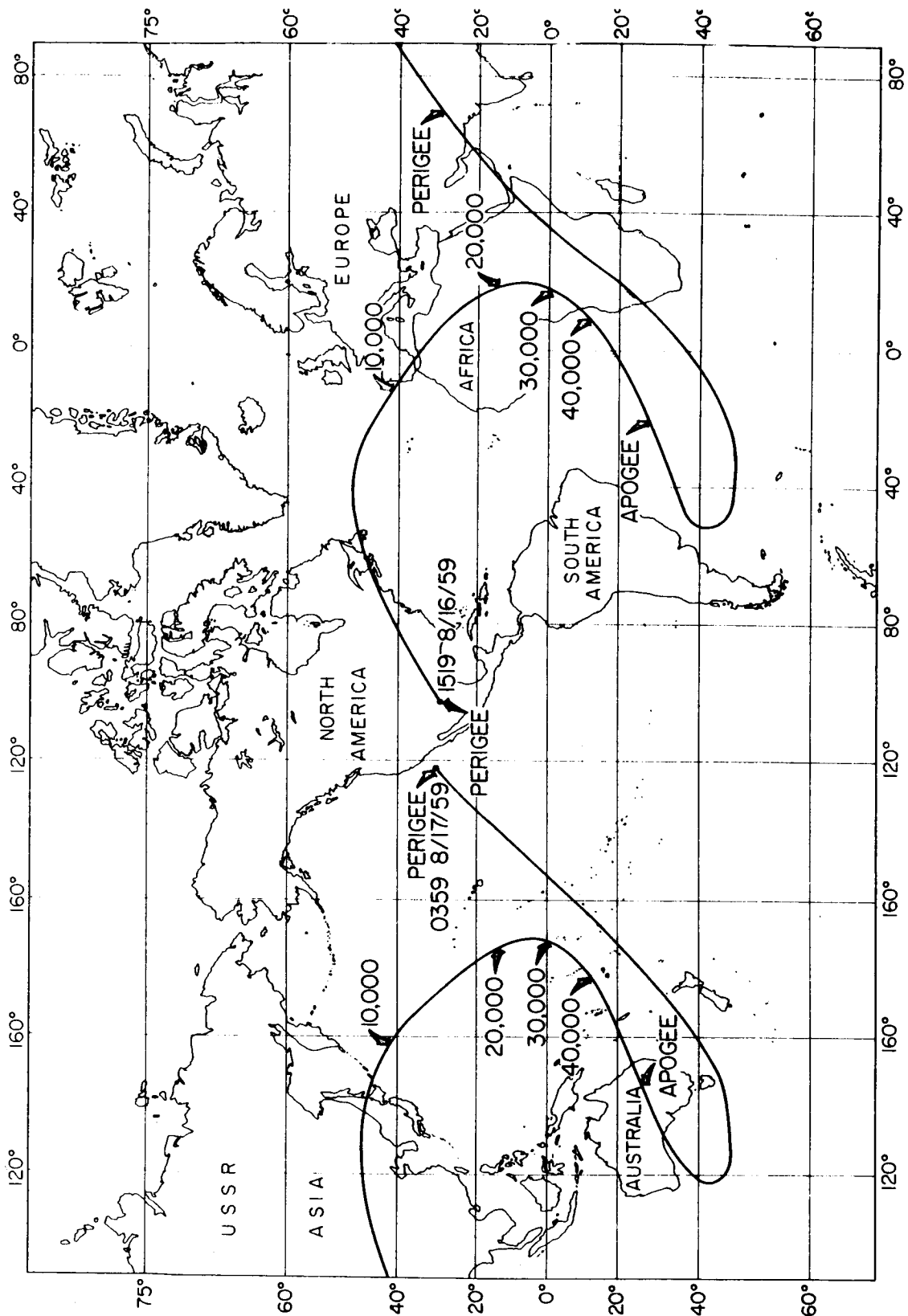


Figure 3. Projection of the Explorer VI Trajectory onto the Earth.

day. The right ascension and declination of the spin axis were  $217^{\circ}$  and  $23^{\circ}$ , respectively.

The orbital period was nearly  $12\text{-}3/4$  hours. Thus, the distant geomagnetic field and the radiation zones were traversed twice daily. This particular orbital period has an important consequence which affects the instantaneous location of the spacecraft in geomagnetic coordinates. Because the earth's magnetic pole is inclined  $11\text{-}1/2^{\circ}$  with respect to the earth's rotational axis, the geomagnetic latitude of a fixed point in space will undergo a diurnal variation. For example, a point on the geographic equatorial plane will vary between  $+11\text{-}1/2^{\circ}$  and  $-11\text{-}1/2^{\circ}$  geomagnetic latitude. Because the Explorer VI orbital period was approximately 12 hours, the geomagnetic latitude of the spacecraft at certain points on the trajectory varied over a range of  $23^{\circ}$  on successive orbital revolutions. Furthermore, because the period differed slightly from 12 hours, there was an asynchronism between the rotation of the geomagnetic field and the orbital period. The asynchronism produced gradual changes in the trajectory of the spacecraft in geomagnetic coordinates. The slow progression of geomagnetic coordinates has prompted us to divide the data obtained on odd-numbered and even numbered passes into two separate groups in order to isolate temporal changes in the geomagnetic field more clearly.

#### MAGNETIC CONDITIONS AT THE EARTH'S SURFACE

The magnetic history of the period (Lincoln, 1960) to be discussed may be summarized as follows (see figure 4): August 12, 13, 14 were among the five quietest days in August. On August 15, a gradual commencement storm was reported at some stations. At approximately 0400 on August 16,



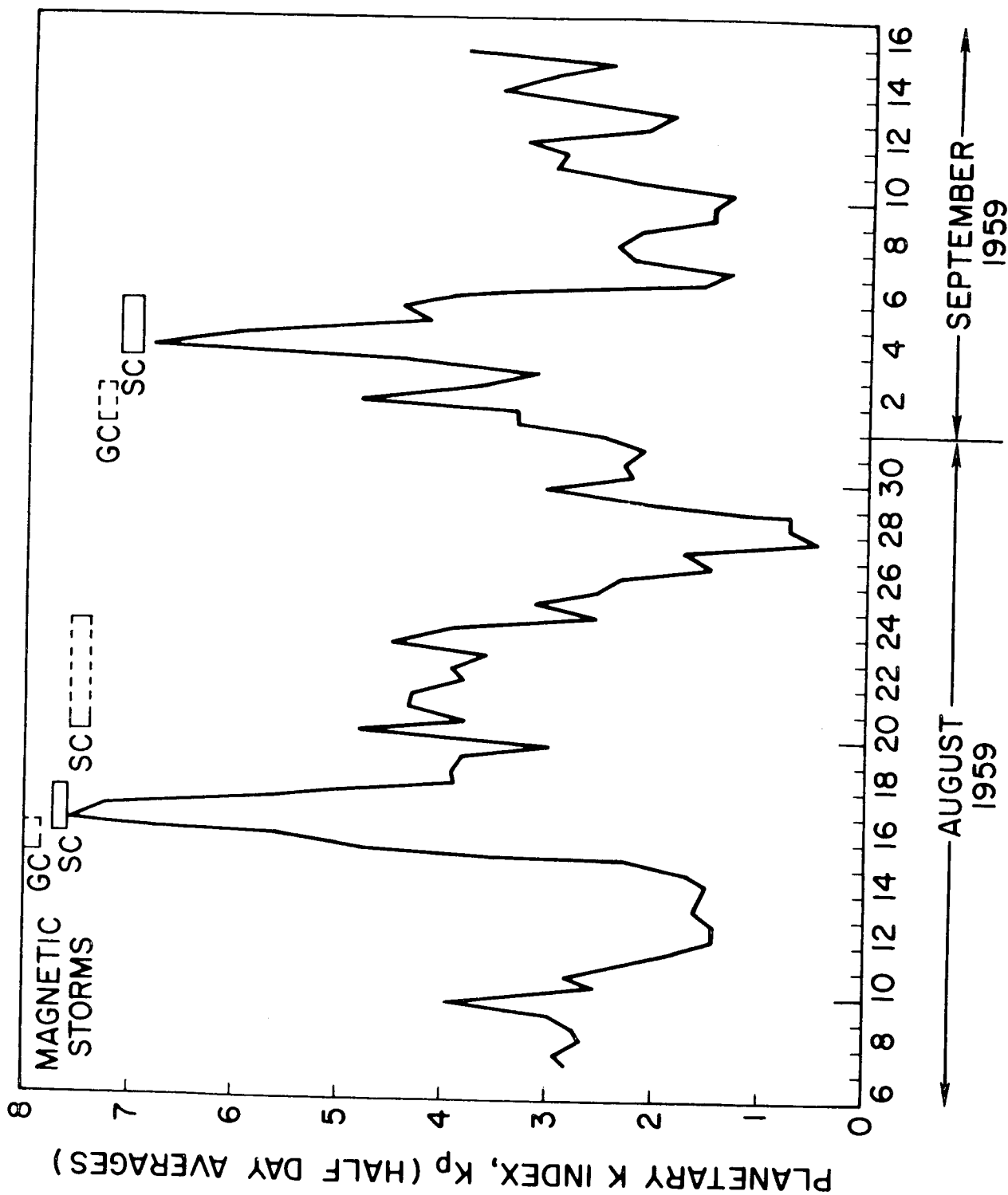


Figure 4. Geomagnetic Activity during the Explorer VI Epoch

a sudden commencement storm began which continued until the end of the 17th or beginning of the 18th. This storm was classed as severe (corresponding to a K-index of 8 or 9). Huancayo reported a moderate, gradual commencement storm which began at 0635 on August 18 and ended at 2000 hours the same day. A moderately severe, sudden commencement storm began on August 20 at 0412. There is no general agreement as to when this storm ended. (Some stations estimated that it ended the 20th while others recorded disturbed conditions until August 24). August 27 and 28 were the two quietest days of the month. A moderately severe ( $K = 6, 7$ ) sudden-commencement storm began on September 3 at 2159 and continued until the 5th or 6th. The discussion below will be concerned primarily with the severe magnetic storm of 16 August.

#### Review of the Data Obtained on Non-storm Days

Preliminary analysis of the Explorer VI data obtained on non-storm days (Sonett, Smith, Judge, and Coleman, 1960; Sonett, Smith, and Sims 1960; Smith, Coleman, Judge, and Sonett, 1960) consisted of a comparison between the magnitude,  $B_{\perp}$ , and direction,  $\phi$ , of the observed field and the magnitude and direction of the extrapolated geomagnetic field. An 8 coefficient, spherical-harmonic expansion of the surface field (Vestine, 1959) was used to derive the extrapolated vector field, which was then resolved into two components, one of which, having a magnitude  $G_{\perp}$  and declination  $\phi_G$ , was perpendicular to the Explorer VI spin axis.

The comparison revealed discrepancies between  $B_{\perp}$  and  $G_{\perp}$  throughout most of the trajectory.  $B_{\perp}$  tended to exhibit the same altitude dependence as  $G_{\perp}$  below  $5R_E$  but to have a somewhat larger magnitude. At altitudes beyond approximately  $5R_E$ , there was a marked disparity in functional dependence.

Because automatic gain control was employed, the sensitivity of the magnetometer was a quasi-logarithmic function of the ambient field magnitude. For example, a change of one per cent in the output voltage corresponded to a 300  $\gamma$  difference in a 5000  $\gamma$  field (approximate altitude, 12,000 km), and to a difference of only 3  $\gamma$  in a 100  $\gamma$  field (approximate altitude, 38,000 km). Beyond  $5R_E$ , measured differences between  $B_{\perp}$  and  $G_{\perp}$  corresponded to a large fractional change in the magnetometer output signal, whereas, appreciable magnitude differences below  $5R_E$ , correspond to small fractional differences in output voltage.

The experimental results suggested that the extraterrestrial field was essentially a dipole field out to  $5R_E$  but became progressively non-dipolar at greater altitudes. The shape of the deviation between  $G_{\perp}$  and  $B_{\perp}$  depends strongly on the direction of  $B_{\perp}$ , as well as on its magnitude. The phase comparator data also revealed a characteristic difference between  $\phi$  and  $\phi_G$  beginning at  $5R_E$ , which showed that the directional behavior of the field was also non-dipolar. A preliminary survey of data obtained throughout a six-week interval showed that these differences were a characteristic feature of the distant field. Perturbations in  $B_{\perp}$  and  $\phi$  were always noted, although their shapes varied from day to day and were strongly dependent on the geometry of the experiment, in particular the trajectory of the spacecraft.

To assess the character of the observed differences, a simple mathematical model of a perturbation field based on a longitudinal current source with a finite, circular cross section and constant current density, was utilized. The field due to the current was computed at points,

on the trajectory, added vectorially to the geomagnetic field, and a coordinate transformation was performed to yield theoretical values of  $B_{\perp}$  and  $\phi$ . Reasonable agreement between the data and the model calculations was obtained for a westward current of  $5 \cdot 10^6$  amperes centered at  $10R_E$ . (Smith, Coleman, Judge, and Sonett, 1960.)

The same mathematical model was applied to the Pioneer V magnetometer data obtained inside the geomagnetic field. There were important differences in the trajectories of the two spacecraft. Perturbations in the distant geomagnetic field were observed by Explorer VI on the evening and night side of the earth, and by Pioneer V on the side of the earth toward the sun. Reasonable agreement was again obtained between the calculated and observed  $B_{\perp}$  for a westward current of  $5 \cdot 10^6$  amperes, located between 5 and  $11R_E$ .

#### THE EXPERIMENTAL DATA

The magnitude data appearing in figure 5 were obtained on three successive days during the severe SC storm which began on August 16.  $B_{\perp}$  and  $G_{\perp}$  are shown as functions of geocentric altitude. The storm data have the same general features as the measurements made on non-storm days (e.g., see figure 1 in Sonett, Smith, Judge and Coleman 1960). The fine structure appearing in figure 5, e.g., a variation of several hundred gamma which occurred at 30,000 kilometers on August 17, may be either spatial or temporal variations. The fine structure is a subject of special interest and is being investigated separately in connection with bay-like, storm variations (Smith and Judge, 1961).

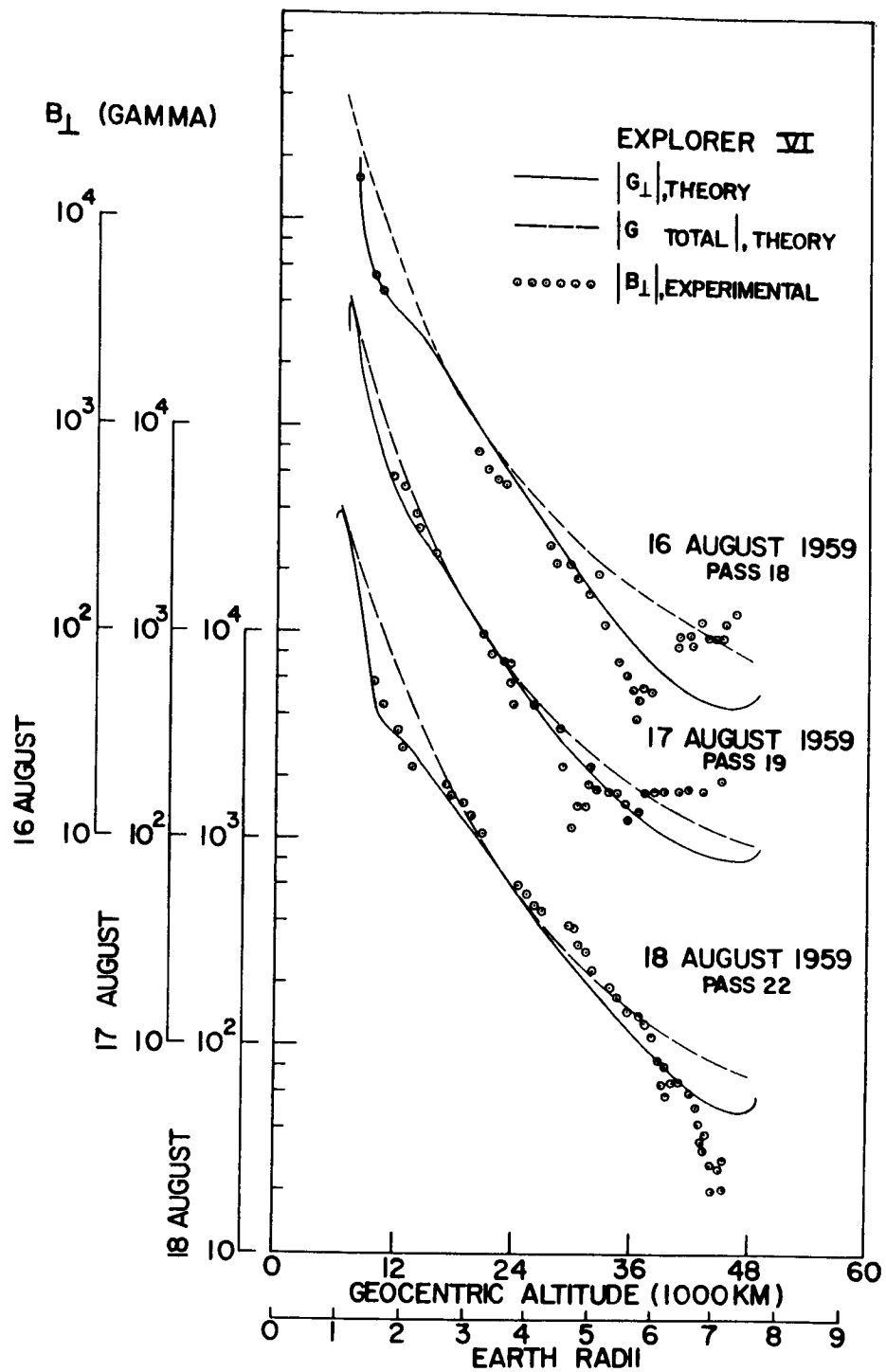


Figure 5. Explorer VI Field Magnitude Data During the Magnetic Storm of 16-18 August.

In the vicinity of  $3R_E$ ,  $G_{\perp}$  and  $G$  coalesce because the spacecraft spin axis is orthogonal to the dipole field direction and, consequently, the magnetometer measures the total field magnitude. At other points on the orbit, the spin axis orientation is such that the total field is not measured. This accounts for the difference between the solid line,  $G_{\perp}$ , and the dashed line,  $G$ , over parts of the trajectory in figure 5.

In interpreting the data, the important assumption is made that there is latitudinal symmetry about the geomagnetic equatorial plane for both unperturbed and stormtime fields. Under this assumption, the disturbance field is antiparallel to the dipole field on the equator and measurement of the scalar field alone completely specifies the resultant field. For non-equatorial points of observation the direction of the field becomes important.

In general, variations in  $B_{\perp}$  can be caused by a change in the direction of the field as well as by a change in magnitude. Because interpretation of the experimental data can be simplified by treating the equatorial measurements separately, the data have been divided in two parts. The first consists of the time and altitude dependence of the field magnitude near the geomagnetic equatorial plane. The second part involves the direction of the distant field at points of observation which are generally not located near the equatorial plane. The centered dipole approximation of the geomagnetic field is used to define the geomagnetic equator.

#### Variation in the Magnitude of the Near-Equatorial Field During the Storm

Figure 6-a shows the time variation of field magnitude in the outer radiation zone. Each datum is obtained from the field magnitude,  $B_{\perp}$ ,

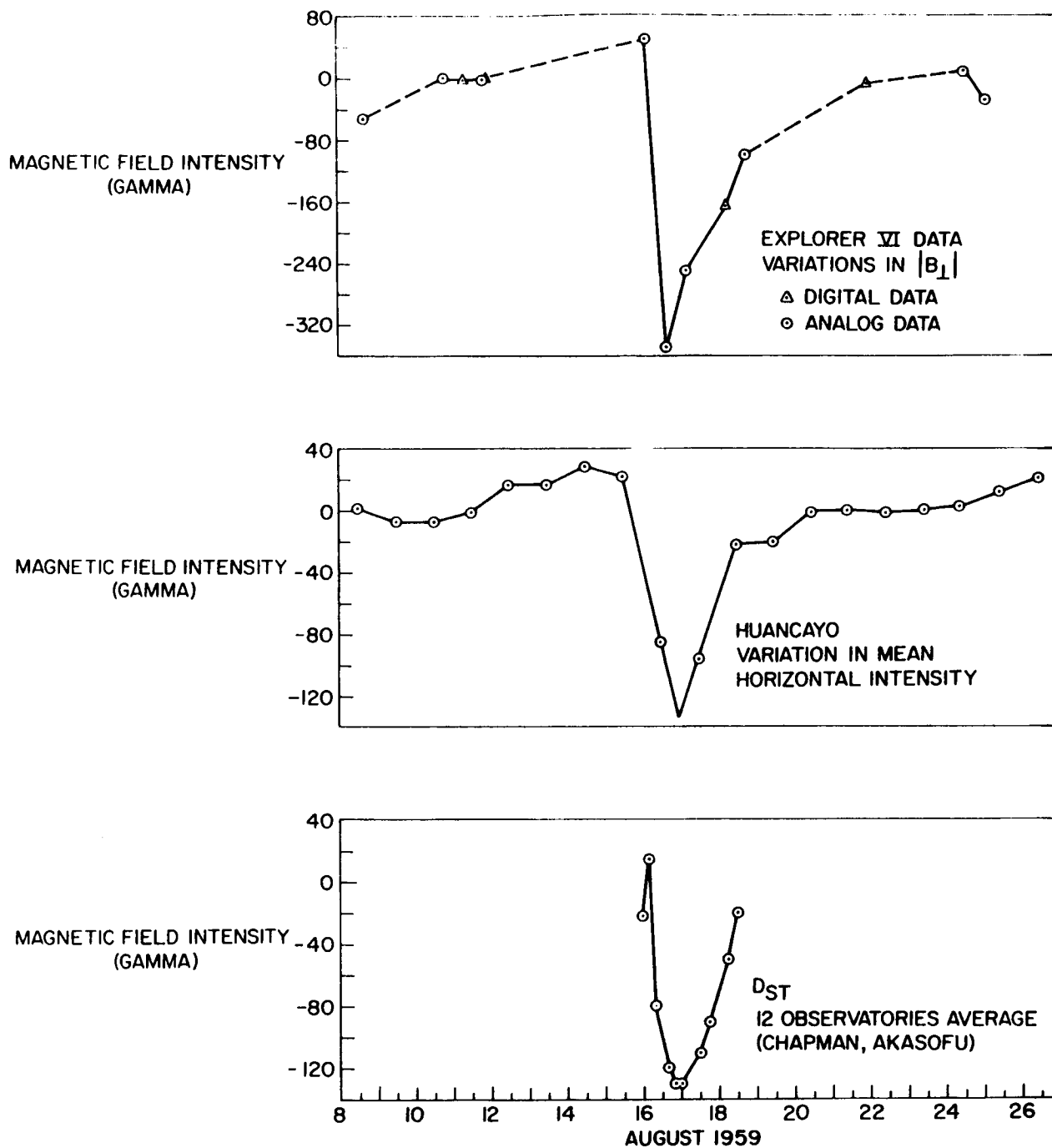


Figure 6. Time Variations of the Equatorial Disturbance Field Compared with  $D_{st}$  Variations at the Earth's Surface.

at a geocentric distance of approximately 24000 kilometers during a single orbital pass. For each such value of  $B_{\perp}$ , the corresponding value of the extrapolated geomagnetic field,  $G_{\perp}$ , was computed. Figure 6-a represents a plot of the difference,  $\Delta B = B_{\perp} - G_{\perp}$ , during approximately the first two weeks of Explorer VI observations. The data have been normalized so that  $\Delta B = 0$  on magnetically quiet days (August 11 - 12). On magnetically quiet days, the observed field at  $4R_E$  tends to exceed the extrapolated value of the dipole field. This feature of the data is still under investigation. The data in figure 6-a were normalized so the  $\Delta B = 0$  on the quietest days of the month. Both analog and digital data appear in figure 6-a. The digital data, which are also normalized, provide data at times for which no analog data is presently available and demonstrate the agreement between the two forms of telemetered data.

Figure 6-b is a graph of the time variation of the horizontal component of the earth's field at the surface. Each datum is the daily mean value of the horizontal intensity at Huancayo, Peru, (geomagnetic latitude  $\delta_M = 0.6^\circ$ ). The data are obtained by averaging the hourly mean values over each Greenwich day and have been plotted at 1200 GMT on each day. This procedure provides a reasonable representation of the long period changes in the earth's field as subsequent removal of the daily variation has shown. The variation in mean horizontal intensity has also been normalized so the  $\Delta H = 0$  on August 11-12.

The outstanding feature of the Huancayo data is the effect of the super-imposed magnetic storms of August 15-20. The storm period was preceeded and followed by quiet intervals during which the horizontal



component rose to its highest values (August 14-15, 26-28). The effect of the SC storm which began on August 16 is particularly noticeable.

Figure 6-c which is a plot of the smoothed  $D_{st}$  curve derived by Chapman and Akasofu (Arnoldy, Hoffman, and Winckler, 1960), shows the history of the August 16 storm in greater detail than figure 6-b. The data represent averages of measurements of the horizontal component made at 12 observatories located at various latitudes and longitudes.

The long period variation of the storm field at the surface coincides with a similar variation at an altitude of 4 earth radii. A comparison of figures 6-a, b, c indicates that  $B_{\perp}$  undergoes a main phase decrease and recovery at  $\sim 4R_E$  which is essentially coincident with  $D_{st}$  at the surface. The magnitude of the main phase decrease is  $\sim 140$  gamma at the surface and  $\sim 360$   $\gamma$  at  $4R_E$ , i.e., approximately two and one-half times as large.

#### Variation in the Direction of the Extra-Terrestrial Field During the Storm

Figure 7 shows the departure of the observed field direction from the direction of the extrapolated geomagnetic field and contrasts the extent of the departure on storm days and days that are magnetically quiet. The experimental measurements obtained from the magnetic field aspect indicator (or phase comparator) are shown as a function of altitude for each of three orbital passes. Also shown are the theoretical values of the phase angle corresponding to the extrapolated geomagnetic field ( $\phi_G$ ). These values are obtained by transforming the extrapolated vector field into the spacecraft coordinate system to derive the angle between the field direction and the direction to the sun.

# EXPLORER VI MAGNETOMETER PHASE ANGLE

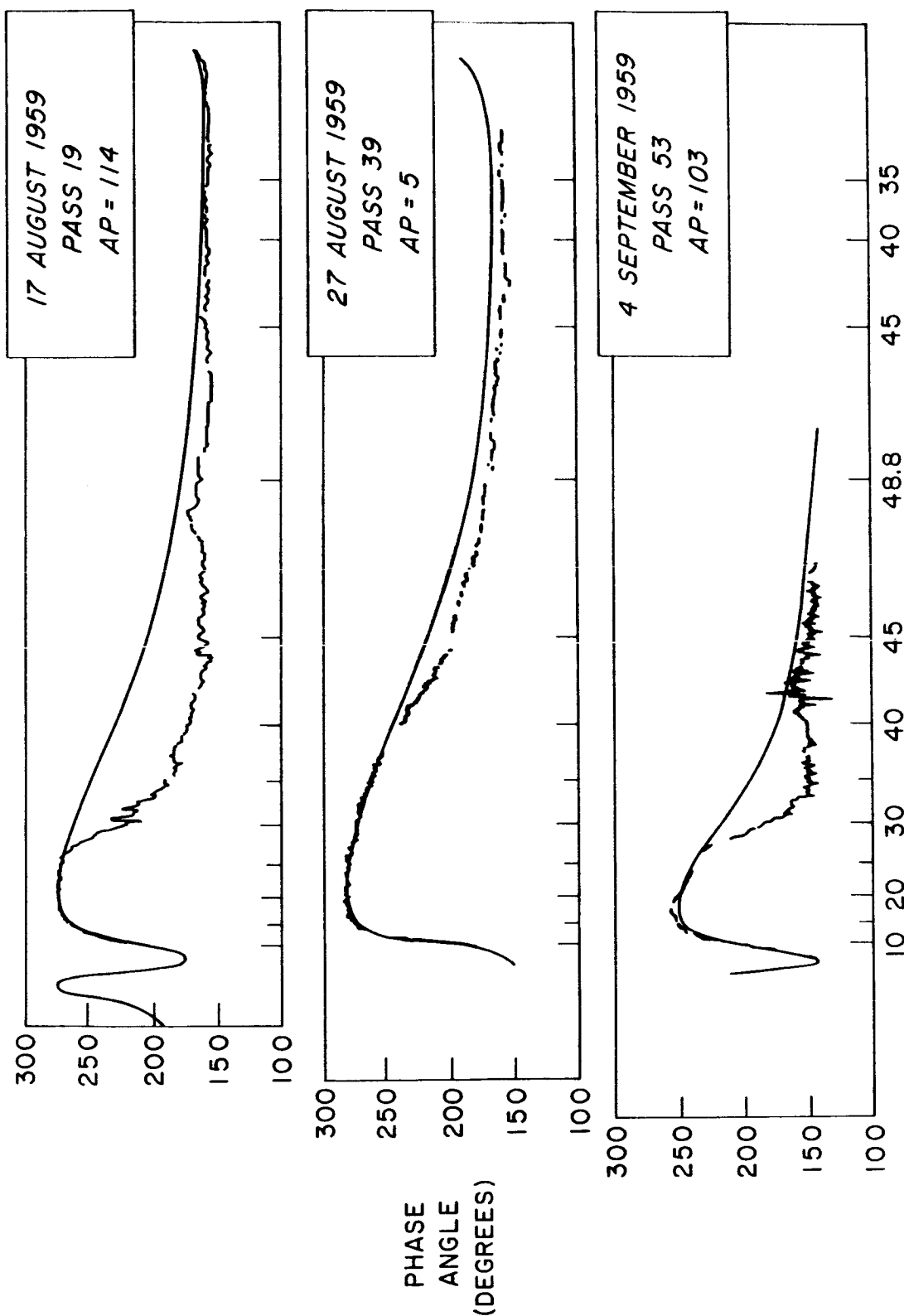


Figure 7. Phase Angle Data During Storm and Non-Storm Intervals.

Figure 7 shows that  $\phi$  and  $\phi_G$  are equal at geocentric distances of less than 10000 - 15000 kilometers. This agreement is due to the "stiffness" of the geomagnetic field near the earth (i.e., a transverse disturbance field of several hundred gamma will produce a negligible rotation of the dipole field lines). The same range of angles is (i.e.,  $150^\circ < \phi < 300^\circ$ ) observed near the earth and at great distances. Thus, the expected agreement between  $\phi$  and  $\phi_G$  near perigee provides a check on the consistency of the aspect indicator calibration.

At large distances from the earth  $\phi$  departs from  $\phi_G$ . At southern geomagnetic latitudes the phase deviation,  $\Delta\phi = \phi - \phi_G$ , is negative. On the geomagnetic equator ( $\delta_M = 0$  is indicated in figures 9 thru 12),  $\Delta\phi$  is either zero (passes 16, 18, 20) or tends to be slightly negative (passes 15, 17, 19, 21, 22).

The extent by which  $\phi$  departs from  $\phi_G$  depends, in part, on variations in the trajectory of the Explorer VI (i.e., the magnetic latitude of the spacecraft at a given altitude). There is also a time variation which is shown in an extreme form in figure 7. There were magnetic storms on August 17 and September 4, while August 27 was the quietest day of the month (see the  $A_p$  indices included in the figure).

The observed negative values of  $\Delta\phi$  for  $\delta_M < 0$ , is qualitatively consistent with the effects of a perturbation field caused by a westward-flowing current. Figure 8 shows an idealized situation in which spacecraft spin axis is assumed to be perpendicular to the magnetic meridian plane (which also contains the sun vector,  $\hat{S}$ ). This example demonstrates how a perturbing field affects  $\phi$ . It should be noted that the spin axis is

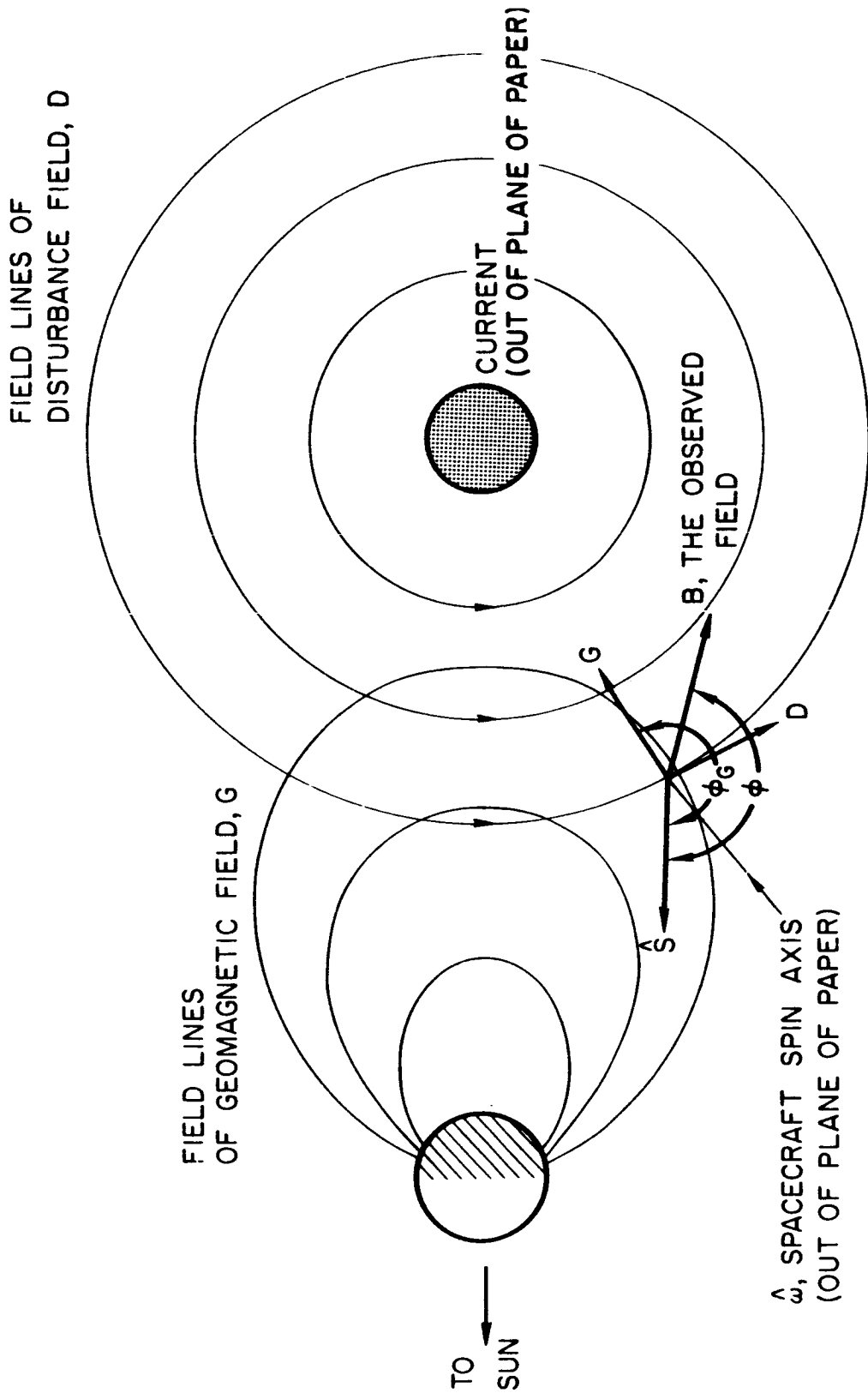


Figure 8. Qualitative Explanation of the Effect of a Disturbance Field on the Phase Angle.

not actually orthogonal to the magnetic meridian plane near apogee - but is inclined at an angle of 30-50 degrees with respect to the latter. However, the situation in figure 8 is qualitatively correct near apogee, as the model calculations have shown.

The departure,  $\Delta\phi$ , has its smallest magnitudes on August 27 and August 13. As figure 6 indicates, the horizontal intensity at the earth's surface rises to its highest value on these quiet days. These observations are qualitatively consistent with a decreased westward current in the outer atmosphere of the earth.

Another notable feature of figure 7 is the occurrence of fine structure during magnetic storms. Several distinct transients (such as those seen at 30,000 kilometers on August 17 and at 42,000 kilometers on September 4) correlate with the occurrence of pulsating magnetic bays in the antarctic (Smith and Judge, 1962), and transient increases in the Explorer VI scintillator count rate. According to Rosen and Farley (1960), the occurrence of rapid variations in the scintillator count rate is typical of magnetic storms or magnetically disturbed periods. Rapid variations in the direction of the distant field are also associated with magnetically disturbed conditions, as figure 7 indicates.

Figures 9 thru 12 contain the phase angle data for eight successive orbital passes during the storm period August 15-18. The  $\Sigma K_p$  values are the sums of the 3 hour, planetary K indices during the 12-hour period corresponding to each orbital pass of the Explorer VI.  $K_p$  is a measure of the magnetic agitation at the surface. The altitude at which the spacecraft crossed the geomagnetic equatorial plane is indicated in

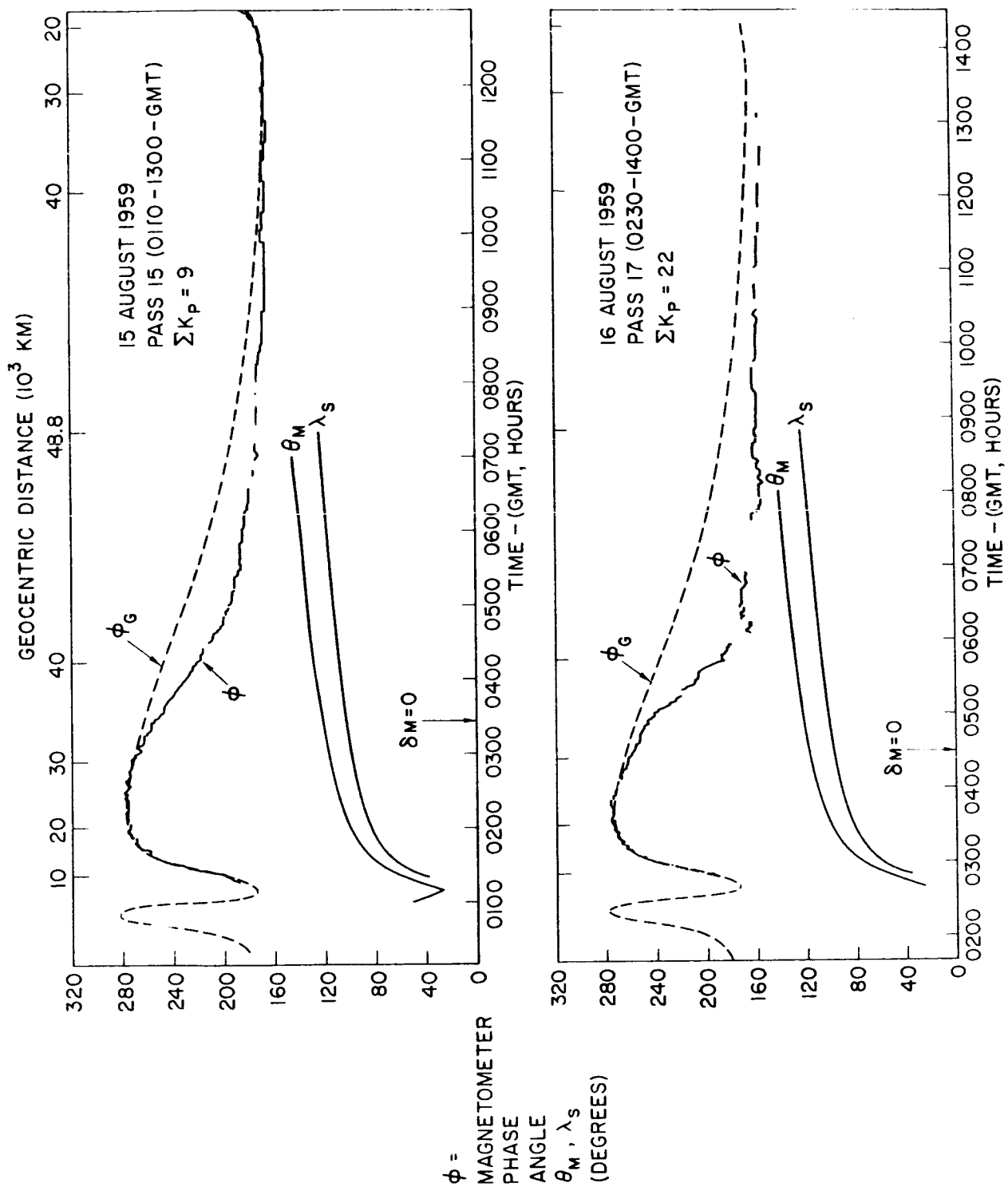


Figure 9. Phase Data Obtained During a Magnetic Storm (odd numbered passes).

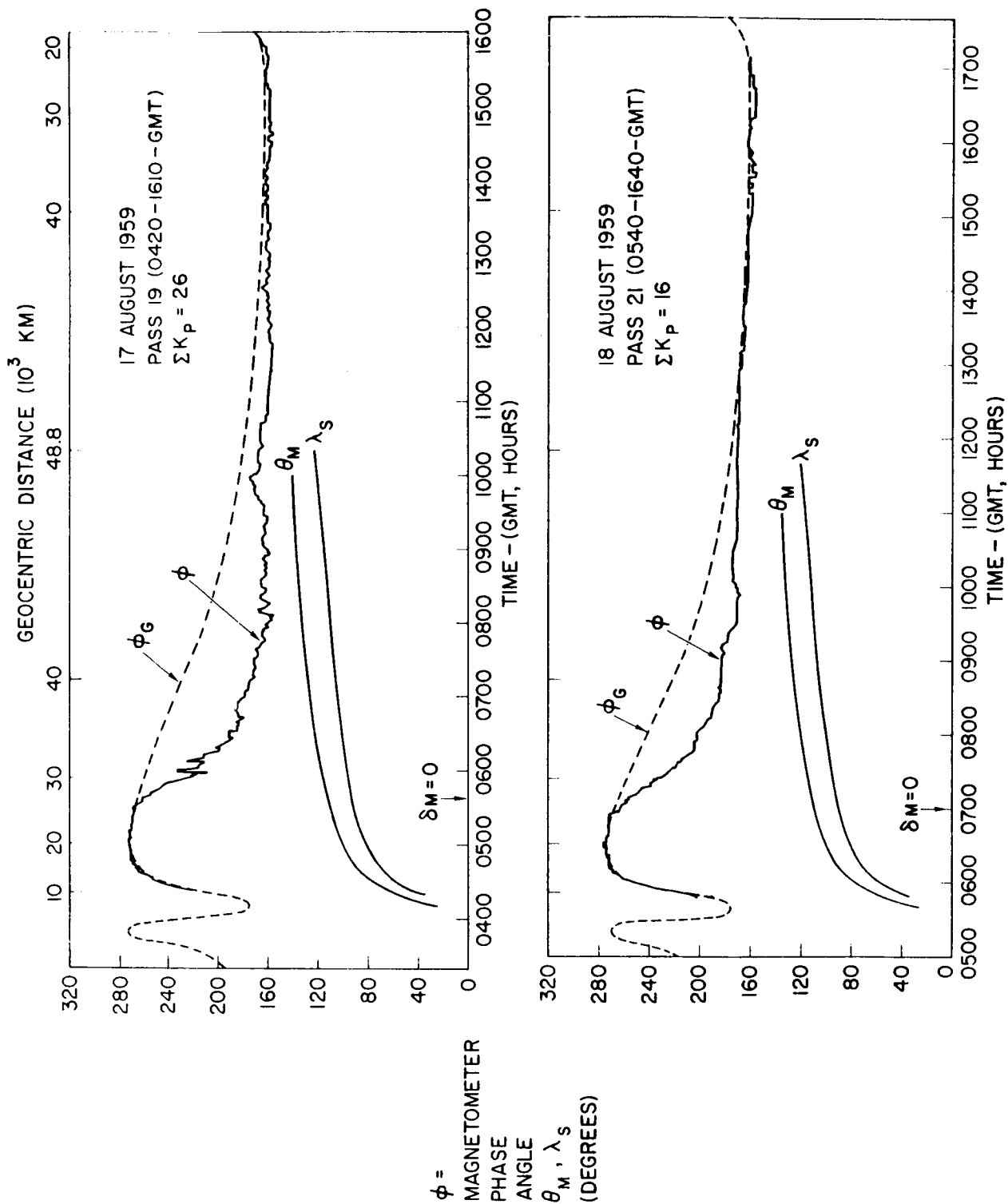


Figure 10. Phase Data Obtained During a Magnetic Storm (odd numbered passes)

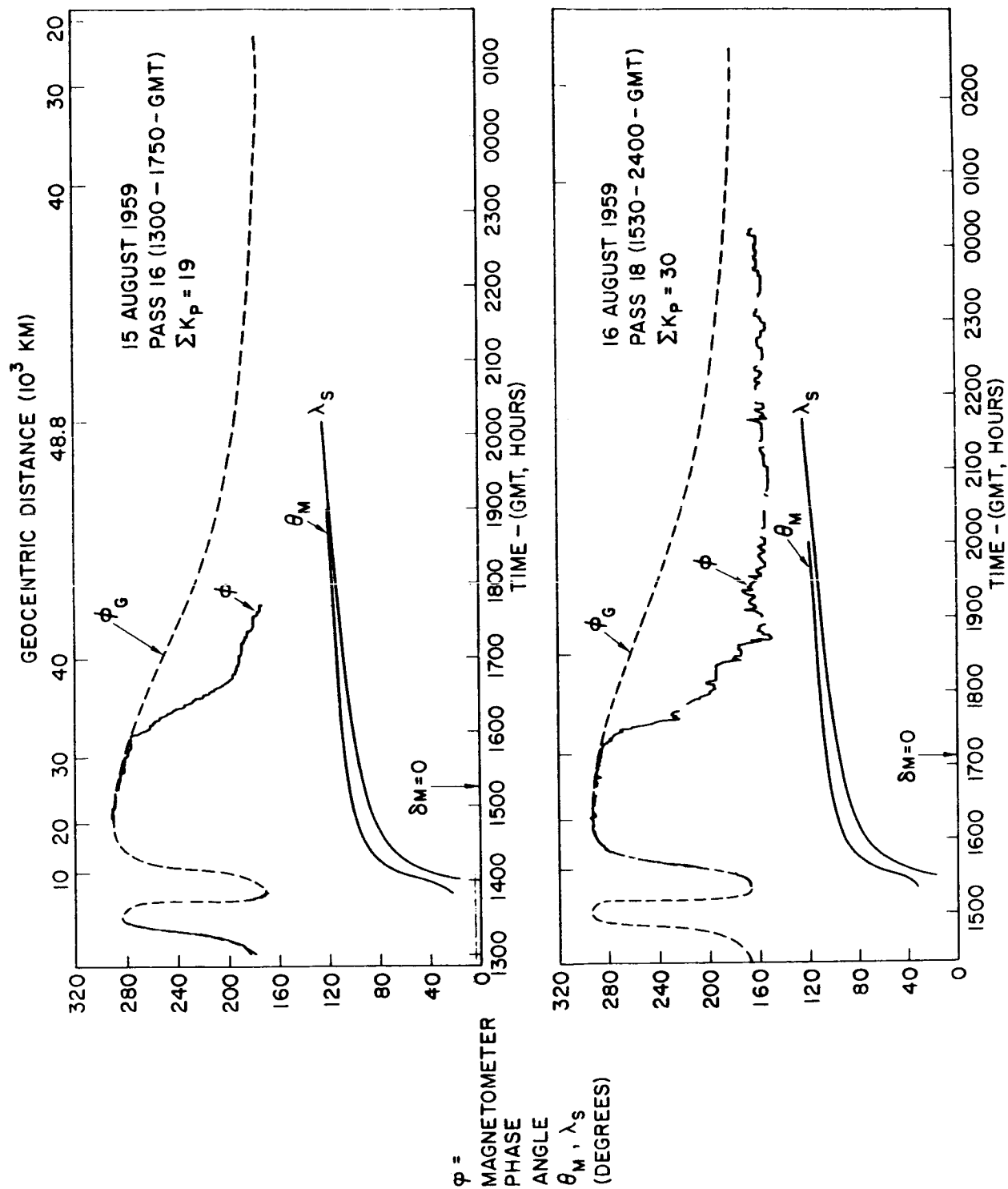


Figure 11. Phase Data Obtained During a Magnetic Storm (even numbered passes)



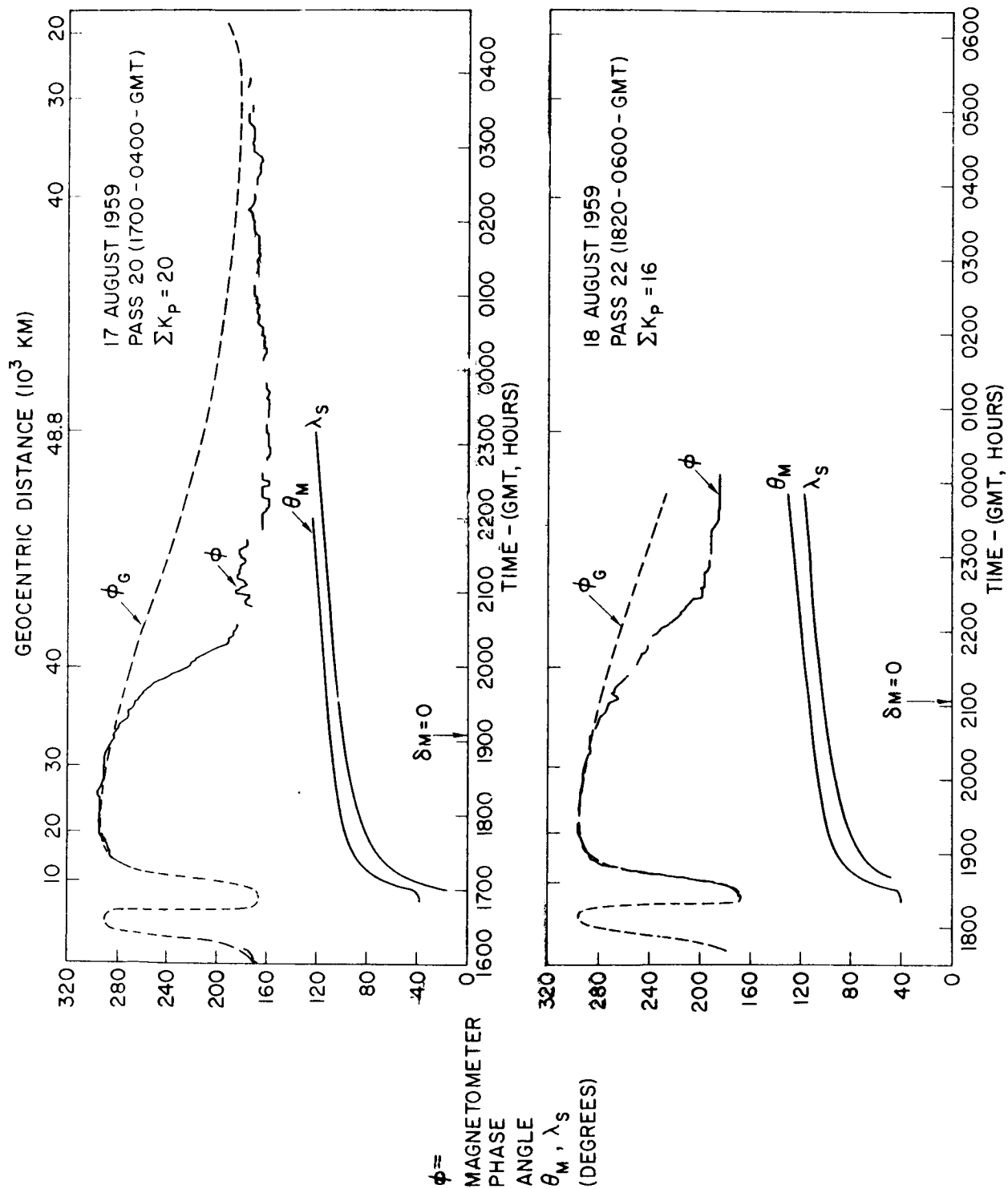


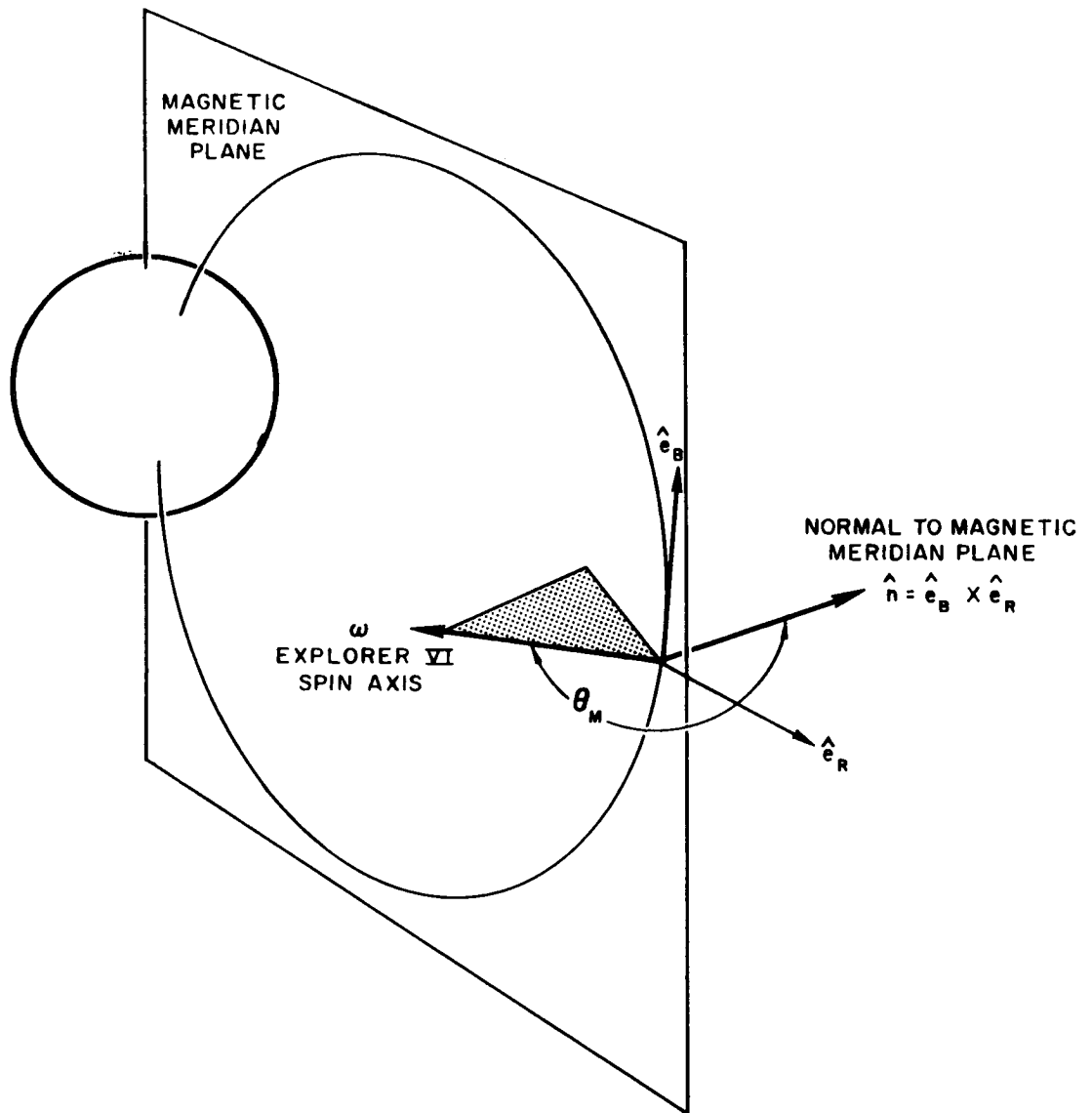
Figure 12. Phase Data Obtained During a Magnetic Storm (even numbered passes)

each figure. Also shown in figures 9 thru 12 are two angles,  $\theta_M$  and  $\lambda_S$ , which are helpful in interpreting the data.

$\theta_M$  is the angle between  $\hat{\omega}$ , the Explorer VI spin axis, and  $\hat{n}$ , the normal to the local magnetic meridian plane (see figure 13). The meridian plane contains the local direction of the field and the center of the earth.  $\hat{n}$ , the perpendicular to the magnetic meridian plane, is given by  $\hat{e}_B \times \hat{e}_R$ , where  $\hat{e}_B$  is the direction of the extrapolated geomagnetic field and  $\hat{e}_R$  is the radius vector from the earth's center to the spacecraft.  $\theta_M$  indicates to what extent the spacecraft spin axis is rotated out of the magnetic meridian plane at different points along the trajectory.

$\lambda_S$  is the angle between the two directions - obtained by projecting the earth-sun vector, and the satellite radius vector, onto the equatorial plane (see figure 14).

As discussed earlier, a division of the data into two groups is made in order to minimize trajectory effects. Figures 9 and 10 contain only the odd-numbered passes, which generally occurred during the first half of the Greenwich day, whereas Figures 11 and 12 contain even-numbered passes. There are small progressive changes in the geomagnetic coordinates of the spacecraft on the odd-numbered and even-numbered orbits taken alone. On the other hand, there are large changes in geomagnetic coordinates on passes taken consecutively. The gradual time variation of the trajectory in geomagnetic coordinates is seen in figures 15 and 16. The altitude at which  $\delta_M$  is equal to zero progresses to higher altitudes during the odd-numbered passes and to lower ones during the even-numbered passes.



$\hat{e}_B$ , UNIT VECTOR IN DIRECTION OF GEOMAGNETIC FIELD  
 $\hat{e}_R$ , UNIT VECTOR IN DIRECTION FROM EARTH'S CENTER

Figure 13. Representation of the Angle,  $\theta_M$ .

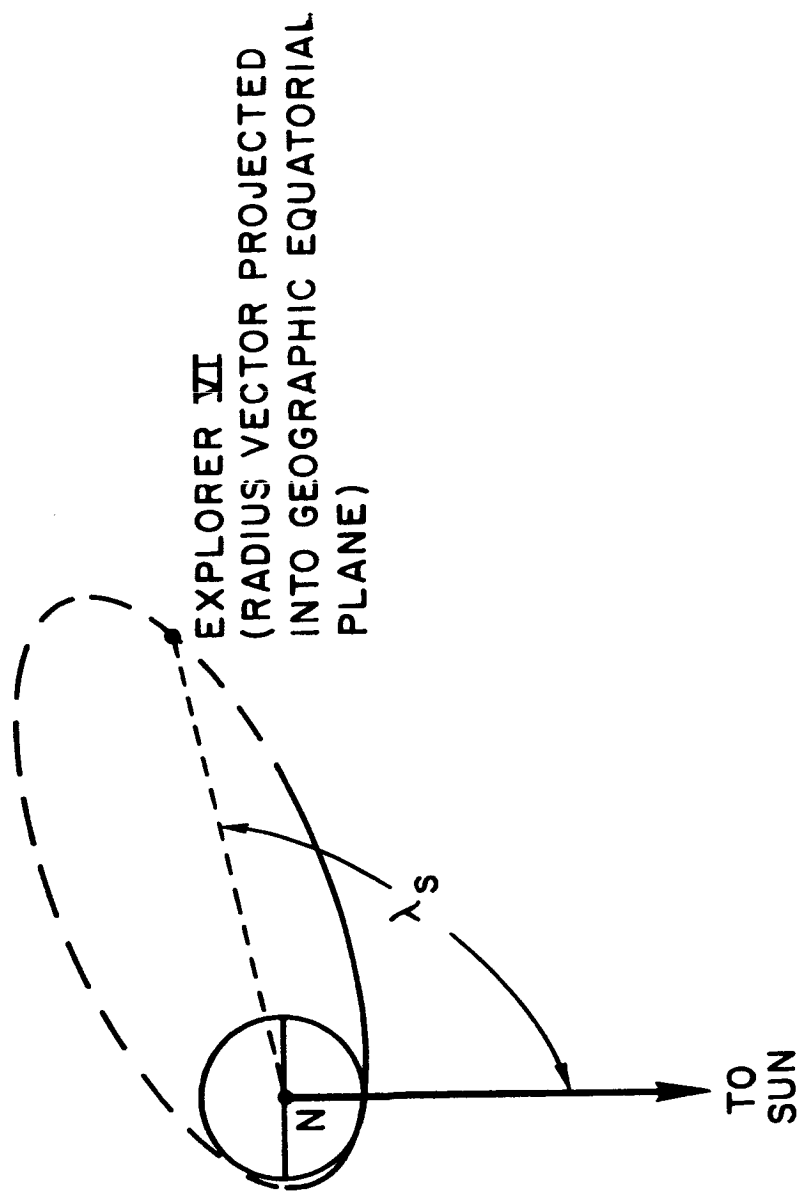


Figure 14. Representation of the Angle,  $\lambda_s$ .

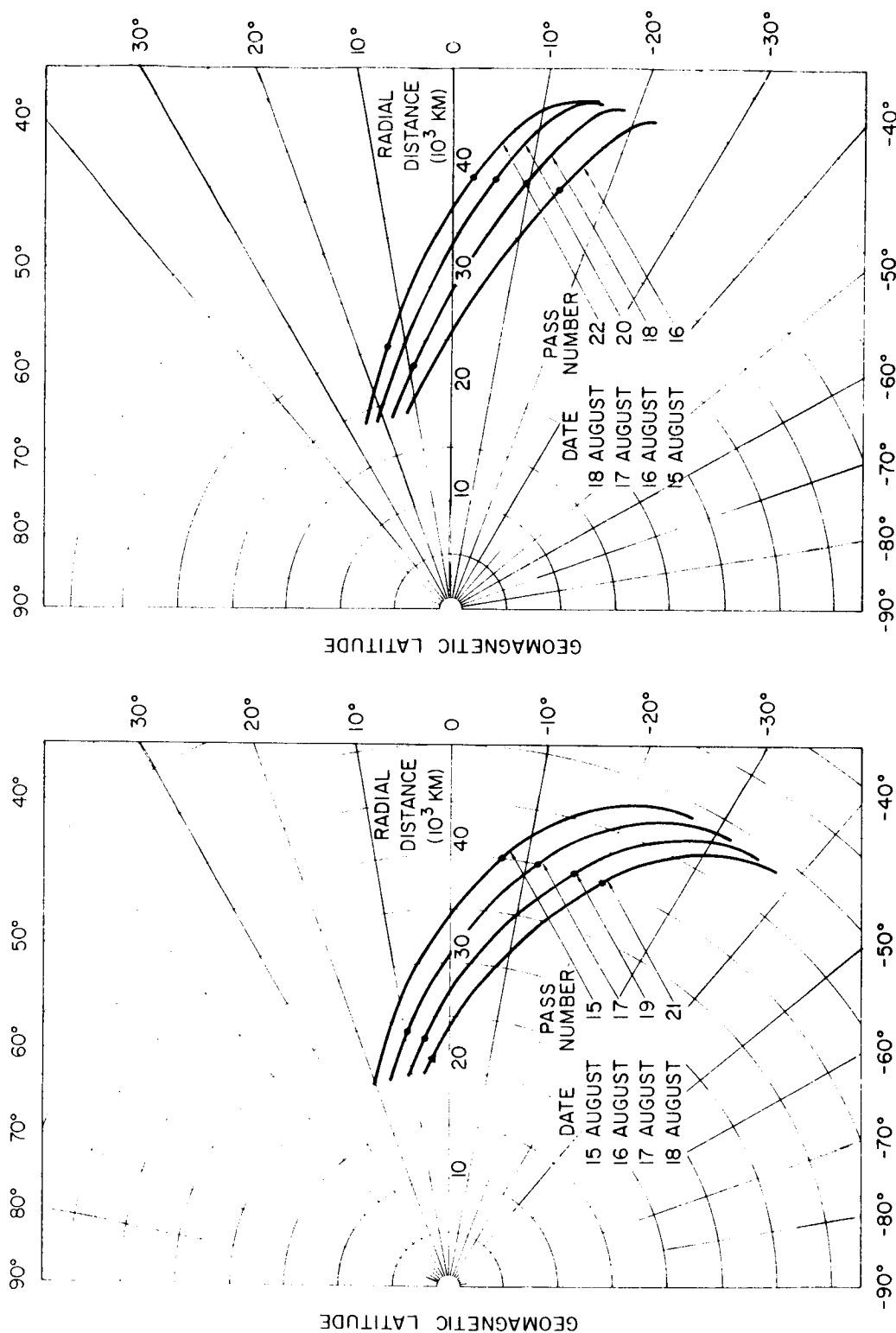


Figure 15. Geomagnetic Latitude of the Spacecraft (odd numbered passes).

Figure 16. Geomagnetic Latitude of the Spacecraft (even numbered passes).

Figures 9 thru 12 show a progressive enhancement of  $\Delta\phi$  during the storm with a subsequent return to pre-storm values. This may be seen by considering a given  $\Delta\phi$ , which we designate  $\Delta\phi^*$  (e.g.,  $\Delta\phi = -20^\circ$ ).  $R(\Delta\phi^*)$ , the altitude at which  $\Delta\phi = \Delta\phi^*$ , moves toward lower altitudes during the main phase of the storm ( $\Sigma K_p$  increasing) and returns to higher altitudes during the recovery phase ( $\Sigma K_p$  decreasing).

Figure 17 provides an alternative view of the variations in  $\Delta\phi$  during the storm. Figure 17-a is a plot of  $\Delta\phi$  at a given altitude (40,000 kilometers) as a function of time. Figure 17-b shows the simultaneous variation in the horizontal intensity at the earth's surface. The data are hourly mean values of  $H$  at Huancayo. The diurnal variation has been removed. Figure 17-c is a plot of the corresponding value of the 3-hour index,  $K_p$ . The direction of the distant field is correlated with both variations in the horizontal component, and the extent of the agitation, of the surface field.

This correlation apparently includes the initial phase of the August 16 storm. However, the increase in  $\Delta H$ , and decrease in  $\Delta\phi$ , observed during the first quarter of August 16 actually represents a super-position of two effects. One is the initial phase of the SC storm of August 16. The other is the recovery phase of the GC storm of August 15. The effect of the GC storm on the distant field can be seen in the first two data points (August 15) in figure 11 and by comparing figures 9-a and 11-a (successive passes). An inspection of ground station magnetograms shows that the GC storm was of short duration. Because the two storms overlap, it is difficult to isolate and study the effects of the initial phase of

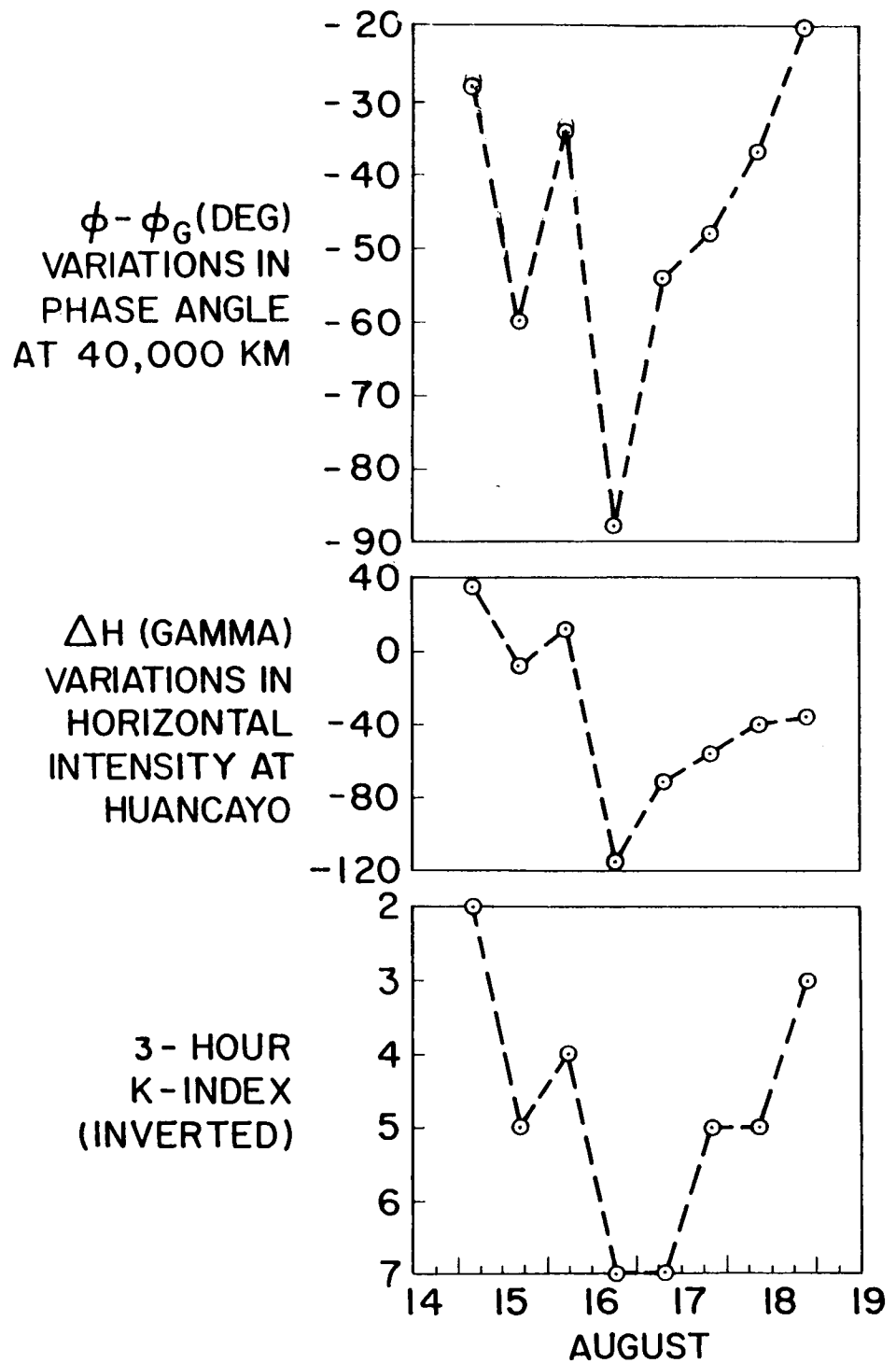


Figure 17. Temporal Variation in the Phase Data at 40,000 Kilometers Compared with the Surface Field.

the SC storm. The subsequent data show the effect of the main phase decrease and recovery associated with the August 16 storm.

Simultaneous Variations in Field Magnitude and  
Peak Intensity of the Outer Radiation Zone

Figure 18a contains the storm data shown previously in figure 6, i.e.,  $\Delta B$  at  $\sim 4R_E$ . Also, shown are the corresponding measurements of the peak intensity of the radiation particle fluxes in the outer zone. Figures 18b, c, d are the Explorer VI data obtained by the University of Minnesota Geiger tube, the University of Chicago proportional counter, and the Space Technology Laboratories Scintillation counter. Prior to the storm of August 16, the primary peak in the outer zone, based on the Geiger tube data, was located at approximately 24,000 kilometers (Arnoldy, Hoffman, and Winckler, 1960). Thus, equatorial field measurements and Geiger tube measurements of the peak intensity occur in the same region of space and are essentially simultaneous. The peak of the outer zone as detected by the other two instruments was displaced slightly from 24,000 kilometers (Fan, Meyer, and Simpson, 1960; Farley and Rosen, 1961).

During the storm main phase, there was a substantial decrease in the count rates of the University of Minnesota and University of Chicago experiments, followed by a large increase in the particle fluxes during the recovery phase of the storm. This behavior apparently is characteristic of the outer zone during a magnetic storm and has been observed by similar instruments on other satellites. The scintillator data departs from the general tendency during the main phase.



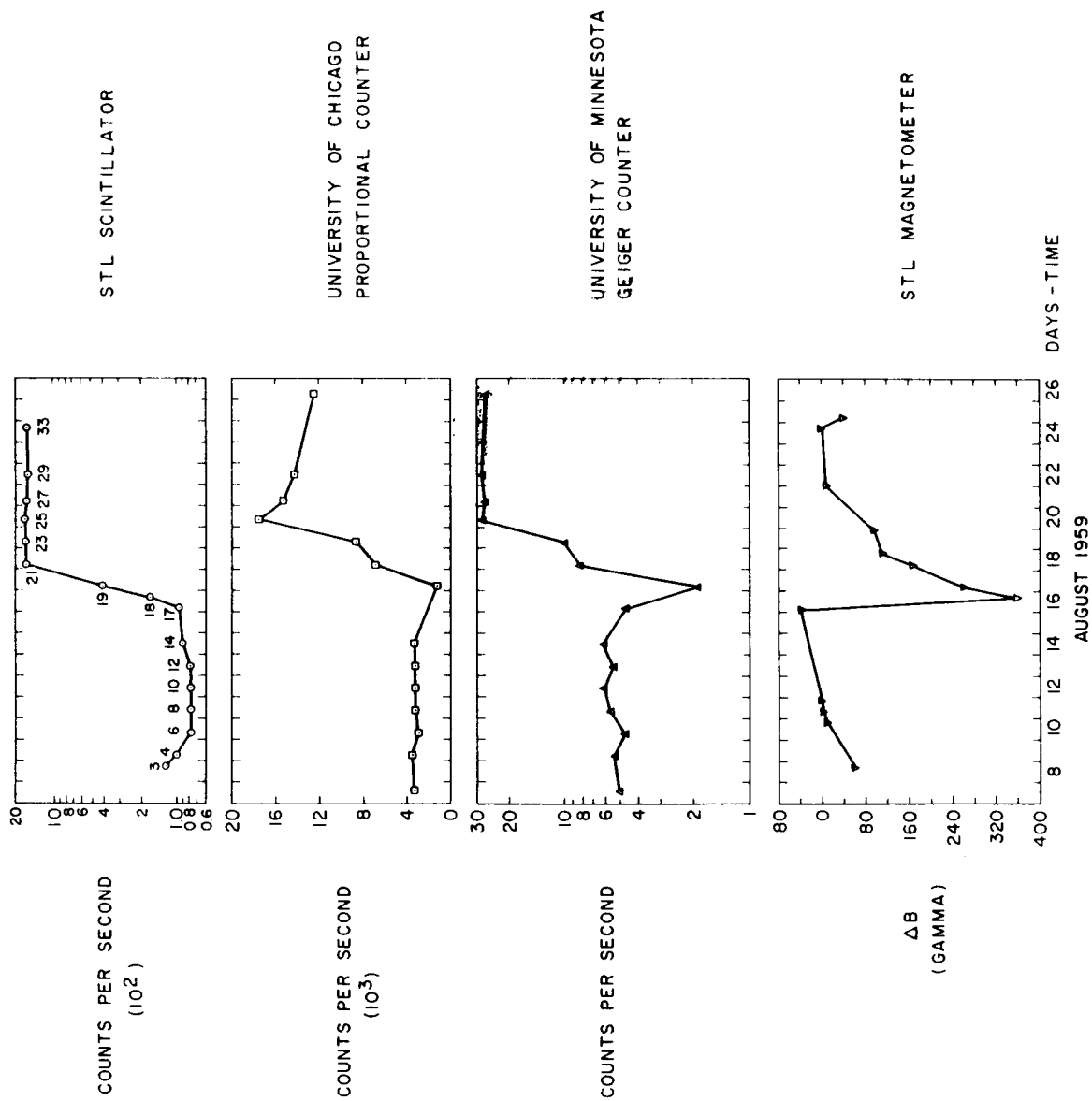


Figure 18. Comparison of Equatorial Magnetic Field Variations at  $h_F$  with Simultaneous Variation in the Three Explorer VI High Energy Particle Detectors.

Figure 18 shows that the slow variations in particle intensity correlate with the variations in field magnitude at  $4R_E$ . The count rates of the Geiger Tube and Proportional Counter decrease when the field magnitude decreases and the scintillator count rate increases slightly. When the field at  $4R_E$  recovers from the effect of the storm, and returns to its pre-storm value, all three particle count rates increase. However, the peak intensities in the outer zone are an order of magnitude larger than their pre-storm values.

#### SUMMARY

The experimental data can be summarized as follows:

- 1) Long period time dependent changes in the distant field coincided with  $D_{st}$  at the surface.
- 2) The magnitude of the main phase decrease in  $B_{\perp}$  at  $\sim 4R_E$  was several times larger than it was at the surface.
- 3) Irregular field fluctuations, with periods exceeding one minute, were observed during the storm. The largest fluctuations correlate with the occurrence of transient, storm variations observed at the surface near the polar regions.
- 4) Variations in the direction of the field at  $\sim 7R_E$  correlate with half-day variations in (a) the horizontal component of the surface field, and (b) the three hour, planetary K index.
- 5) The large scale perturbations of  $B_{\perp}$  and  $\phi$  during the storm were qualitatively similar to the perturbations observed previously on non-storm days.

6.) The  $D_{st}$  variations in the field magnitude at  $4 R_E$  correlate with changes in the peak intensity of the outer radiation zone measured by three, high energy particle detectors on Explorer VI. Two detectors show a decreased intensity during the storm when the field magnitude is depressed. All three detectors measured peak intensities which exceed the pre-storm values at the same time that the field magnitude returns to its quiescent value.

## DISCUSSION

The Explorer VI observations extend our knowledge of geomagnetic storm fields to points of observation far above the earth's surface. Such data can be used to test the validity of the various magnetic storm theories.

The Explorer VI storm data at 4 to 8  $R_E$  and the world wide component of the surface storm field ( $D_{st}$ ) have the same time dependence. Furthermore, the variations at one, four, and seven earth radii are essentially simultaneous, i.e., possible time delays are much less than the characteristic period of the  $D_{st}$  variation. During the storm the earth was immersed in a large scale magnetic field that was manifest at the surface as the main phase decrease.

### Characteristics of the Large Scale Storm Field

The characteristics of the  $D_{st}$  field at the earth's surface can be described simply. The  $D_{st}$  field has approximately the same magnitude and direction (antiparallel to the earth's axis of rotation) over the entire surface. It is the kind of uniform field that could be produced by a spherical current distribution concentric with the earth or by a toroidal current having a dimension of several earth diameters.

Ideally, a complete description is desired of the magnitude and direction of the  $D_{st}$  field in the space surrounding the earth. However, a complete description is not possible from a single orbiting satellite. It is particularly difficult to distinguish between a radial dependence and a dependence on latitude or longitude when the trajectory is a highly inclined ellipse like the Explorer VI orbit. In addition, useful data from the Explorer VI magnetometer is restricted to portions of the orbit where the magnitude of the disturbance field was at least several percent of the magnitude of the unperturbed geomagnetic field (as discussed above).

We can, however, infer several important properties of the large scale storm field from the Explorer VI data. Future magnetometer experiments will extend and improve this description.

1. A lower bound can be placed on the radial extent of the storm field. An attempt to establish the characteristic dimension of the  $D_{st}$  field is related to problems involving how much of the magnetosphere is occupied by the storm field and how the storm field inside the magnetosphere is allied to large scale storm fields in interplanetary space (Coleman, Davis, and Sonett, 1961). If the  $D_{st}$  field fills the geomagnetic cavity, the characteristic dimension will depend on the shape of the cavity and may be significantly different along, and transverse to, the earth-sun direction.

The longest dimension of the  $D_{st}$  field must have been  $7R_E$  at least, since a correlation with the surface  $D_{st}$  field was observed at that radial distance (see figure 17). As discussed below, it is evident that the Explorer VI orbit was entirely confined to the earth's magnetosphere. We are only able, therefore, to place a lower bound on the largest dimension of the magnetosphere during the storm, i.e., Explorer VI apogee ( $8R_E$ ). The observed correlation is consistent with the extension of the storm field throughout the entire magnetosphere. Since the boundary of the cavity was not penetrated, we cannot investigate the possible connection between the disturbed geomagnetic field inside the cavity and the interplanetary field outside it during the storm.

The evidence that the Explorer VI orbit was inside the magnetosphere is the following:

(1) In the vicinity of  $4 R_E$  with the spacecraft near the magnetic equator both the magnitude of the field ( $\sim 600\gamma$ ) and its geographic dependence are

typical of the geomagnetic field. Furthermore, the coherent variations in  $\phi$  and  $\phi_G$  from orbit to orbit (see figures 9 through 12) show that the location of the spacecraft in geomagnetic coordinates, as indicated by the field direction, followed closely the rotation of the earth's dipole field.

The spacecraft was evidently also inside the magnetosphere at larger radial distances.

- (1) There is no indication in the phase data (which provide the most complete data coverage throughout the storm interval) that the spacecraft ever penetrated an interface. The Explorer X (Heppner, Ness, Skillman and Searce, 1962) and Explorer XII (Cahill, 1962) magnetometer data show a marked change in the direction of the distant field at the magnetopause. However, the dependence of  $\phi$  on radial distance in figures 9 to 12 is essentially smooth. In addition to studying the geographic variations we can also compare the day to day variations in  $\Delta\phi$ . The storm data are qualitatively consistent with the non-storm phase data. During quiet intervals, e.g. 27 August, the small  $\Delta\phi$  clearly indicates that the spacecraft was confined to the magnetosphere.
- (2) Temporal variations in  $\Delta\phi$  at 40,000 kilometers correlate with variations in the magnitude of the surface field. The simplest explanation is that the perturbed geomagnetic field was measured at both locations.
- (3) Model calculations, to be presented below, can account for the qualitative features of the storm data along the trajectory. The magnitude of the superposed disturbance field so derived is less than  $G$  all along the Explorer VI orbit.

(4) Explorer VI high energy particle measurements show that the outer zone extended to geocentric altitudes of at least 40,000 kilometers. (e.g. see Rosen, Farley, and Sonett 1960, figure 7).

2. Near the equatorial plane at  $4 R_E$ , the storm field was directed southward, was apparently aligned with the local magnetic meridian plane, and had a magnitude of  $\sim 350\gamma$ .

At certain points of observation, symmetry properties can simplify the description of the distant vector magnetic field. Thus, if D is antiparallel to G on the magnetic equator, a single, scalar measurement completely specifies the resultant field, B. Such simplification depends on whether or not D causes a rotation of the geomagnetic field near the equator.

There are definite implications in the Explorer VI data regarding large angular rotations of the geomagnetic field near the equator. At 24,000 kilometers,  $\theta_M$ , the angle between the spacecraft spin axis and the normal to the local magnetic meridian plane, was approximately 105 degrees. The spin axis was nearly contained in the meridian plane. Consequently, field rotations out of, or transverse to, magnetic meridian planes were readily detected. Conversely, along this part of the orbit, the phase angle was insensitive to rotations confined to magnetic meridian planes, which would leave  $\phi$  equal to  $\phi_G$ . The phase data (figures 9 through 12) show that  $\Delta\phi$  did not exceed  $8^\circ$  during the storm. Therefore, any component of field rotation out of the magnetic meridian plane was small. Stated another way, at  $4 R_E$  near the equator, toroidal components of the disturbance field, were either small or entirely absent.

Can the changes in  $B_\perp$  (figure 6) be explained by a rotation of the field within the magnetic meridian plane? Near the geocentric distance of 24,000 kilometers, the spacecraft spin axis was nearly perpendicular to G. Thus, in the absence of a disturbance field,  $B_\perp$  was approximately the total field

magnitude,  $G$ , near the equator. (Note that  $|G_{\perp}| \approx |G|$  in figure 5.) The 350% decrease in  $B_{\perp}$  during the main phase implies a reduction in the magnitude of the field component parallel to  $G$  by a factor of approximately 2. Assuming that the field rotated without a change in magnitude implies a rotation of 60 degrees. This would produce a resultant field with a large radial component near the equator. Such a field would differ greatly from the geomagnetic field. It would correspond for example, to an interplanetary field, or a strongly deformed magnetic tail existing at 24,000 kilometers and lying in a magnetic meridian plane. The experimental evidence discussed above makes it almost certain that the Explorer VI was inside the geomagnetic field, particularly at 24,000 kilometers. Therefore, it seems reasonable to conclude that the decrease in  $B_{\perp}$  is primarily a decrease in magnitude, that  $B$  and  $G$  were parallel near the equator, and that  $\Delta B(t)$  in figure 6 is approximately the magnitude of the time varying storm field near the geomagnetic equatorial plane. Small deviations in field direction can not be ruled out but are not an essential feature of the arguments presented here.

Since  $\Delta B$  is negative, the storm field is southward at  $4 R_E$  and at the earth's surface. This qualitative observation implies that the primary storm current causing the  $D_{st}$  field was not located in the ionosphere, since the disturbance field above a westward current is directed northward. The Explorer VI data agree with Vanguard III storm data (Heppner, Stolarik, Shapiro, and Cain, 1960, 1962) which showed a tendency for the field above the ionosphere (at  $2 R_E$ ) to be decreased during the main phases of several moderate storms. If the southward directed storm field was caused by a ring current, most of the westward component of the current must have been located at geocentric altitudes above  $4 R_E$ .



3. The measurements on the magnetic equator at 1 and 4  $R_E$  show that the storm field was strongly dependent on altitude.

The magnitude of the main phase  $D_{st}$  field was 360 $\gamma$  at 4  $R_E$  and only 140 $\gamma$  at the surface. The magnitude of the primary disturbance field at the surface was actually less than 140 $\gamma$ . Earth currents induced by the slow  $D_{st}$  variations increase the magnitude of the disturbance field at the earth's surface because such currents tend to exclude the field from the earth's interior. Conversely, currents induced in the ionosphere tend to screen the earth's surface from the primary  $D_{st}$  field. However, the effective conductivity of the total ionosphere ( $10^{-3}$  to  $10^{-4}$  mho/meter) is too small to permit it to shield the earth effectively from slow magnetic variations. Analysis has shown that approximately three-tenths of the  $D_{st}$  field is due to currents inside the earth (Chapman and Bartels, 1940, p. 697 and Dessler and Parker, 1959). Therefore, the primary storm field at 1  $R_E$  was 30 percent less than 140 $\gamma$  or approximately 100 $\gamma$ .

The  $D_{st}$  field at the surface is independent of longitude. In the magnetosphere at 4  $R_E$  and beyond, however, the equatorial disturbance field may be asymmetric. A ring current could generate a longitudinally symmetric storm field, but if the magnetosphere is tear-drop shaped, or if the storm field is caused by currents near the boundary, the character of the equatorial disturbance field could differ greatly from one longitude quadrant to another. The Explorer VI data establish the radial dependence of the equatorial field in a meridian which is almost perpendicular to the earth-sun direction on the evening side of the earth (see figure 14).

Since the Explorer VI orbit was apparently confined to the interior of the geomagnetic cavity, a bound can be placed on the magnitude of the equatorial disturbance field at 8  $R_E$  (Explorer VI apogee) for  $\lambda_s \approx 120^\circ$ . If the storm

field was southward at this distance, its magnitude must have been less than  $60\gamma$ , the magnitude of the unperturbed, northward directed, geomagnetic field. This inference is supported by the model calculations which indicate that  $D$  is less than  $G$  and is southward at points of observation below the equatorial plane at  $8 R_E$ .

A lower bound can also be placed on the equatorial disturbance field along the evening meridian at greater radial distances if the magnetosphere is assumed to have extended to at least  $8 R_E$  at  $\lambda_s \approx 90^\circ$ . If the storm field was southward, its magnitude was less than  $60\gamma$  as above. If the storm field was northward at  $8 R_E$  an even stronger dependence on altitude is implied (see figure 19).

4. At greater radial distances, with the satellite below the equatorial plane, the characteristics of the storm field agree qualitatively with model calculations employing a quasiuniform magnetic field that is confined to magnetic meridian planes. Magnetometer data ( $B_{\perp}$  and  $\phi$ ) obtained on August 16, 17, and 18, are shown in Figure 20 in the restricted altitude range from 30,000 to 50,000 kilometers. The results of a model calculation are also included. The theoretical calculations are based on a circular current loop having an infinitesimal cross-section. The source of the field is described in terms of  $R_0$ , the radial distance from the earth's center to the current, and  $I$ , the magnitude of the current. The results of superposing the perturbation field due to this current on the unperturbed geomagnetic field are shown for a single set of parameters, which correspond to the best fit for each of the three days. The best fit was obtained by varying  $R_0$  and  $I$  in a systematic way and choosing the results which most closely approximated  $B_{\perp}$  and  $\phi$ . Calculations using the current model applied previously to the non-storm data

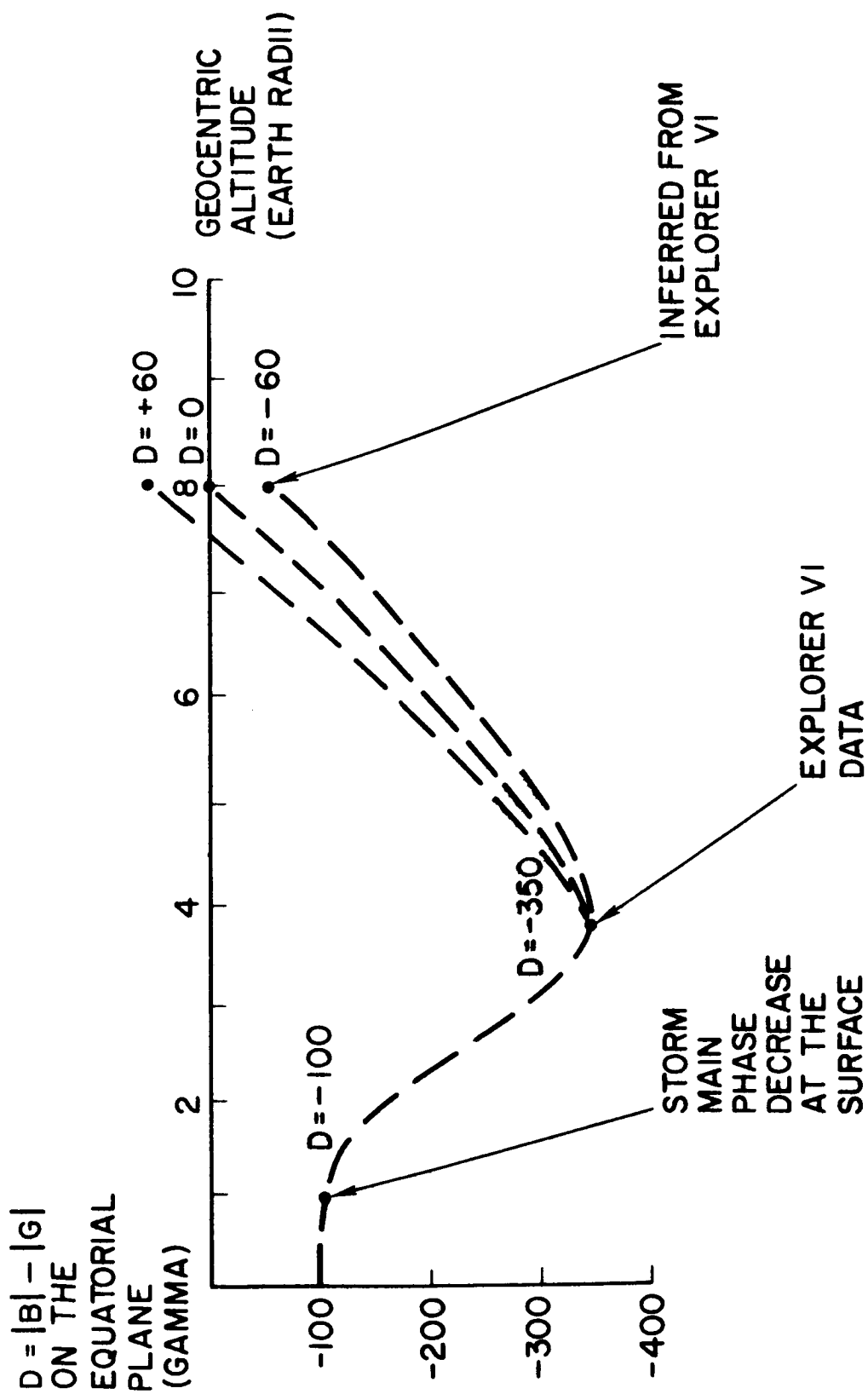


Figure 19. Radial Dependence of the Disturbance Field Inferred from Satellite and Surface Data.

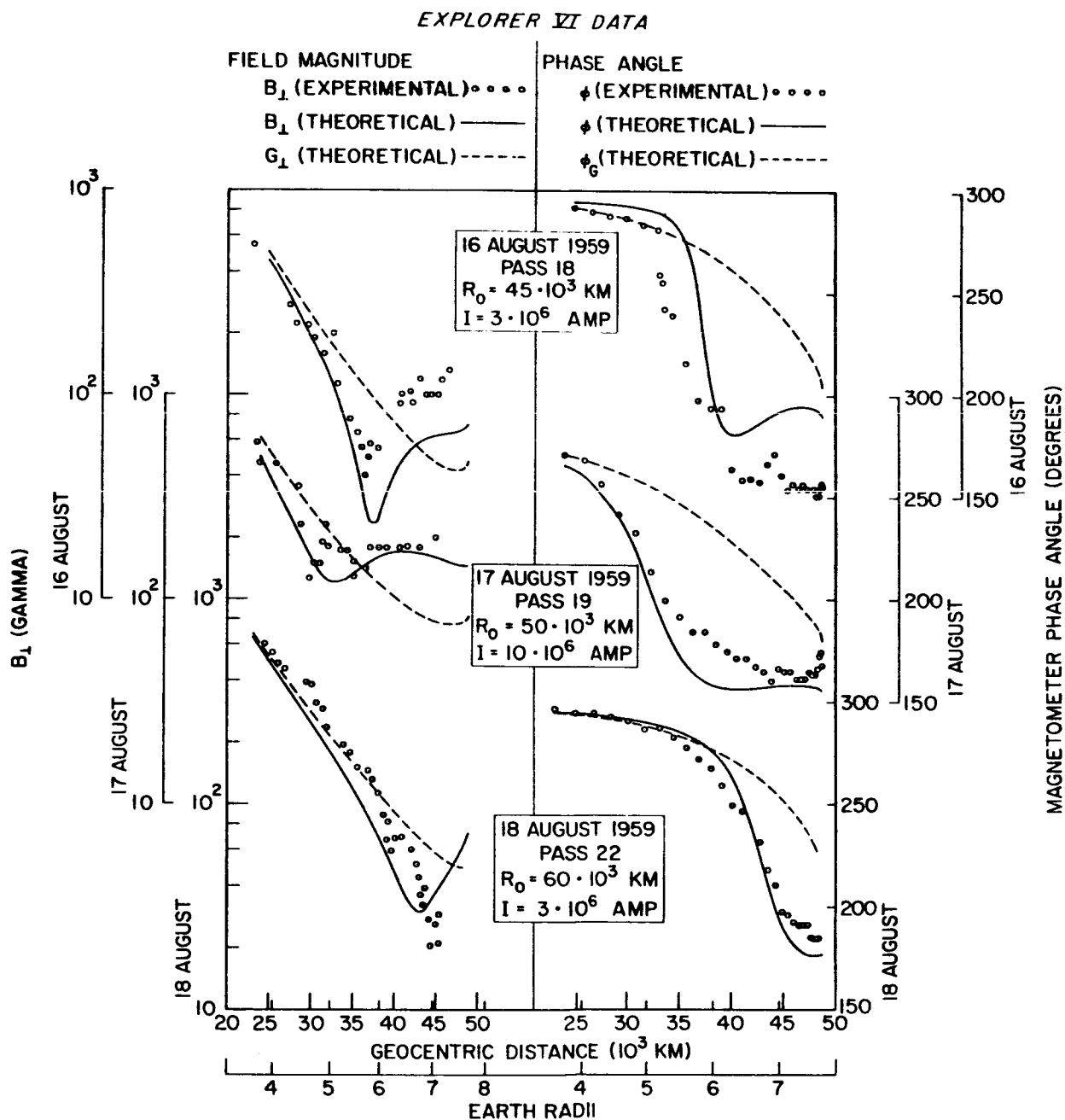


Figure 20. Results of Model Calculations Employing a Circular Current Loop Compared with Explorer VI Data.

(a longitudinal current located at  $R_0$ , having a finite circular cross sectional area  $\pi a^2$ , and a total current  $I$ ) were also carried out. However, they did not agree with the data any better than the infinitesimal loop, which can be described by one less parameter. For the present discussion, the physical significance of the current source is not critical. The filamentary current loop is a convenient source of a large scale, quasiuniform magnetic field, which is symmetric above and below the equator, and which is confined to magnetic meridian planes.

5. Inspection of the magnitude data and phase angle data shows that the storm field is qualitatively similar to the disturbance field reported previously for non-storm periods (Smith, Coleman, Judge, and Sonett, 1960).

The characteristics of the disturbance field during storm and non-storm intervals as inferred from model calculations, are similar. The storm field may simply be an enhancement of the non-storm disturbance field.

Studies of the surface geomagnetic field suggest a continuity between storm and non-storm conditions. In 1916, Schmidt postulated that a ring current causes the main-phase decrease. To explain why the surface field continued to increase slowly for many days following the end of the storm, he proposed that the ring current was a persistent feature of the distant field. Recent statistical studies by Chernosky (1962) indicate that the magnetic storm proper (which is defined in terms of K indices, i.e, fluctuation phenomena) is part of a phenomenon that persists for at least 5 days.

The satellite data show that the distant field is indeed deformed during both quiet periods and storm periods. The same general departure from the extrapolated geomagnetic field is present in varying degrees in all the analyzed Explorer VI data (19 days and 32 orbital passes).

## Origin of the Large Scale Storm Field

At the present time there are two prevalent explanations for a large scale magnetospheric storm field. One involves a ring current while the other involves deformations of the magnetosphere by solar plasma. Analysis of surface measurements has shown that the  $D_{st}$  field is also consistent with a spherical system of currents located just above the earth's surface, perhaps at ionospheric levels (see Chapman and Bartels 1940). The discussion above rules out ionospheric currents as a possible cause of the primary  $D_{st}$  field.

A ring current has been the common feature of most magnetic storm theories. A toroidal geocentric current loop is undoubtedly the simplest current configuration that could produce a large scale, quasi-uniform magnetic field surrounding the earth. Singer (1957) extended Alfvén's discussion of the drift motion of particles moving through the inhomogeneous geomagnetic field (Alfvén, 1950) in trapped, Störmer orbits. The spiral motion of the trapped charged particles about the lines of force is superposed on a gradual drift motion concentric with the earth. Singer derived particle drift velocities on the basis of forces exerted by the earth's field gradient, although his numerical results implicitly included the contribution to the drift caused by the curvature of the geomagnetic field lines. Dessler and Parker (1959) derived an explicit relation between field curvature and particle drift velocity and called attention to another contribution to the ring current, which had also been discussed by Alfvén, namely, the diamagnetism of the trapped plasma. These matters are discussed in greater detail in a recent review article (Smith, 1962).

Thus, the mechanism by which a ring current may be established is well understood. If plasma becomes trapped in the geomagnetic field, a ring current will result. Recent advances in ring current theory are directed at derivations of the currents and fields associated with specific models of the trapped-particle distribution function (Akasofu and Chapman, 1961, Apel, Singer and Wentworth, 1962, Akasofu, Cain and Chapman, 1961).

The generation of the  $D_{st}$  field within the magnetosphere by hydromagnetic deformation is a modern concept. Piddington has proposed an alternative to the ring current that involves the formation of a geomagnetic tail pointing away from the sun (Piddington 1959, 1960, 1962). He argues that at the solar plasma-geomagnetic field interface earth's field lines diffuse into the streaming plasma and are transported around to the rear of the earth. The diffusion of magnetic flux out of the magnetosphere could cause a net decrease in field strength. The hydromagnetic redistribution of the geomagnetic field lines inside the cavity may lead to a disturbance field having the same symmetry near the earth as the dipole field. At the present time, the formulation of the magnetic tail theory is primarily qualitative. Quantitative estimates are available for the shape of the cavity (Harrison, 1962) but not for the disturbance field inside the magnetosphere.

Both the ring current and deformed magnetosphere theories depend on stresses involving the geomagnetic field and solar plasma. These two alternatives may not be mutually exclusive. The basic question is whether the solar particles or the geomagnetic field lines cross the interface. The mechanism of diffusion proposed by Piddington to remove magnetic flux was proposed by Dessler and Parker (1959) to trap solar plasma. If the magnetic pressure and plasma pressure are approximately equal at the interface as anticipated, both

mechanisms may operate. A ring current and magnetic tail may occur simultaneously. The recent storm theories of Dungey (1960) and Axford and Hines (1961) imply both a deformed magnetosphere and a ring current. Dungey invokes neutral points to get solar plasma into, and out of, the cavity. Axford and Hines postulate a viscous-like interaction at the boundary that convects plasma into the magnetosphere from the tail. In these two theories, the solar plasma is not actually trapped in stoermer orbits, but currents equivalent to a ring current develop as the plasma drifts through the geomagnetic field. This feature of the theories is similar to Alfven's magnetic storm theory (Alfven 1940) which utilized large scale electric fields to get the solar particles into the earth's dipole field.

The characteristics of the storm field derived above are qualitatively consistent with the existence of a ring current. A disturbance field that is strongly dependent on altitude, confined to magnetic meridian planes, and dominated by the geomagnetic field may be due to a ring current. However, it is not obvious that these characteristics are inconsistent with a field caused by a deformation of the magnetosphere. During non-storm intervals the disturbance field detected by Explorer X (Heppner, Ness, Skillman, and Searce, 1962) at geocentric altitudes out to  $22 R_E$  tended to lie inside magnetic meridian planes (Smith, 1962) although the data are more consistent qualitatively with the existence of a magnetic tail than with a ring current.

The basic difference between the theoretical alternatives is the presence or absence of trapped plasma inside the magnetosphere. Therefore, the best way to decide which explanation is correct is by simultaneous particle and field measurements.

The Explorer VI contained three high energy particle detectors designed to study the radiation zones. Unfortunately, the scientific experiments did not include a low energy particle detector. The behavior of the high energy particle



detectors during the storm when compared with the magnetometer data (figure 18) shows that the trapped high energy radiation particles did not cause the  $D_{st}$  field. The simultaneous variation of the particle count rates and the magnetic field shows a general "in-phase" correspondence. The University of Chicago and University of Minnesota particle fluxes decrease when the field decreases and they increase when the field increases. This is contrary to the expectation that the energy of the ring current particles is maximum when the field is minimum, i.e., during the main phase, and that the recovery phase is associated with a loss of particle energy. Although the scintillation count rate increases slightly during the main phase, the experiment shows an even greater increase during the recovery phase. This behavior, is also inconsistent with the hypothesis that the radiation particles represent an important constituent of a main phase ring current.

Low energy particle detectors have been flown on spacecraft other than Explorer VI.

(1) An ion trap on Lunik spacecraft measured fluxes of particles with energies greater than 200 ev (Gringauz, Kurt, Moroz, and Shklovskii, 1960). From 20,000 to 55,000 kilometers geocentric altitude the observed particle fluxes are accounted for by the high energy particles of the outer radiation zone. However, low energy electrons were detected in the region from 55,000 to 75,000 kilometers. Gringauz and Rytov (1960) reconciled these measurements with the existence of a current in the same region of space suggested by Explorer VI and Pioneer V model calculations (Smith, Coleman, Judge, and Sonett 1960) by using the drift current theory. However, as Dessler and Karplus (1961) pointed out, it was necessary to assume that large numbers of low energy ( $\sim 20$  ev) electrons were present that were not actually detected by the ion traps.

(2) The Explorer X plasma probe (Bridge, Dilworth, Lazarus, Lyon, Rossi, and Scherb 1961) found an absence of protons with energies between 5 and 2300 ev in the altitude range from 20,000 to 140,000 kilometers. Simultaneous magnetometer data showed that the characteristic deviation of the distant geomagnetic field seen by the Explorer VI magnetometer was present. This result is consistent with the magnetic tail theory. However, the observations were made during a non-storm interval. Furthermore, the plasma probe was not designed to detect low energy electrons which might be the cause of a ring current (Singer, 1962).

(3) Explorer XII low energy proton measurements (Bader, 1962) are consistent with the results described above. There was a marked absence of protons in the energy range between 100 ev and 20 kev at geocentric altitudes of less than 85,000 km ( $13 R_e$ ). A substantial flux of 100 kev protons was detected by Davis and Williamson (1962). However, the disturbance field associated with these trapped particles is small according to calculations carried out by Akasofu, Cain and Chapman (1962).

To summarize these results, the plasma data favors the absence of large numbers of low energy protons inside the magnetosphere. However, information regarding the presence of low energy electrons is incomplete and the particle measurements do not conclusively eliminate a ring current as the cause of the  $D_{st}$  field.

If only the Explorer VI magnetic field data are considered, the fundamental problem becomes to derive the current system corresponding to the observed disturbance field. This general problem has not been attacked theoretically except for points of observation on the equatorial plane (Apel, Singer, and Wentworth 1962). However, the magnitude of the disturbance field detected

by the Explorer VI magnetometer is only known at two points of observation on the equatorial plane, one of which is at the earth's surface (See figure 19).

The alternative problem has received considerable theoretical treatment i.e., given the characteristics of the trapped particles, what are the current density of the ring current and the accompanying disturbance field? It is, therefore, possible to perform model calculations based on plausible physical models. Model calculations can presumably establish whether or not the data are consistent with the existence of a ring current.

To specify a diamagnetic ring current it is necessary to know the phase space density distribution function of the trapped plasma. Unfortunately, as discussed above, the distribution function is unknown. Consequently, ring current disturbance field calculations based on plasma theory have involved particle distributions chosen because of their mathematical simplicity. Akasofu and Chapman (1961) utilized a separable distribution function,  $n(r_e) f(v)$  where  $r_e$  is the equatorial radius and  $f(v)$  is specified by the energy and pitch angle distribution of the particles.  $n(r_e)$  was assumed to be a Gaussian function. Apel, Singer and Wentworth (1962) made similar assumptions but used a different  $n(r_e)$ . These calculations were carried out for points of observation on the geomagnetic equatorial plane. Furthermore, the calculations were not self consistent [See discussion by Beard (1962) and Akasofu (1962)], the particles were assumed to be monoenergetic, and only numerical results are available that apply to specific particle distributions located in definite regions of the magnetosphere.

In the past, these limitations, particularly the inapplicability of the calculations to satellite trajectories, led us to employ simple current models such as the circular current loop described above. The limitations of the

ad hoc models that were used are obvious from the standpoint of plasma theory.

The circular current loop, undoubtedly, lacks physical significance. The model consists of a current filament having an infinitesimal cross sectional area. A real ring current would presumably occupy a relatively large volume of space. The current density must be low, if the energy density of the disturbance field is to be less than the energy density of the geomagnetic field. However, large currents ( $\sim 10^6$  amps) are required in order to produce a main phase decrease of  $100\gamma$ .

This expectation is evidently supported by the experimental data at geocentric distances of 30,000 km and beyond (figure 20). The altitude dependence is unsatisfactory and the implicit time variation of the field at the earth does not agree with the surface measurements. Current loops at 45,000 to 60,000 km cannot produce a disturbance field of  $\sim 100\gamma$  at  $1 R_E$  and  $\sim 350\gamma$  at  $4R_E$ . The equatorial surface field ( $\frac{\mu_0 i}{2a}$ ) for 16, 17, 18 August computed from the parameters appearing in figure 20 are  $-40$ ,  $-125$ , and  $-30\gamma$ . However, the observed fields are  $-100$ ,  $-85$ , and  $-15\gamma$ , respectively.

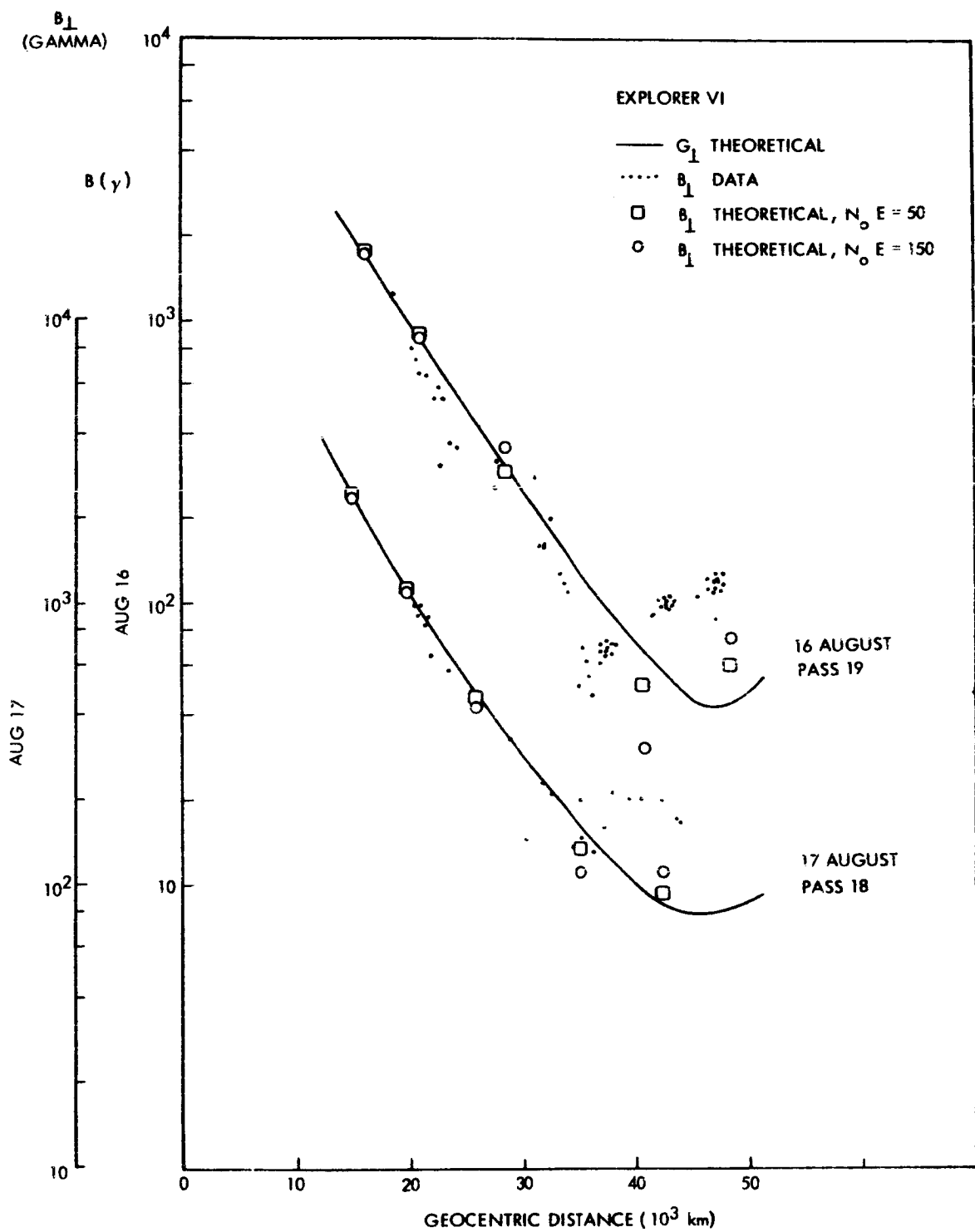
Thus, the usefulness of these particular model calculations is restricted to the concomittant disturbance field. The field due to the filamentary loop apparently approximates the actual disturbance field along the portion of the flight path near apogee.

More realistic trapped particle ring current models have recently been developed that overcome some of the limitations mentioned above. Akasofu, Cain, and Chapman (1961) extended the Akasofu and Chapman calculations to points of observation above and below the equatorial plane. An attempt was also made to establish the self consistency of the calculations apparently with encouraging results. The numerical results of Akasofu, Cain, and Chapman

are compared with the Explorer VI data in figure 21. The magnitude of the disturbance field is proportional to the particle energy density at the distribution maximum,  $n_0 E$ . Two values of  $n_0 E$  are shown, 50 and 150 kev cm<sup>-3</sup>. The latter value, which was employed by Akasofu, Cain and Chapman, produces a region in which the earth's field gradient is reversed. According to Apel, Singer and Wentworth, this may be a possible self consistent field configuration. The Akasofu, Cain, and Chapman disturbance field is obtained by numerical calculations and the other parameters that specify the number density and pitch angle distribution functions of the trapped particles cannot be varied. In this model most of the trapped particles lie between 4 and 8  $R_E$  with the maximum density occurring at 6  $R_E$ .

Figure 21 shows that these model calculations also agree qualitatively with the Explorer VI data. Large values of  $n_0 E$  produce the best agreement. Presumably, energy densities exceeding 150 kev cm<sup>-3</sup> are required to produce the observed  $\phi$ . The computed and measured phase angles correspond more closely than the theoretical and experimental values of  $B_1$ . This suggests that the variation in the direction of the theoretical field is more nearly correct than the variation in magnitude. It was noted above that the Explorer VI data are consistent with a stretching of the lines of force of the geomagnetic field.

We have not attempted to obtain the best fit to the data using the Akasofu, Cain, and Chapman model. Experience with other models has shown that increasing the magnitude of the current in order to yield a better fit near 30,000 to 40,000 km will cause larger deviations at greater altitudes and higher latitudes. Furthermore, the Akasofu, Cain, and Chapman ring current cannot account for the Explorer VI data obtained near the geomagnetic equatorial plane. The numerical results applicable to points of observation on the equator show that



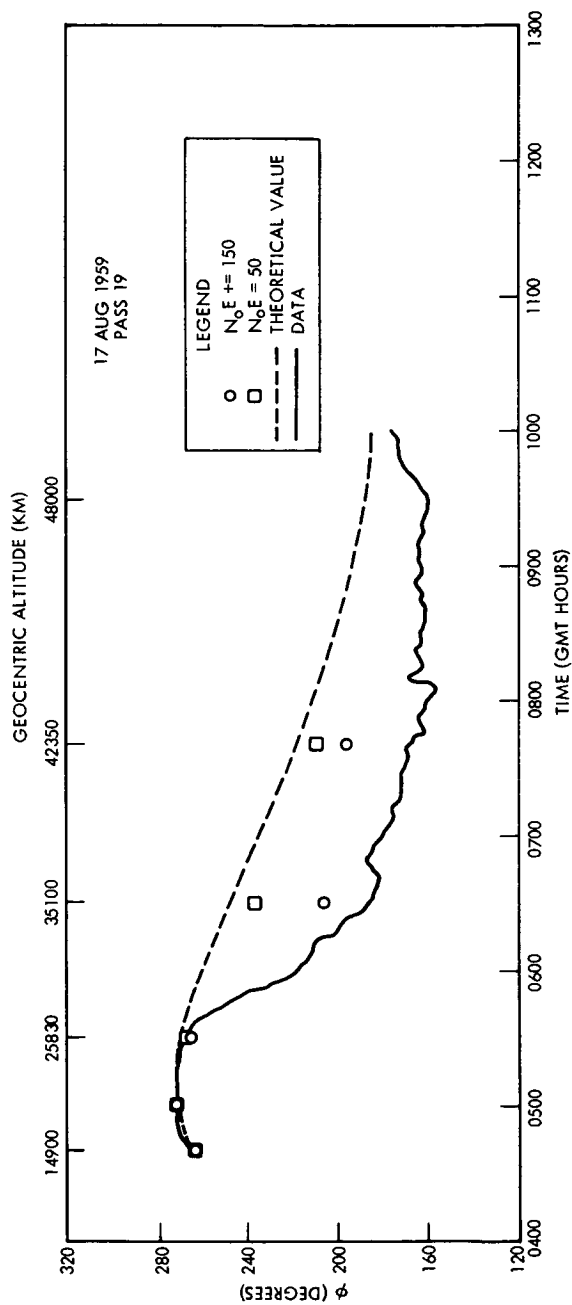
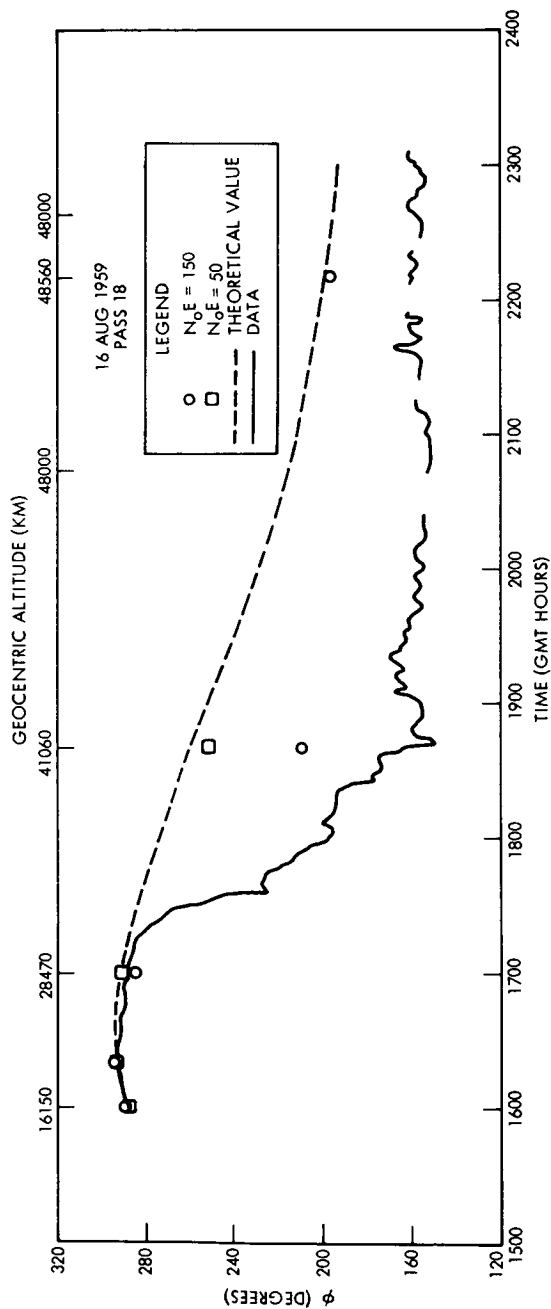


Figure 21B. Comparison Between the Akasofu, Cain, and Chapman Ring Current and the Explorer VI Storm Data.

the magnitude of the disturbance field at  $4R_E$  only slightly exceeds its magnitude at  $1 R_E$ . A ratio only slightly greater than one is predicted (see figure 2 of Akasofu, Cain, and Chapman) but the actual ratio was approximately 3.5 to 1. Therefore, a ring current of this type, centered at  $6R_E$ , cannot account for all features of the  $D_{st}$  field.

Our attempts to see if the data are consistent with a  $D_{st}$  field due to a ring current may be summarized as follows. The Explorer VI data beyond  $5R_E$  are qualitatively consistent with ring current fields, although no specific current model has been found that can account quantitatively for the observations. However, the results are ambiguous in that the current needed to account for the high altitude observations will not produce the large field decrease that was actually observed at  $4R_E$ . The latter may mean that the peak in the particle intensity was located at  $\sim 4R_E$  but that there was a large current component at altitudes out to 6 to  $10 R_E$ .

The characteristics of the large scale  $D_{st}$  field may also be consistent with the formation of a magnetic tail. Theoretical estimates of the disturbance field associated with such a tail have not appeared in the literature. The most prominent qualitative features of the resultant field in the usual diagrams of an asymmetric magnetosphere are (1) a region in which field lines that intersect the earth's surface at high latitude cease to corotate with the earth, and (2) a region in which resultant field lines point away from the earth in an antisolar direction.

The data presented above show that the distant field corotates out to at least  $4 R_E$ . However, corotation is expected to persist out to altitudes at which the field lines intersect the earth's surface in, or near, the auroral zones. This probably implies that corotation occurs as far out at 7 to  $10R_E$ .



It is difficult to use the Explorer VI data to investigate corotation at greater altitudes because of the large departures of  $\phi$  from  $\phi_G$  and significant temporal variations (indicated by the correlation between  $\Delta\phi$  and the surface field, figure 17).

A field directed away from the sun would produce a phase angle equal to  $180^\circ$ . Although phase angles are observed that have this value, there is no evidence of a persistent, or recurrent, tendency for the observed field to assume such an orientation. Since the Explorer VI measurements are restricted to geocentric distances of less than  $8 R_E$ , this result neither confirms nor contradicts the existence of a magnetic tail.

### Acknowledgements

This work was supported financially by the National Aeronautics and Space Administration under contract NASw-270. We are grateful to Space Technology Laboratories, Inc. and particularly the Space Physics Department and Dr. Alan Rosen, for their cooperation and assistance in the performance of this task. Technical assistance was provided by J. Kinsey, N. Lyke, and G. Komatsu, of the Space Physics Department and by I. Kliger and P. Lipinski of the Computation and Data Reduction Center.

We want to express our appreciation also to our colleagues, P.J. Coleman, Jr. who was closely involved in the initial effort to reduce the phase data, to K. Moe for his careful refinement of the Explorer VI trajectory, to Prof. J. A. Simpson and Prof. J. Winckler for making ground station and satellite data available to us, and to Dr. A. J. Dessler and Dr. R. C. Wentworth for many helpful discussions regarding ring current theory.

Figure 1. Spacecraft Coordinate System

This is an artistic representation of the experiment geometry.  $\omega$  is the rotation axis of the spin stabilized spacecraft. The equatorial plane of the spacecraft is shaded and is perpendicular to  $\hat{\omega}$ .  $\hat{S}$  is a unit vector directed toward the sun and  $B$  is the magnetic field vector. The projections of  $S$  and  $B$  onto the equatorial plane are  $S_{\perp}$  and  $B_{\perp}$  respectively.  $\phi$  is the angle between  $S_{\perp}$  and  $B_{\perp}$ . The magnetometer measured  $|B_{\perp}|$  and  $\phi$  directly.

Figure 2. Block Diagram of the Search Coil Magnetometer

The experiment sensors are the search coil and a sun-sensing photodiode. The amplifier bandpass was centered at the spacecraft spin frequency. Automatic gain control extended the dynamic range of the amplifier. The phase comparator measured the time delay between zero-voltage crossings of the search coil sinusoid and pulses that were generated when the sun was within the narrow field of view of the photodiode. Two independent data processing systems were employed. Analog voltages were telemetered continuously as frequency modulated signals. The analog voltages were also digitized and binary numbers were transmitted upon ground command.

Figure 3. Projection of the Explorer VI Trajectory Onto the Earth

The geographic position of the spacecraft is shown at radial distances separated by 10,000 kilometers and at apogee. The positions shown are for the 18th orbit which occurred on 16-17 August.

Figure 4. Geomagnetic Activity during the Explorer VI Epoch

Half day averages of the planetary K index,  $K_p$ , are shown for 7 August to 15 September 1959. Half day averages are plotted because the orbital period

of the Explorer VI was approximately 12 3/4 hours. The major storms are indicated at the top of the figure. The abbreviations GC and SC stand for gradual commencement and sudden commencement storm. The length of the blocks indicate the duration of the storm. The blocks are dashed where uncertainty exists as to the exact duration.

Figure 5. Explorer VI Field Magnitude Data During the Magnetic Storm of 16-18 August

$B_{\perp}$  is shown as a function of geocentric distance for 3 orbits on 16, 17, and 18 August. Values of the total geomagnetic field,  $|G_{\text{total}}|$ , and the component perpendicular to the satellite spin axis direction,  $|G_{\perp}|$ , are also shown. From 3 to 4  $R_E$   $|G_{\perp}|$  and  $|G_{\text{total}}|$  are approximately equal because the Explorer VI spin axis is essentially orthogonal to the geomagnetic field vector. Although the absolute magnitude of the differences between  $|B_{\perp}|$  and  $|G_{\perp}|$  can be large at altitudes less than 3 earth radii, the relative differences are small at these low altitudes, especially when account is taken of the quasi-logarithmic characteristic of the magnetometer amplifier. The deviation between  $|B_{\perp}|$  and  $|G_{\perp}|$  at  $R > 5R_E$  first noted on non-storm days is also observed during the storm. Magnitude data ( $B_{\perp}$ ) are unavailable during much of the storm and much of the Explorer VI epoch. When the satellite was at large altitudes, it was difficult to obtain good quality ground station records because of the dynamic character of the sinusoidal output signal. Most of the useful magnitude data were acquired by the large radio telescope at Jodrell Bank, England. Conversely, the frequency modulated signal from the phase comparator varied slowly over the orbit and most of the phase data was recovered.

Figure 6. Time Variations of the Equatorial Disturbance Field Compared with  $D_{st}$  Variations at the Earth's Surface

The upper curve shows  $\Delta B = |B_{\perp}| - |G_{\perp}|$  near the geomagnetic equator at a geocentric distance of approximately  $4 R_E$  during the first two weeks of Explorer VI measurements. The data are normalized so that  $\Delta B = 0$  on 12 August (one of the magnetically quietest days of the month). The center curve shows the variation in the intensity of the horizontal component of the surface field at Huancayo, Peru ( $\delta_M = -0.6^\circ$ ). Daily averages are plotted at 1200 GMT for each day. The  $D_{st}$  curve for the SC Storm of 16 August is shown at the bottom of the figure. The  $D_{st}$  curve is the result of averaging the storm data from 12 geomagnetic observatories and was derived by S. Chapman and S.I. Akasofu.

Figure 7. Phase Angle Data During Storm and Non-storm Intervals

The phase angle,  $\phi$  is shown as a function of geocentric distance for orbits on 17 and 27 August and 4 September. The theoretical angle based on a spherical harmonic expansion of the surface field is also shown. 17 August and 4 September were storm days and 27 August was the quietest day of the month. The planetary  $A_p$  indices are given for each day. There are substantial changes in the character of the large scale deviation,  $\phi - \phi_G$ , between quiet and disturbed periods. In addition, during storm periods pronounced small scale irregular variations in  $\phi$  occur.

Figure 8. Qualitative Explanation of the Effect of a Disturbance field on the Phase Angle

The earth, a westward current, and the associated magnetic fields are shown. The spacecraft location is the point common to the vectors S, D, B, and G. For illustrative purposes we have assumed a simplified geometry in which the spacecraft, the field lines, and the sun vector, S, all lie in the plane of

the diagram. The spin axis,  $\omega$ , is assumed to be perpendicular to the plane of the diagram.  $\phi_G$  is the angle between S and the geomagnetic field vector, G.  $\phi$  is the angle between S and the resultant field, B, which is the vector sum of G and the disturbance field, D, caused by the westward current. Note that  $\phi$  is less than  $\phi_G$ , a qualitative feature of the Explorer VI data.

Figure 9. Phase Data Obtained during a Magnetic Storm (odd numbered passes)

The phase angle,  $\phi$ , is shown as a function of geocentric distance and universal time. The theoretical phase angle for the unperturbed geomagnetic field,  $\phi_G$ , is also shown.  $\Theta_M$  is the angle between the Explorer VI spin axis and the local magnetic meridian plane (see figure 13).  $\lambda_s$  is the angle between the projection of the spacecraft radius and the earth-sun direction onto the geographic equatorial plane (see figure 14). The arrow marked  $\delta_M = 0$  indicates where the spacecraft crossed the geomagnetic equator. Data is shown for two orbits, numbers 15 on 15 August and number 17 and 16 August. The odd numbered passes are presented together because their trajectories are similar in geomagnetic coordinates.  $\sum K_p$  is the sum of the planetary K indices during the 12 hours of each orbit. Note that the agreement between  $\phi$  and  $\phi_G$  at low geocentric altitudes represents a calibration check on the phase comparator data at high altitudes, where large deviations from the geomagnetic field direction are observed.

Figure 10. Phase Data Obtained during a Magnetic Storm (odd numbered passes)

The empirical phase angle and the theoretical angles presented in figure 9 are shown here for pass number 19 on 17 August and pass number 21 on 18 August.

Figure 11. Phase Data Obtained During a Magnetic Storm (even numbered passes)

The phase data and theoretical angles are presented for the two even numbered passes on 15 and 16 August.

Figure 12. Phase Data Obtained During a Magnetic Storm (even numbered passes)

The phase data and theoretical angles are presented for two even numbered passes on 17 and 18 August.

Figure 13. Representation of the Angle,  $\Theta_M$

The unit vector,  $\hat{e}_P$ , gives the direction of the geomagnetic field.  $\hat{e}_R$  is a unit vector passing through the center of the earth and the instantaneous location of the spacecraft.  $\hat{n}$  is the unit normal to the local magnetic meridian plane, i.e., the plane of the geomagnetic field line.  $\Theta_M$  is the angle between the normal to the magnetic meridian plane and  $\omega$ , the spacecraft spin axis.  $\Theta_M$  is useful in determining how sensitive the magnetometer is to disturbance field components lying inside, or perpendicular to, the magnetic meridian plane.

Figure 14. Representation of the angle,  $\lambda_s$

The sun-earth direction and Explorer VI radius vector are projected on the geographic equatorial plane.  $\lambda_s$ , the angle between these projections, describes the instantaneous orientation of the spacecraft with respect to the solar direction. The projected Explorer VI orbit for 16 August is shown as an example. The solid portion of the orbit lies above, and the dashed portion of the orbit lies below, the equatorial plane.

Figure 15. Geomagnetic Latitude of the Spacecraft (odd numbered passes)

The portion of the Explorer VI orbit between radii of 20,000 and 48,000 kilometers is shown for passes 15, 17, 19 and 21 on 15-18 August. The

triangle (digital data) and circles (analog data) mark the positions at which data used in figures 6 and 17 were obtained.

Figure 16. Geomagnetic Latitude of the Spacecraft (even numbered passes)

This figure contains the trajectory in spherical coordinates (geomagnetic latitude and radial distance) for passes 16, 18, 20, 22 (15-18 August). The circles mark the Explorer VI location where the data used in figures 6 and 17 were obtained.

Figure 17. Temporal Variation in the Phase Data at 40,000 Kilometers compared with the Surface Field

$\phi - \phi_G$  is the phase angle deviation, observed minus theoretical (corresponding to the unperturbed geomagnetic field).  $\phi - \phi_G$  is shown during the storm interval, 15-18 August. Each Explorer VI datum was obtained at a geocentric altitude of 40,000 kilometers irrespective of geomagnetic latitude (see figures 15 and 16).  $H$  is the variation in the hourly values of the horizontal intensity at Huancayo, Peru. The surface data shown are the average values of the horizontal component for the hour during which the Explorer VI data were obtained. The 3 hour K index, inverted so that K increases downward, is shown in the lower third of the figure. Note the correspondence between variations in the surface field and in the field direction at  $\sim 7R_E$  (40,000 km). Two storms are superposed. A gradual commencement storm that began 15 August was in the recovery phase when a sudden commencement storm began on 16 August.

Figure 18. Comparison of Equatorial Magnetic Field Variations at  $4R_E$  with Simultaneous Variations in the Three Explorer VI High Energy Particle Detectors

The time dependence of the peak counting rate per orbit of the scintillating crystal detector (STL) appears at the top. The variation in the counter



telescope (Univ. of Chicago) peak counting rate is shown as the next lower curve. The maximum count rate per orbit obtained by the Geiger counter (Univ. of Minnesota) as a function of time is given by the next lower curve. The magnetometer data appears at the bottom of the figure. The same data appears in figure 6.

Figure 19. Radial Dependence of the Disturbance Field Inferred from Satellite and Surface Data

$D$  is the difference between the magnitudes of the measured field,  $B$ , and the unperturbed geomagnetic field,  $G$ , for points of observation on the geomagnetic equator. The main phase decrease at the surface is  $100\gamma$  when corrected for currents induced in the conducting earth by the slow  $D_{st}$  variations. The main phase decrease at  $3.75 R_E$  is  $350\gamma$  as discussed in the text. The three values appearing at  $8 R_E$  (approximately Explorer VI apogee) corresponds to the vanishing of the  $D$  field ( $D = 0$ ), to a disturbance field that just cancels the unperturbed geomagnetic field ( $D = -60\gamma$ ), and to an arbitrary positive disturbance field equal to the magnitude of the dipole field at  $8 R_E$  ( $D = 60\gamma$ ). The latter three points show the apparent, strong dependence of  $D$  on geocentric altitude. However, a dependence on longitude, or solar orientation, could be implicit.

Figure 20. Results of Model Calculations Employing a Circular Current Loop Compared with Explorer VI Data.

$B_{\perp}$  and  $\phi$  are shown for 3 passes on 16, 17, and 18 August.  $G_{\perp}$  and  $\phi_G$  (dashed lines) are also shown. The solid lines are theoretical values of  $B_{\perp}$  and  $\phi$  at the instantaneous position of the spacecraft obtained by vector addition of the geomagnetic field and the disturbance field due to the circular current. The current loop is specified by  $R_0$ , the distance of the

loop from the center of the earth, and  $I$ , the total current. The numerical values of  $R_0$  and  $I$  give the best fit to the data based on a qualitative comparison. Note the similarity between  $R_0$  and  $I$  and the corresponding best fit parameters obtained previously for Explorer VI and Pioneer V data during non-storm intervals. The physical significance of the current loop is discussed in the text.

Figures 21-a and 21-b. Comparison Between the Akasofu, Cain, and Chapman Ring Current and the Explorer VI Storm Data.

Figure 21-a shows the Explorer VI data for the transverse field component,  $B_1$ , between 30,000 and 48,800 km on 16, 17 August. Figure 21-b shows the corresponding phase angle data.  $G_1$  and  $\phi_G$  are also plotted. Theoretical values of  $B_1$  and  $\phi$  at specific geomagnetic latitudes were computed by transforming the disturbance field associated with a model ring current (Akasofu, Cain, and Chapman, 1961) into the satellite frame of reference. The two values of  $n_0 E$ , the kinetic energy density of the trapped plasma at the peak in the radial distribution function, are 50 and 150 kev  $\text{cm}^{-3}$ .

## REFERENCES

1. Akasofu, S. I. On a Self-Consistent Calculation of the Ring Current Field, J. Geophys. Res. 67, 3617 (1962)
2. Akasofu, S. I., and S. Chapman, The Ring Current, Geomagnetic Disturbance and the Van Allen Radiation Belts, J. Geophys. Res. 66, 1321, (1961)
3. Akasofu, S. I., J. C. Cain, S. Chapman, The Magnetic Field of a Model Radiation Belt, Numerically Computed, J. Geophys. Res. 66, 4013 (1961)
4. Akasofu, S. I., J. C. Cain, and S. Chapman, The Magnetic Field of the Quiet Time Proton Belt, J. Geophys. Res. 67, 2645 (1962)
5. Alfvén, H., Theory of Magnetic Storms, Kungl. Sv. Vet- Akademiens Handl. 18, (1940)
6. Alfvén, H., Cosmical Electrodynamics, Clarendon Press, Oxford (1950)
7. Apel, J. R., S. F. Singer, and R. C. Wentworth, Effects of Trapped Particles on the Geomagnetic Field, Advances in Geophysics vol IX (Ed. H. F. Landsberg) Academic press, New York (1962)
8. Arnoldy, R. L., R. A. Hoffman, and J. R. Winckler, Observations of the Van Allen Radiation During August and September 1959, Part I. J. Geophys. Res. 65, 1361 (1960)
9. Axford, W. I., and C. O. Hines, Unifying Theory of High Latitude Geophysical Phenomena and Magnetic Storms, Canad. J. Physics, 39, 1433 (1961)
10. Bader, M., Preliminary Results of the Low Energy Proton Analyzer, Explorer XII Symposium (Goddard Space Flight Center, January 1962)
11. Beard, D. B., Self Consistent Calculation of the Ring Current, J. Geophys. Res. 67, 3615 (1962)
12. Bridge, H. S., C. Dilworth, A. J. Lazarus, E. F. Lyon, B. Rossi, and F. Scherb, Direct Observations of the Interplanetary Plasma, Proc. of International Conference on Cosmic Rays and the Earth Storm, J. Phys. Soc. Japan 17, 553 (1962)

13. Chapman, S., and J. Bartels, Geomagnetism, Volumes 1 and 2, Oxford University Press, New York (1949)
14. Chernosky, E. J., Changes in the Geomagnetic Field Associated with Magnetic Disturbance, Proc. Int. Conf. Cosmic Rays and Earth Storm J. Phys. Soc. Japan 17, 25 (1962)
15. Coleman, P. J., C. P. Sonett, D. L. Judge, and E. J. Smith, Some Preliminary Results of the Pioneer V Magnetometer Experiment, J. Geophys. Res. 65, 1856 (1960)
16. Coleman, P. J., C. P. Sonett, and L. Davis, On the Interplanetary Magnetic Storm: Pioneer V, J. Geophys. Res. 66, 2043 (1961)
17. Davis, L. R., and J. M. Williamson, Trapped Protons and Electrons Between Two and Twelve Earth Radii, Explorer XII Symposium (Goddard Space Flight Center, January 1962)
18. Dessler, A. J., and E. N. Parker, Hydromagnetic Theory of Geomagnetic Storms, J. Geophys. Res., 64, 2239 (1959)
19. Dessler, A. J., and R. Karplus, Some Effects of Diamagnetic Ring Currents on Van Allen Radiation, J. Geophys. Res. 66, 2289 (1961)
20. Dungey, J. W., Interplanetary Magnetic Field and the Auroral Zone, Phys. Rev. Letters 6, 47 (1961)
21. Fan, E. Y., P. Meyer, and J. A. Simpson, Trapped and Cosmic Radiation Measurements from Explorer VI, Space Research, Ed. H. Kallman Bijl, North Holland Publishing Company Publishing Company, Amsterdam, p. 951 (1960).
22. Farley, T. A., and A. Rosen, Charged Particle Variations in the Outer Van Allen Zone During a Geomagnetic Storm, J. Geophys. Res. 65, 3494 (1960)
23. Gringauz, K. I., and S. M. Rytov, On the Relationship Between the Magnetic Field Measurements Obtained by U.S.A. Explorer VI and Pioneer V, and Those Obtained by Soviet Cosmic Rockets with Charged Particle Traps, DOKL, AN-SSSR 135, 48 (1960)

24. Gringauz, K. I., V. G. Kurt, V. I. Moroz, and I. S. Shklovskii, The Io Gas and Fast Electrons in the Vicinity of the Earth and in Interplanetary Space, *Astronomical Jnl.* (Academy of Sciences of USSR) 37, (1960)
25. Harrison, E. R., The Earth's Distant Magnetic Field, *Geophysical Jnl.* 6, 479 (1962)
26. Heppner, J. P., J. D. Stolarik, I. R. Sharpiro, and J. C. Cain, Project Vanguard Magnetic Field Instrumentation and Measurements, Space Research Proceedings of First International Space Science Symposium, Edited by H. Kallman BIJL (North-Holland Pub. Co., Amsterdam, 1960), p. 982
27. Heppner, J. P., N. F. Ness, T. L. Skillman, and C. S. Scearce, Magnetic Field Measurements with the Explorer X Satellite, Proceedings of International Conference on Cosmic Rays and the Earth Storm (Kyoto, Sept. 1961) *J. Phys. Soc. Japan* 17, 546 (1962)
28. Heppner, J. P., N. F. Ness, C. S. Scearce, and T. L. Skillman, Explorer X Magnetic Field Measurements, GSFC-NASA Report X-611-62-126 Submitted to the *J. Geophys. Res.* (1962)
29. Judge, D. L., A. R. Sims, and M. G. McLeod, The Pioneer I, Explorer VI, and Pioneer V High Sensitivity Transistorized Search Coil Magnetometer, *I. R. E. Trans. on Space Elect. and Telem. SET* 6, 114 (1960)
30. Krassovsky, V. I., Results of Scientific Investigations Made by Soviet Sputniks and Cosmic Rockets, *Astronaut. Acta*, 6, 32 (1960)
31. Lincoln, J. V., Geomagnetic and Solar Data, *J. Geophys. Res.* 65, 788
32. Piddington, J. H., The Transmission of Geomagnetic Disturbances to the Earth's Surface, *Geophys. J.*, 2 173 (1959)
33. Piddington, J. H., Geomagnetic Storm Theory, *J. Geophys. Res.* 65, 9
34. Piddington J. H., The Cis-Lunar Magnetic Field, *Planet. Space Sci.* 305, (1962)

35. Rosen, A., T. A. Farley, and C. P. Sonett, Soft Radiation Measurements on Explorer VI Earth Satellite, Space Research, Ed. by H. Kallman BIJL, North Holland Publishing Company, Amsterdam, (1960), p. 938
36. Rosen, A., and T. A. Farley, Characteristics of the Van Allen Radiation Zones as Measured by the Scintillation Counter on Explorer VI, J. Geophys. Res. 66, 2013 (1961)
37. Schmidt, A., Abh. der Kgl. Pr. Met. Inst. 5, 37 (1916), also Encyclopedia der Math. Wiss. 6, 334
38. Singer, S. F., A New Model of Magnetic Storms and Aurorae, Trans. Am. Geophys. Union 38, 175 (1957)
39. Singer, S. F., Nature of Magnetic Storm Belt Particles: Electrons or Protons? (Abstract) J. Geophys. Res. 67, 1658 (1962)
40. Smith, E. J., P. J. Coleman, D. L. Judge, and C. P. Sonett, Characteristics of the Extraterrestrial Current System: Explorer VI and Pioneer V, J. Geophys. Res., 65, 1858 (1960)
41. Smith, E. J., and D. L. Judge, Transient Variations in the Extraterrestrial Magnetic Field (Abstract), J. Geophys. Res. 66, 2562 (1961)
42. Smith, E. J., and C. P. Sonett, Satellite Observations of the Distant Field During Magnetic Storms: Explorer VI, Proceedings of International Conference on Cosmic Rays and the Earth Storm (Kyoto, Sept. 1961) J. Phys. Soc. Japan 17, 17 (1962)
43. Smith, E. J., A Comparison of Explorer VI and Explorer X Magnetometer Data, J. Geophys. Res. 67, 2045 (1962)

44. Smith, E. J., Theoretical and Experimental Aspects of Ring Currents, in Space Science (Ed. D. P. LeGalley) Wiley and Sons New York (1963)
45. Sonett, C. P., D. L. Judge, and J. M. Kelso, Evidence Concerning Instabilities in the Distant Geomagnetic Field: Pioneer I, J. Geophys. Res. 64, 941 (1959)
46. Sonett, C. P., D. L. Judge, A. R. Sims, and J. M. Kelso, A Radial Rocket Survey of the Distant Geomagnetic Field, J. Geophys. Res., 65 55 (1960)
47. Sonett, C. P., E. J. Smith, and A. R. Sims, Surveys of the Distant Geomagnetic Field: Pioneer I and Explorer VI, Space Research, Proceedings of First International Space Science Symposium, Edited by H. Kallman BIJL (North-Holland Pub. Co., Amsterdam, 1960), p. 921
48. Sonett, C. P., E. J. Smith, D. L. Judge, P. J. Coleman, Current Systems in the Vestigial Geomagnetic Field: Explorer VI, Phys. Rev. Letters, 4, 161 (1960)
49. Vestine, E. H., Lines of Force of the Geomagnetic Field in Space, Planet. and Space Science 1, 285 (1959)

CHAPTER III

PIONEER V DATA REDUCTION AND ANALYSIS

by

Eugene W. Greenstadt



## I. INTRODUCTION

Most of the results of this year's investigation of the Pioneer V record have been discussed in the first and second Quarterly Progress Reports previously submitted under this contract (References 1, 2, and 3). For convenience, the findings are enumerated in Section IV of this chapter.

During the latter half of the year and particularly during the final quarter, attention has been directed to the existence of a relative change in the low or undisturbed interplanetary field level which appears to have occurred during the two month data acquisition period. In the course of preparing a compilation of the low level Pioneer V data for this study, several disagreements were found between the raw data listed on computer printout and the plotted and tabulated readings, presumably taken from that printout, which have heretofore served as basic material for all the published reports on Pioneer V results. It was therefore decided to re-examine the raw data carefully with the aim of producing a recount of the Pioneer V magnetometer record where necessary.

As of the writing of this report, neither task, recount of the raw data nor analysis of the undisturbed field has been completed. Sections II and III will review the present status of these activities.

## II. DATA RECOUNT

The original reduction of Pioneer V raw data was performed during and shortly after the flight itself, under the pressure of diverse conflicting commitments and in the atmosphere of forced urgency that still permeated the space program in mid-1960. It is not surprising, therefore,

that occasional discrepancies are to be discovered in this lengthy accumulation of data whose reduction would be demanding under the most unhurried circumstances. Although great change in the overall record is not expected to result from the contemplated recount of data points, a reliable analysis of such relatively subtle effects as a low-level variation require production of a concise reference compilation faithful in detail to the raw listings.

About 70 percent of the data has been checked or recounted at the time of writing. Most of the existing figures have remained unaltered, but in a few cases early in the record, major revision of tabulated values has been required. Table I shows two of the more extreme examples of transmissions in which the recount is substantially different from the previous result. In the table, "Transmission Numbers" refers to the sequential order of each payload on-time, and "Mid-range Field Value" refers to the center of the range of magnetic flux densities represented by each digital reading, when evaluated in an assumed temperature of 50°F.

It has already been proposed that compilation of the Pioneer V magnetometer data be funded (reference 4) and we plan to complete the recount for inclusion in a proposed Pioneer V compendium. Spot check comparisons between revised data averages and the original versions indicate that drastic alteration of the previous data pattern does not occur and that, in particular, the apparent variation in low-level field, whose investigation motivated the recount, will still be in evidence.

TABLE I

Samples of Revised Pioneer V Data Count

Date	Trans- mission Number	Digital Reading	Mid-Range Field Values ( $\gamma$ )		Number of Readings		Average Field Value ( $\gamma$ ) All Readings	
			Previous	Revised	Previous	Revised	Previous	Revised
15 Mar.	27	28	13.25	13.25	1	1		
		27	8.0	8.6	61	77		
		25	3.88	3.88	53	998		
		24	2.70	2.60	1	2		
		23	2.35	2.39	2	2		
		21	2.04	2.04	1	1	6.02	4.22
16 Mar.	32	27	8.0	8.6	117	674		
		25	3.88	3.88	65	140		
		24	2.70	2.70	2	2		
		23	2.39	2.39	1	1		
		21	2.04	2.04	2	2	6.42	7.75

### III. LOW LEVEL FIELD STUDY

Preliminary evidence from the magnetometer of space probe Pioneer V showed a tendency for the measured field component, in the absence of transient disturbances, to remain at a rather constant field value of around 2.7 gamma (Reference 5). Subsequent examination of the data in greater detail, however, has indicated the presence of a slow variation during the recording period, which may be due to solar influence.

The possibility of a systematic quiet, or low-level field variation was first suggested by a characteristic of the plot of smoothed satellite data used in demonstrating a correlation between payload measurements and geomagnetic disturbances. The curve referred to (Figure 1a) consists of a series of undulations whose maxima occur in conjunction with both geomagnetic storms and elevations of the smoothed planetary magnetic index (Reference 6). If maxima of the interplanetary curve represent disturbed periods then it seems reasonable that minima should correspond to undisturbed intervals. On this assumption, then, the history of the minimal values, shown in Figure 1b, suggest that a gradual modulation of the quiet field may have been present. Figure 1c is an alternate representation of the evidence, showing a history of the minimal values of another plot (not shown) of the field corresponding to the average of the two most common digital readings each day.

To assess the validity of this result, a variety of possible representations of the "quiet", or "undisturbed", readings have been examined.

Since high readings seem to be definitely associated with stormy intervals, field values low in absolute value form the basis for the chosen criteria of disturbance-free conditions.

The most straightforward approach to a definition of quiet periods is to select intervals during which no storm was reported and for which the interplanetary field remained at low values. In this context, the points of Figure 1b and c represent relative minima in ambient field, occurring between periods of relatively higher field, the latter presumably corresponding to the presence of greater disturbance.

A second representation of the quiet field can be obtained by producing a history of all readings below some preselected field level, since the raw magnetometry data from Pioneer V was frequently characterized by interspersions of low readings during storms and of relatively high values during otherwise normal intervals. Since magnitudes above five to seven gamma seemed to be associated with disturbances, values at or below these figures can be used as criteria for dividing disturbed from undisturbed data. In Figure 2a, for example, are plotted the (smoothed) daily averages of all mid-range readings of  $3.88\gamma$  or below. It is seen that this curve retains the sharp minima of 23 March and 20 April, seen in the previous figure, but at the same time shows much additional detail impossible in the previous representation.

A third technique can be imagined for selecting undisturbed readings. Points occurring in those periods during which the measured field remained essentially constant, with little or no fluctuations or with

peak to peak fluctuation confined to some predetermined limit, can be averaged. Unfortunately, this approach is unfruitful because of a difficulty inherent in the instrument calibration. All data were recorded as digital numbers, each number representing a range of magnetic field values. The range corresponding to each number increases greatly with higher numbers and with higher fields, so that the only situations in which the data can be tested unambiguously for absence of large fluctuation are those in which the ranges and hence the field levels themselves are small. Consequently, the application of this criterion produces a result which is essentially a duplication of the relative minima of Figure 1, and therefore has not been reproduced separately here.

The fourth and last criterion of field quietude considered is related to the probability of detecting random or irregular changes in ambient field regardless of actual extreme values attained during any period of agitation. This measure consists of finding the ratio of the number of points above some preselected field level to the total number of points both above and below that level. Results of applying this criterion produce a curve similar to, but with sharper features than those of 2a.

Before placing faith in the evidence of ambient field change offered by Figures 1 and 2a, it must first be asked whether the observed effects could have been instrumental in origin. If the presence of some unknown and undefinable electronic caprice is omitted from discussion, there are basically two possible sources of the kind of gradual variation recorded: temperature change within the spacecraft and a modification of payload spin frequency during the data period.

An examination of the magnetometry data themselves offers reason at once to doubt any extensive influence of either factor. If the apparent tendency of recorded field values to drop to low levels around March 22 and April 20, with higher readings before and after each of these dips, is to be accepted, then it seems highly unlikely that the temperature would suffer just this kind of variation and almost inconceivable that the payload spin frequency would manifest such behavior, with its implication of no less than two mid-course increases in spin rate!

Examination of actual data from each of the temperature sensors carried by the vehicle bears out the inference that this factor was not influential. Not only is the shape of each temperature curve unlike that of the magnetometry graphs, but the temperature exhibited a gradual inclination to increase during flight. According to the magnetometer calibration, the latter effect would have produced a similar overall rise in field readings (for assumed constant ambient field), which is exactly contrary to experience. We feel this factor can therefore be neglected.

The influence of a change in spin frequency is not quite so easily disposed of by reference to direct measurement because no record similar to that of temperature exists, and the necessary re-runs of magnetic tapes to attempt an estimate of spin rate from the antenna pattern variation in signal strength have not yet been carried out. The above indirect reasoning excluding reversals in spin rate trend, however, seems to

exclude any possibility of an effect on the data that would tend to produce the pattern with which we are presently concerned. It is tentatively concluded, therefore, that the apparent slow fluctuation in low field level, with two dominant minima around 22-23 March and 20 April, was a real feature of the measured ambient field component during the Pioneer V flight.

If the apparent changes in the component of resident interplanetary field measured by Pioneer V cannot be unambiguously credited to internal behavior of spacecraft instrumentation, then it seems reasonable to ask whether the observed variation can be imputed to the state of the payload environment. Confirmation of the payload curves and some clue to the implications can therefore be sought in other concurrent measures of interplanetary conditions. Other direct measurement of the extra-solar ambium are of course not available, but it seems reasonable to investigate simultaneous data on solar and terrestrial activity, especially in view of the 28 day interval separating the two predominant dips in measured field magnitude.

The general lack of correlation between low-importance solar activity and disturbed geomagnetic conditions has been repeatedly noted in the literature (Reference 7), so that in this case attention has been directed first to various criteria of solar conditions themselves. Since this study is still in an incomplete, if not preliminary stage, extensive comparisons are not available for this report. Figure 2, however, offers evidence that this approach will eventually be fruitful. Figure 2a



has already been described, while 2c and d repeat curves b and c of Figure 1, respectively. Figure 2b is a representation of coronal green line intensity projected to central meridian for the period in question (Reference 8). The coronal index was chosen in this case because its slowly changing nature lends itself easily to comparison with the rather crude versions of payload magnetic data in 2c and d, and because the only other readily available indices of gross solar activity, i.e. sunspot numbers and 10 cm emission, exhibit patterns quite different from the satellite curves.

The delay between sun and satellite can be seen by noting the displacement between the horizontal (time) coordinates of 2b and the remaining curves. This "best fit" delay of around 8.5 days corresponds to a sun-spacecraft "velocity" of approximately 200 Km/sec, not utterly inconsistent with a generally accepted quiet solar wind of 200-300 Km/sec (Reference 9). Whether such an assumption of physical connection between coronal streamer intensity and ambient field as is implied by the terms "delay" and "velocity" is justified remains to be determined. It is equally possible that the magnetic variations are in reality correlated with solar features bearing some regular relationship to green line enhancement, but not occurring at the sub-streamer heliographic longitude. Such displaced or anticorrelations are known to exist in the case of M-region storms, for example.

At present the best approach points toward an effort to find a similarity between some of the more detailed characteristics of the

low level data as represented in, say, Figure 2a or its equivalent, and some finer measure of solar activity than coronal index, e.g. plage area.

#### IV. SUMMARY OF THIS YEAR'S PIONEER V RESULTS

1. Pioneer V data taken during Polar Cap Absorption events showed no apparent connection between payload and PCA disturbances, thus obviating the likelihood of ambiguity in the correlation of payload-terrestrial magnetic storms, and tentatively excluding the existence of gross magnetic field effects associated with traveling PCA particles.
2. Investigation of Pioneer V telemetry sampling parameters indicated that major characteristics of the magnetometry record are independent of telemetry on-time and of digital bit-rate.
3. Relatively sharp, individual magnetic disturbances in the interplanetary region are caused by specific chromospheric flares.
4. Minimal flare size for a significant magnetic disturbance (five to seven gamma or more) was 3 to 5 square degrees at the 1960 level of the sunspot cycle, and with an importance designation 1+.
5. Average flare disturbance travel time from the sun to a distance of 1 A.U. is around 40 to 50 hours, with mean propagation velocities from individual flare sources to the satellite of 750 to 1150 Km/sec.
6. Interplanetary magnetic disturbances are associated with the type of plasma cloud to which geomagnetic storms are ascribed, but unless of considerable duration, do not necessarily correspond to geomagnetic events.

7. Interplanetary disturbances generally have a duration one half day or less, implying radial dimension of approximately 0.5 A.U.
8. Separation of "disturbed" from "quiet" field readings in the Pioneer V data suggests the existence of trends in each not as evident in the comprehensive averages where all data points are included. Disturbed values correlate well with high velocity flare and magnetic storm activity, while low level readings show a possible solar rotation periodicity, suggesting a connection with underlying solar conditions, possibly at great delay between sun and satellite.

V. REFERENCES

1. Quarterly Progress Report, "Reduction and Analysis of Explorer VI and Pioneer V Data", Contract NAS w-270, November 13, 1961.
2. Second Quarterly Progress Report, "Reduction and Analysis of Explorer VI and Pioneer V Data", Contract NAS w-270, February 20, 1962.
3. Third Quarterly Progress Report, "Reduction and Analysis of Explorer VI and Pioneer V Data", Contract NAS w-270, May 15, 1962.
4. "Continuation of Reduction and Analysis of Explorer VI and Pioneer V Data Volume I: Technical Plan", Proposal 0609.03, Contract NAS w-270, 19 October 1962. Prepared for submittal to NASA.
5. Coleman, P. J., Jr., L. Davis, Jr., and C. P. Sonett, "On the Steady Component of the Interplanetary Magnetic Field: Pioneer V", Phys. Rev. Letters, 5, 43-46 (1960)

6. Greenstadt, E. W., "Magnetic Storms in Interplanetary Space as Observed by Pioneer V", *Nature*, 191, 329-331 (1961)
7. Hansen, Richard T., Constance S. Warwick, and Marion B. Wood, "Studies in Solar Geomagnetic Relations I. Optical Criteria", NBS Report 5570, National Bureau of Standards, Boulder Laboratories, Boulder (May 12, 1958)
8. Henderson, De Arliss, "Integrated Indices of the Solar Corona 1960", Report No. HAO-57, High Altitude Observatory National Center for Atmospheric Research (15 June 1962)
9. de Jager, C., "Emission of Gas from the Sun", paper presented at COSPAR, Washington, D.C. (May 1962)

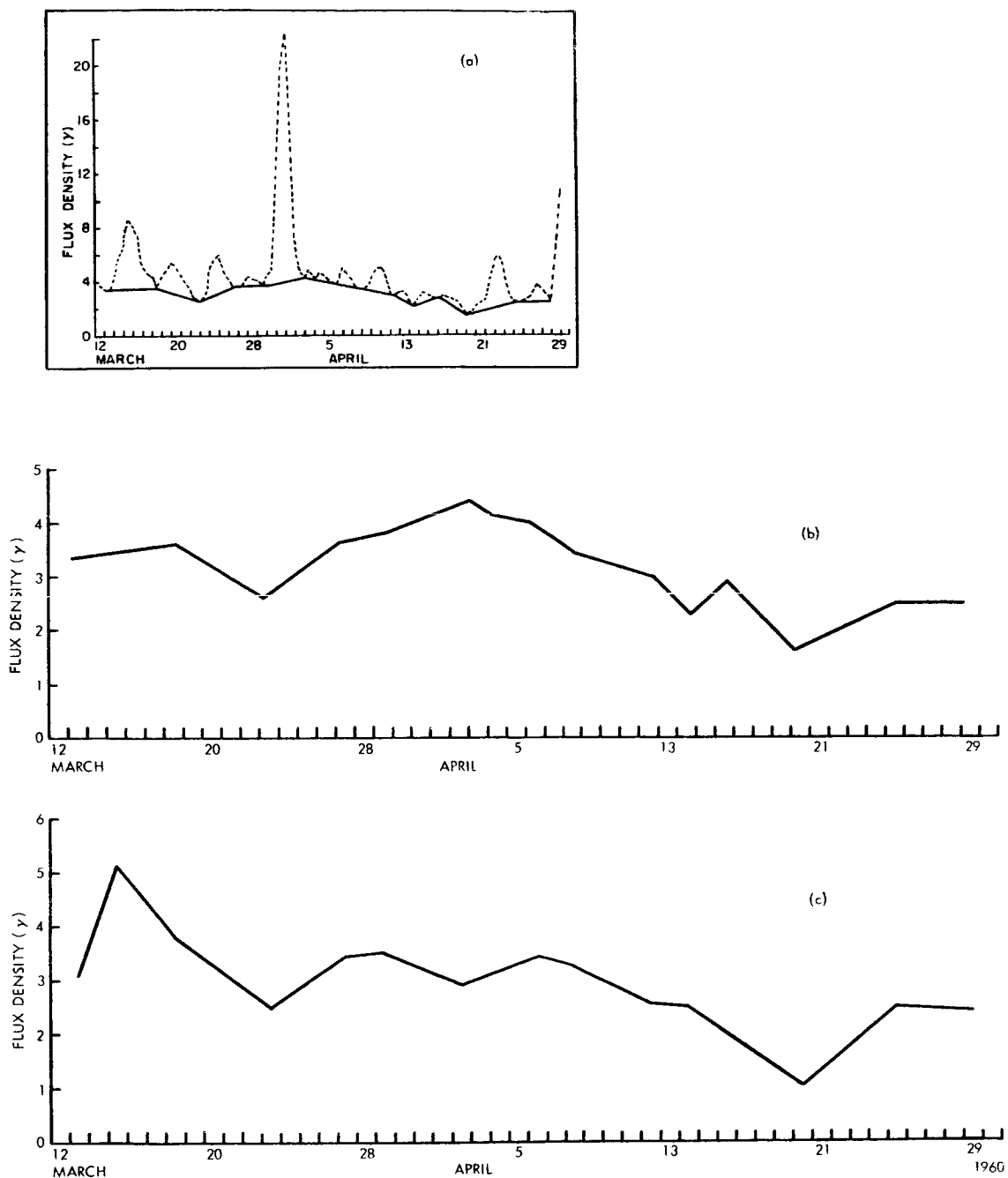


Figure 1. Variation in low level magnetic field measured by Pioneer V;  
 a) Smoothed average field at payload (dashed curve) showing lower envelope;  
 b) Expanded vertical scale plot of lower envelope;  
 c) Lower envelope of daily mean of two most frequent mid-range field values.

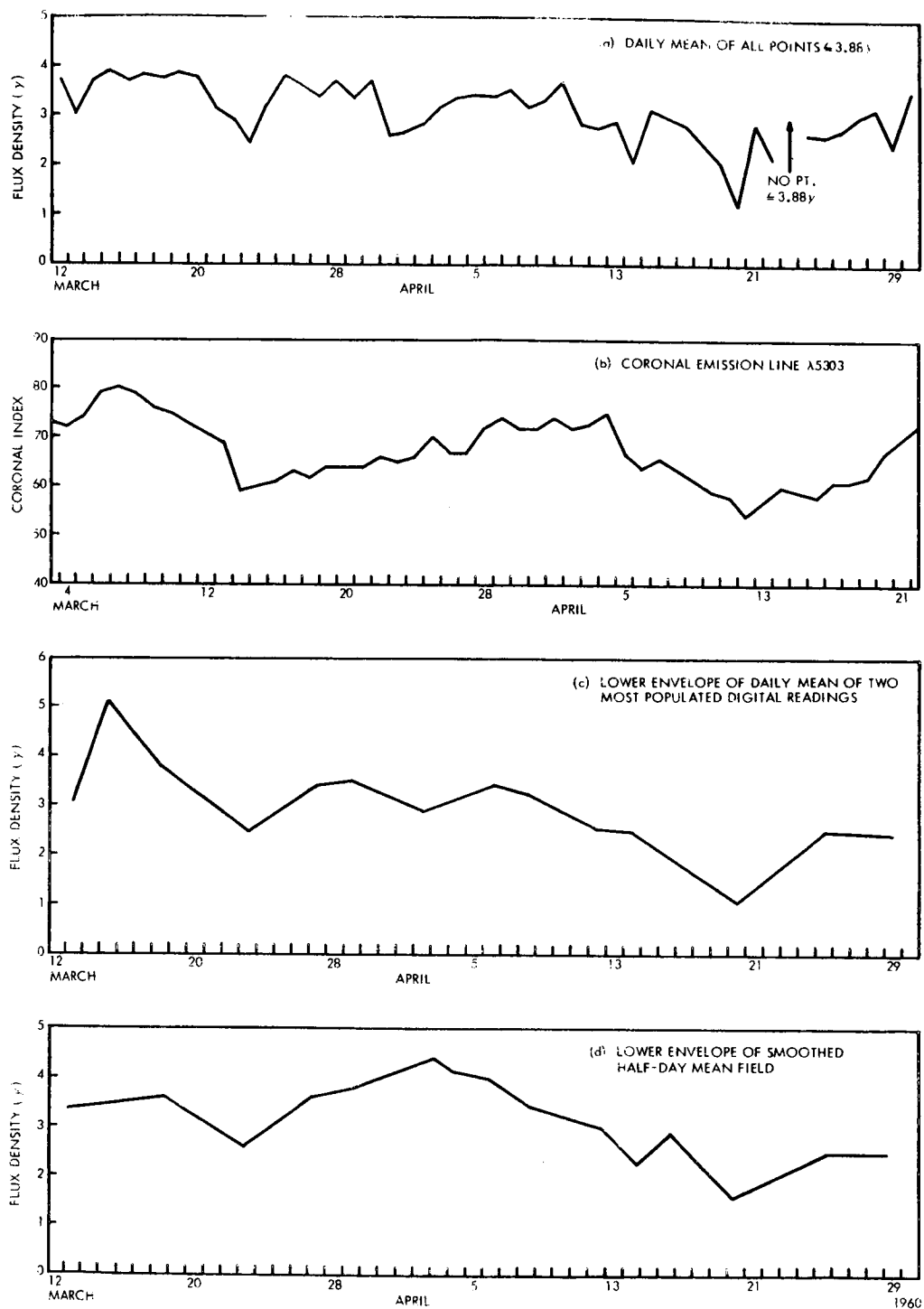


Figure 2. Comparison of low level field at Pioneer V with coronal index; a) Daily mean of all mid-range readings  $\leq 3.88\gamma$ ; b) Corona' green line index; c) Same as Figure 1(c); d) Same as Figure 1(b).

## CHAPTER IV

### AN INVESTIGATION OF SIGNAL FADING IN EXPLORER VI AND PIONEER V TRANSMISSIONS

by

R. C. Gore

## I. INTRODUCTION

The Explorer VI satellite, designated internationally as 1959  $\delta_1$ , was successfully launched August 7, 1959, into an orbit of period 768 min. with a perigee height of 157 miles, an apogee height of 26,366 miles and an inclination of  $47^\circ$ . From time of launch until October 2, 1959, telemetry data was transmitted by the satellite upon command from ground tracking stations. Difficulties in the transmission of this telemetry data were often occasioned by extremely deep fading in the signal strength. Further investigation of these occurrences indicated that they occurred somewhat systematically in time and position, and hence a more thorough investigation was undertaken to clarify the nature of these signal strength fluctuations.

Telemetry signals from Explorer VI were transmitted on FM subcarriers by three transmitters in the satellite: two 80 milliwatt VHF transmitters broadcasting at 108.06 mc and 108.09 mc; one 5 watt UHF transmitter broadcasting at 378 mc. Figure 1 shows a record of the normal VHF signal strength. The UHF transmitter could only be utilized for short periods due to its large drain on the power supply; VHF transmission was essentially limited only by the visibility of the satellite from a ground station. Primarily three different ground stations located at Manchester, Hawaii and Singapore were used for communicating with the satellite. Due perhaps to its geographic location or to the times of observation the station at Manchester, England, reported no fading of the type under investigation, Hawaii and Singapore ground stations both reported deep signal strength fading.

The ground station at Hawaii was located at the southernmost point in the Hawaiian Islands at South Point on the island of Hawaii. From the station



**Figure 1. Normal signal strength recording without fading.**

location there was an unobstructed view of the ocean and horizon from about  $60^{\circ}$  east of north around to the south of  $300^{\circ}$  east of north. Volcanic mountains shielded the station from the nearest sizeable towns of Kailua and Hilo, each of which is about 70 miles from the station site, hence, there was very little man-made radio interference. The antenna used primarily at the Hawaii station was a 60 foot parabolic antenna mounted at the top of a 70 foot tower of steel and concrete. This antenna could be rotated through an azimuth of  $360^{\circ}$  and through  $95^{\circ}$  in elevation. At 108 mc the full  $\frac{1}{2}$  power angle of the antenna pattern was  $11.2^{\circ}$  and its first side lobe peak was  $19^{\circ}$  from the axis. The overall gain of the main lobe was 23.3 db with the gain of the first side lobe some 20 db lower. At 378 mc the antenna gain was 35 db with the first side lobe's gain approximately 20 db lower; the  $\frac{1}{2}$  power angle was  $3^{\circ}$  and the first side lobe was at  $5^{\circ}$ . In addition to the parabolic antenna, a square pattern of four helical-array axial-mode antennas was arranged centered on the parabolic antenna; each of the helical-array antennas consisted of an array of four helices. The array had a gain of 19 db over an isotropic antenna and a beamwidth of  $30^{\circ}$ . In addition a 100 foot high antenna calibration tower was located 1300 feet NW of the parabolic antenna and was used to calibrate all the receiving antennas. The Hawaii station had a complete dual receiving installation consisting of a pair of phase-lock receivers which could receive 108 or 378 mc signals, two Ampex tape recorders, two Sanborn galvanometer recorders and a double set of voltage-controlled oscillators.

This dual installation allowed simultaneous recordings of telemetry from two frequencies. The Sanborn recorders were Model 150 8-channel galvanometers capable of recording signals from d-c to about 50 cps at paper speeds from 0.2 to 100 mm/sec. The phase lock receivers were used to amplify and demodulate the telemetry information and were capable of locking onto signals of -155 dbm or better.

The Singapore station was located 5 miles north of the city and was equipped with a single helical-array antenna identical to the array antennas at Hawaii. The ground station instrumentation, as at Hawaii, included a phase-lock receiver, Ampex tape recorder and Sanborn chart recorder.

## II. DESCRIPTION OF FADING OCCURRENCES

The fading in the signal strength of the 108 mc transmitters was often, but not always, initiated by a low frequency nearly sinusoidal variation in the signal level with a period of about 10 - 30 seconds. Within several minutes these oscillations would deepen in amplitude, increase in frequency and lose their regularity until the signal level was behaving in an essentially random fashion with departures from the average signal level of as much as 15 db. Signal strength fading of the 378 mc signal, when observed, occurred simultaneously with the VHF fading. Qualitatively, the fading amplitude of the UHF signal was comparable to the VHF amplitude, but the frequency of fading of the UHF signal was considerably lower than the VHF signal so that in general the UHF signal level was smoother.

The Explorer VI satellite was designed partially as a test vehicle for various concepts of space communication and it was for this purpose of testing the transmission system that the signal strength was originally recorded. Initial investigations into the nature of the fading were undertaken primarily as an adjunct to the communication test philosophy; the possible value of the signal strength record as a source of ionospheric information was not fully considered until after the complete failure of the satellite transmitters. As a result the signal level was rather infrequently calibrated and, consequently, later quantitative analysis was rendered difficult. Additional complexity was introduced by the fact

that the calibrations which were made showed the scale to be nonlinear in amplitude and/or power and somewhat unstable between calibrations. As can be seen from Figure 2 an average calibration curve could be obtained with an uncertainty of approximately 3 db at the higher signal levels and 5 db at the lower signal levels, i.e., below - 140 dbm. This uncertainty was felt to be sufficiently small to at least permit semiquantitative data reduction. The resultant of these factors is a large amount of semiquantitative and qualitative data which was not primarily intended for ionospheric investigation but which nonetheless seemed possibly related to ionospheric phenomenon.

The UHF transmitter could only be utilized for limited periods, consequently, the majority of the data available relates only to VHF signal fading. The VHF fading characteristics will, therefore, be described first and then the relatively minor amount of UHF fading will be contrasted with it. Fading at VHF was frequently characterized at onset by an apparent low frequency oscillation in the signal strength envelope. The frequency of this initial fading might vary between 4 - 10 cycles/min; however, the amplitude would occasionally be comparable to that of later higher frequency fading rates. In this type of fading, the signal appears quite regular and the modulation of the signal strength due to the spin of the satellite is seldom obscured, see Figures 3a and 3b. This slower type of fading would persist for a period of time of between 2 - 15 minutes after which time the regularity

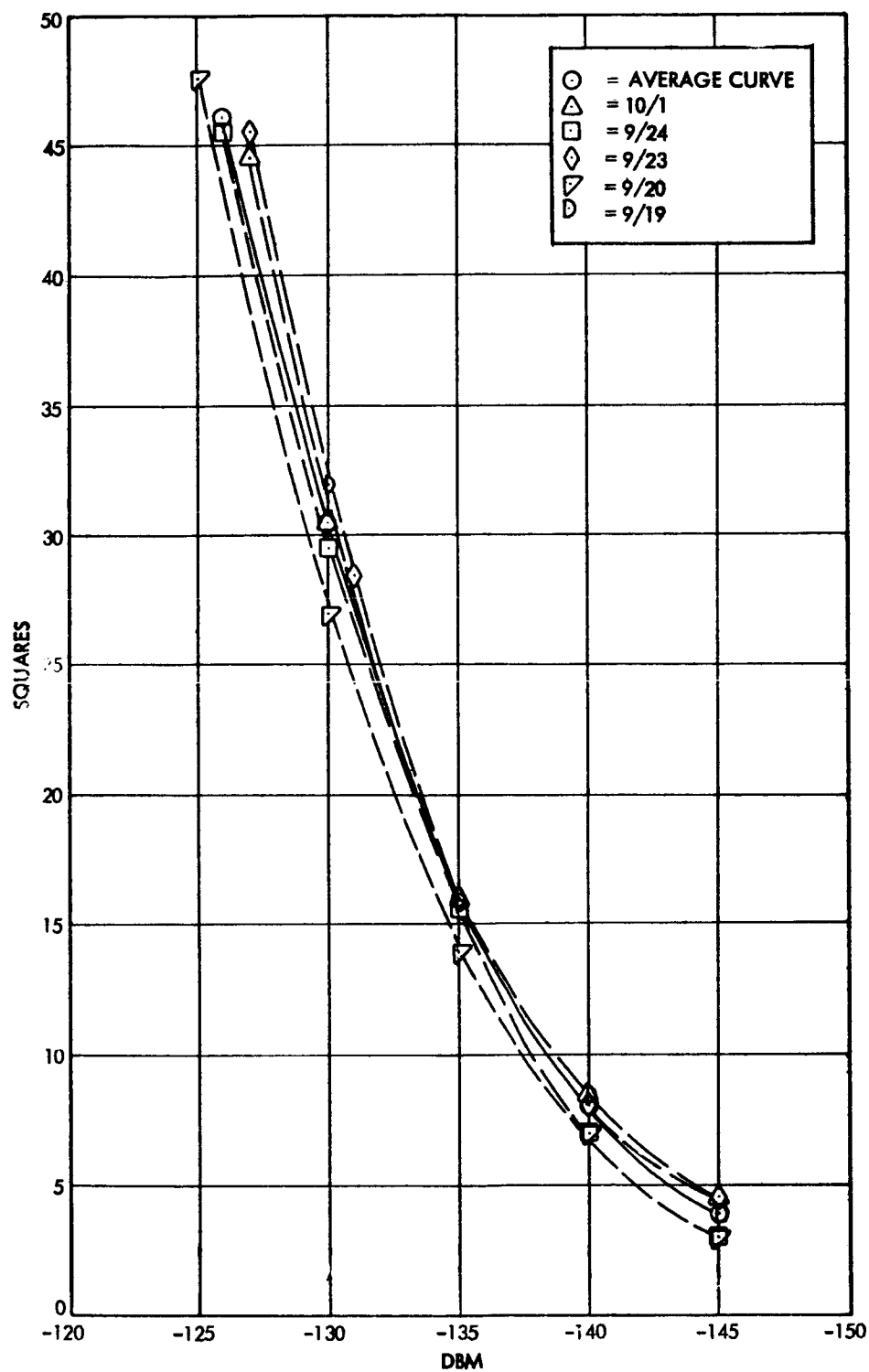


Figure 2. Sample of calibration curves made for one setting of gain control showing variation in time.

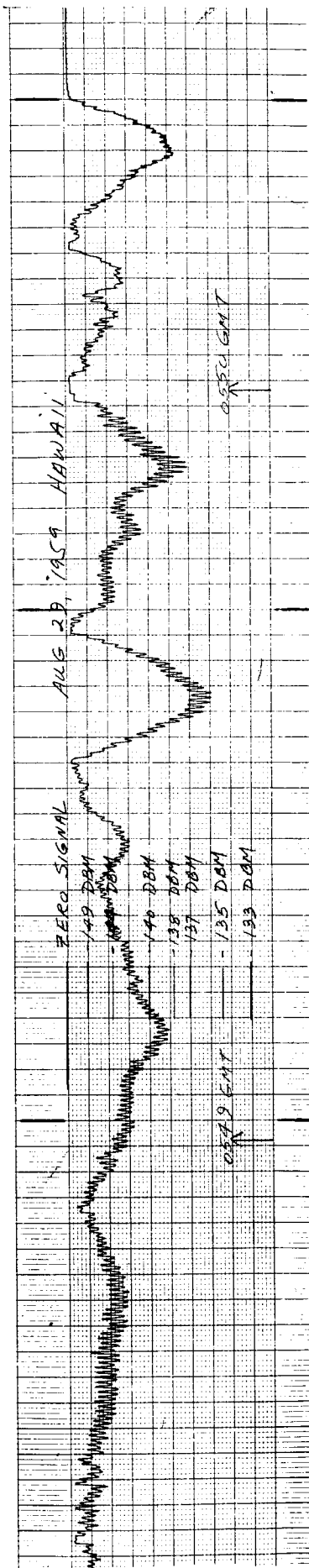


Figure 3a. Illustration of slow fading onset

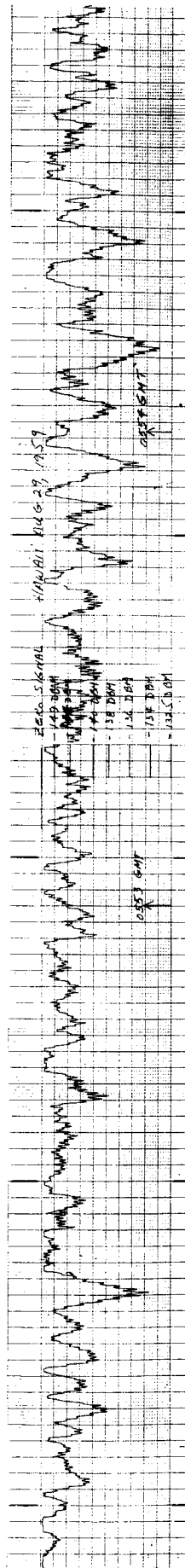


Figure 3b. Illustration of slow fading showing continuation of fading from the onset shown in 3a.



of the fading would be obscured by highly erratic, high frequency, large amplitude fluctuations in the signal strength which in some records seemed to be superimposed over the more regular preliminary fluctuations. Equally frequently, the fading would begin immediately to exhibit the high frequency, erratic behavior with little or no preliminary slower regular fading, see Figure 4. The high frequency fading would persist for long periods frequently to the end of the tracking period, see also VHF record in Figure 5. Interruptions in the fading during the tracking would occasionally be noted but persistence of the fading after onset to the end of tracking was more characteristic of this phenomenon. When the fading terminated while the satellite was still transmitting to the ground station, the slower regular type of fading was often noted after the high frequency fading terminated. The maximum amplitude of the high frequency signal level fluctuation is estimated to be roughly 20 db; signal level fluctuations greater than 4 db were often characteristic of this fading. Fading rates observed during the higher rate fading varied from 10 cycles/min to approximately 50 cycles/min and occasionally reached the vicinity of 100 cycles/min with an average of approximately 30 cycles/min. No difference was noted in the character of the fading encountered at Singapore and Hawaii.

Although data on fading during UHF transmissions is somewhat limited, sufficient information is available to discern an essential

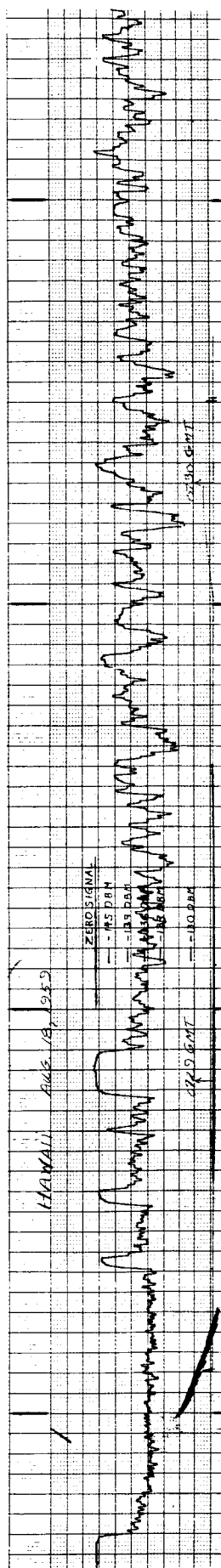


Figure 4. Illustration of onset of fast type of fading.

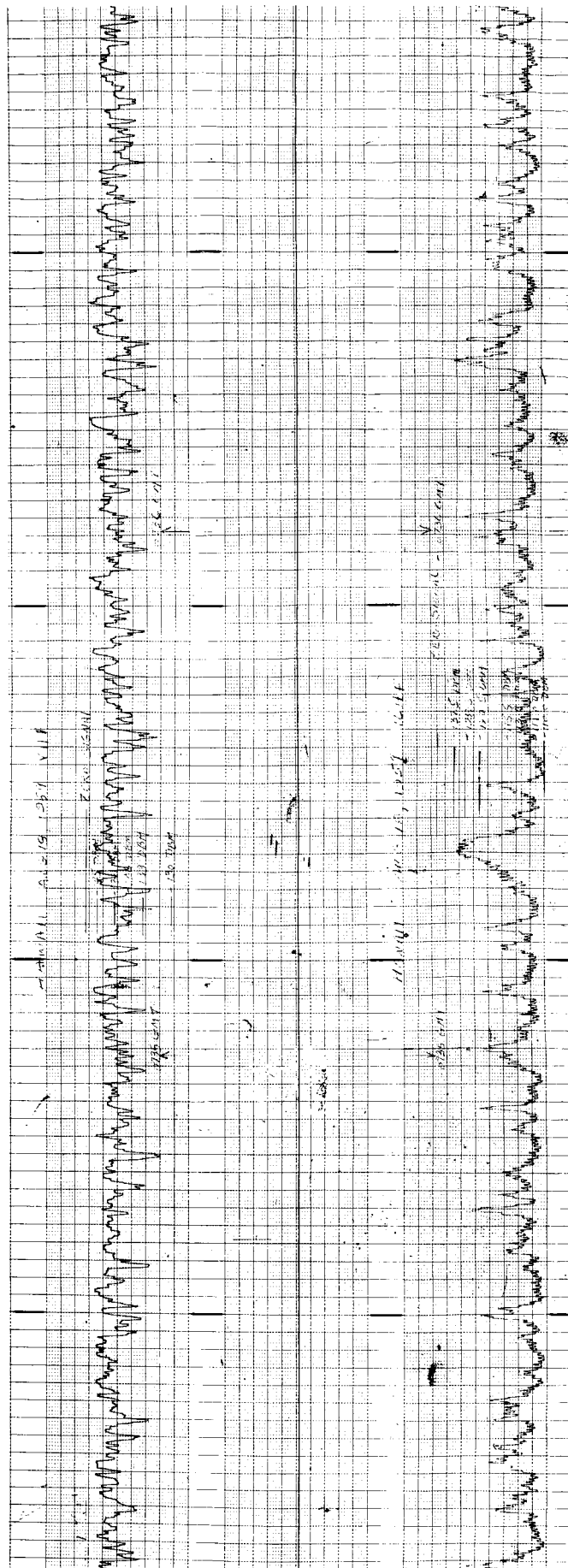


Figure 5. Comparison of simultaneous fast VHF fading and UHF fading.

difference in the nature of the fading at UHF to that at VHF. Occurrences of fading at UHF were only noted during periods of fading at VHF; however, a normal transmission at UHF was noted concurrently with severely fading signal levels at VHF. Concurrent transmissions at UHF and VHF were not sufficiently numerous to provide a clearer picture of the mutual occurrence of fading at the two frequencies. A summary of representative samples studied of concurrent transmissions is given in Table 1, which shows rather clearly the comparative character of the two types of fading: UHF fading measured in amplitude of the total fluctuation in db is comparable to the total fluctuation of the VHF; however, the UHF shows a significantly more regular and lower rate of fading than the VHF fading, see Figure 5. UHF transmissions at Singapore were made during quiet periods on the VHF and the available data showed no fading at UHF at Singapore.

As a check against possible malfunction of the transmitters on the satellite causing the fading, the records were examined for periods during which transmissions were simultaneously received at Singapore and Hawaii. On several of these records fading was found to have occurred at one of the two stations; however, no fading was found to occur simultaneously at both stations. Therefore, the conclusion follows that transmitter malfunction cannot account for the fading observed.

At the time when the fading was first encountered while tracking 1959  $\delta_1$  at Hawaii, unexpectedly severe Faraday rotation was hypothesized as the cause. In an attempt to alleviate the fading, reception was transferred from the parabolic antenna, which was in principal use, to

TABLE 1  
COMPARISON OF VHF AND UHF FADING CHARACTERISTICS AT HAWAII

Time (GMT)	VHF			August 15, 1959			
	Maximum peak to peak ampli- tude (DB)	Freq. Fad'g (cycles/min)	Average Signal Level (DBM)	Time (GMT)	Maximum peak to peak ampli- tude (DB)	Freq. Fad'g (cycles/min)	Average Signal Level (DBM)
1148 ↓ 1149	16	28 - 30	-141	1148 ↓ 1149	10	10 - 12	-109
1120 ↓ 1121	19	26 - 30	-144	1120 ↓ 1121	10	8	-109
1054 ↓ 1055	19	18 - 22	-145	1054 ↓ 1055	12.5	7 - 10	-109
August 18, 1959							
0733 ↓ 0734	19	40	-139	0733 ↓ 0734	26.5	25	-114
0957 ↓ 0958	19	43	-143	0957 ↓ 0958	24	34	-113
1020 ↓ 1021	22	31	-145	1020 ↓ 1021	4.5	9	-112
1033 ↓ 1034	16	43	-147	1033 ↓ 1034	27.5	28	-114
August 19, 1959							
0900 ↓ 0901	14	18 - 20	-141	0900 ↓ 0901	16	5 - 7	-134
0924 ↓ 0925	9	10 - 15	-141	0924 ↓ 0925	5.5	8 - 10	-132
0943 ↓ 0944	10	25 - 35	-141	0943 ↓ 0944	22	15 - 20	-134

the helical axial-mode antenna arrays which could receive the signal in either right- or left-circular polarization modes. No essential alleviation of the intensity of fading was attained by using antennas receiving circularly polarized signals instead of antennas with preferred planes of polarization. The fading was, therefore, not attributed to Faraday rotation although anomalies in the rate of Faraday rotation were observed, but not recorded, by tracking personnel.

Four days, when fading was known to occur, were chosen for more intense study: August 15, 19, 30 and September 3. For these days the data on fading at Hawaii was sampled evenly throughout the period of fading; generally samples were spaced roughly 6 minutes apart. At the times chosen, the fading rate was estimated by counting the number of peaks in the signal level fluctuations during one minute. The maximum amplitude of fading was estimated by measuring on the Sanborn chart the maximum departure from the average signal level; this fluctuation was normalized to provide what might be termed a fading index by dividing the maximum fluctuation by the distance on the Sanborn chart from the average signal level to the zero signal level. Even though the signal level is a non-linear function of distance on the Sanborn chart, if the assumption is made that the relationship between signal strength  $S$  and distance on the chart,  $D$ , is a simple power law  $S \propto D^n$ , then  $\frac{\Delta S}{S} = n \frac{\Delta D}{D}$ ; so that the fading index is a simple multiple of the normalized signal fluctuation. A value for "n" of  $n \sim 2$  was found to provide reasonably good conformity with the available calibration data.

The fading rate and fading index were plotted as functions of time of occurrences, see Figures 6 and 7. A maximum for both curves is found to occur roughly at 0830 GMT and no fading was found before 0600 GMT or after 1115 GMT on the days examined. The other data at Hawaii and Singapore supports the result that this fading is limited to the periods around sunset and early evening at the ground station (0600 GMT is 8:00 p.m. Hawaiian local time). Tracking data from the ground station provided the elevation angle above the horizon for the times sampled. From this data, Figures 8 and 9 were made by plotting the fading rate and index against the elevation angle. Except for a possible, weakly defined maximum in the vicinity of  $15^{\circ}$  above the horizon, no correlation seems evident.

The velocity at which the line-of-sight from the station to satellite proceeds through the ionosphere at 300 km above the earth was estimated by computing the geocentric angular rate of the point defined by the intersection of the line-of-sight with the 300 km elevation surface. The fading rate was determined for times at which the geocentric angular rate of the ray was computed for data from both Hawaii and Singapore; the resulting plot, Figure 10, shows no apparent correlation between the velocity of the ray through the ionosphere and the fading rate.

The general distribution of the fading was obtained by searching all the available records and noting the time and severity of the occurrences of fading. The elevation and azimuth angles obtained from the ground-station antenna steering data were plotted on polar scales so that an approximate representation of the celestial sphere over the

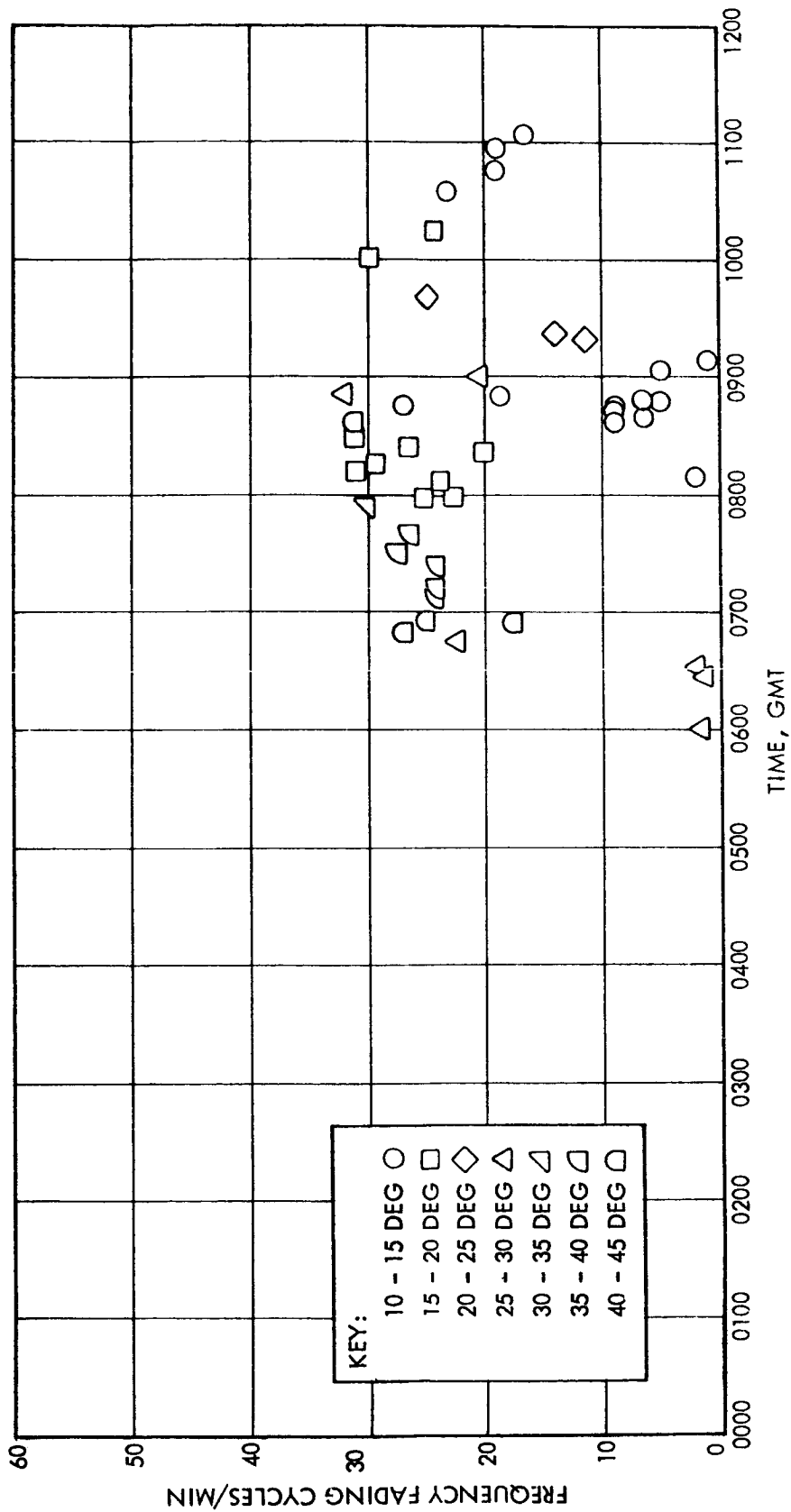


Figure 6. Fading frequency vs time of observation on selected days.



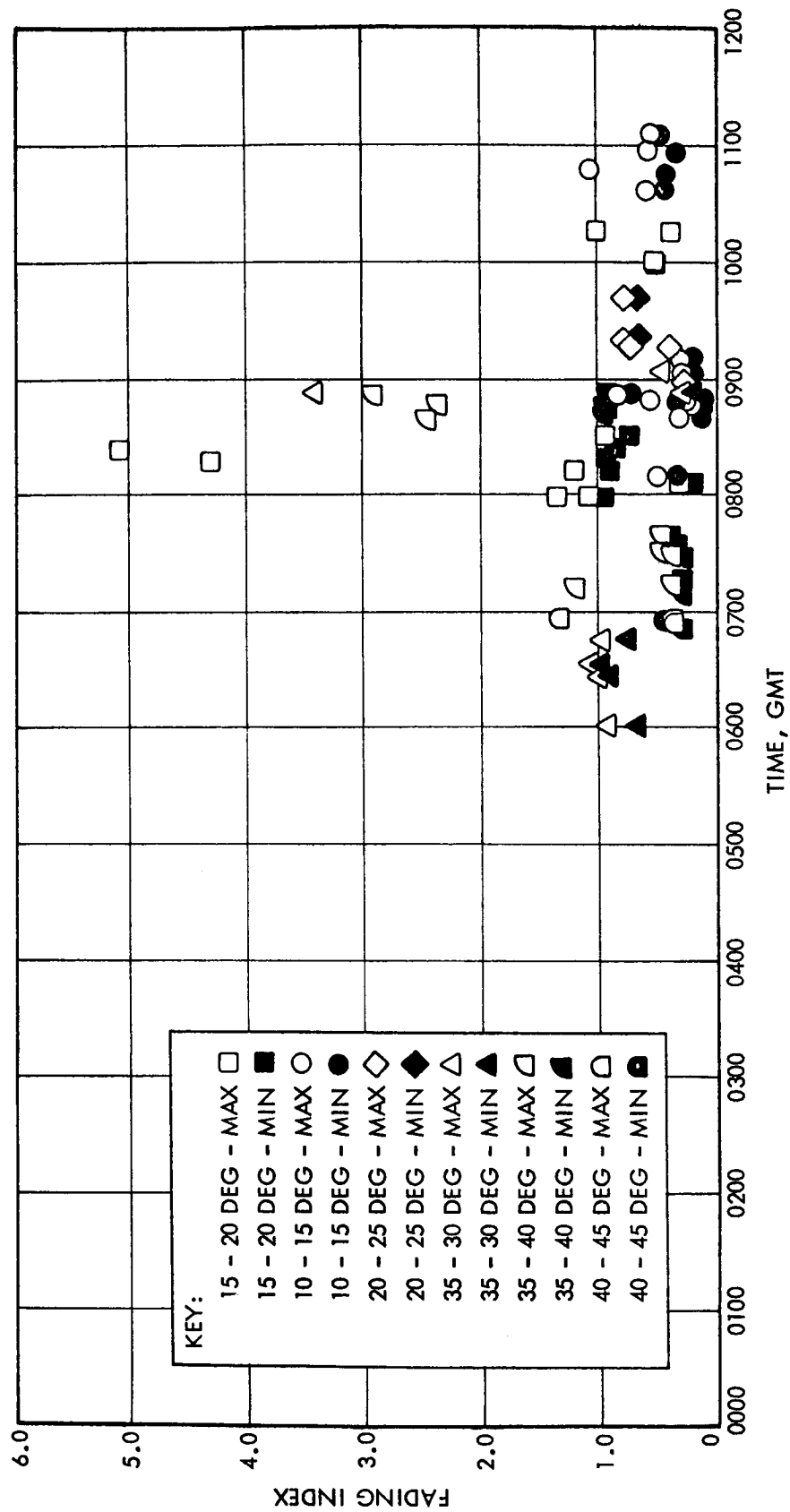


Figure 7. Fading index vs time of observation on selected days.

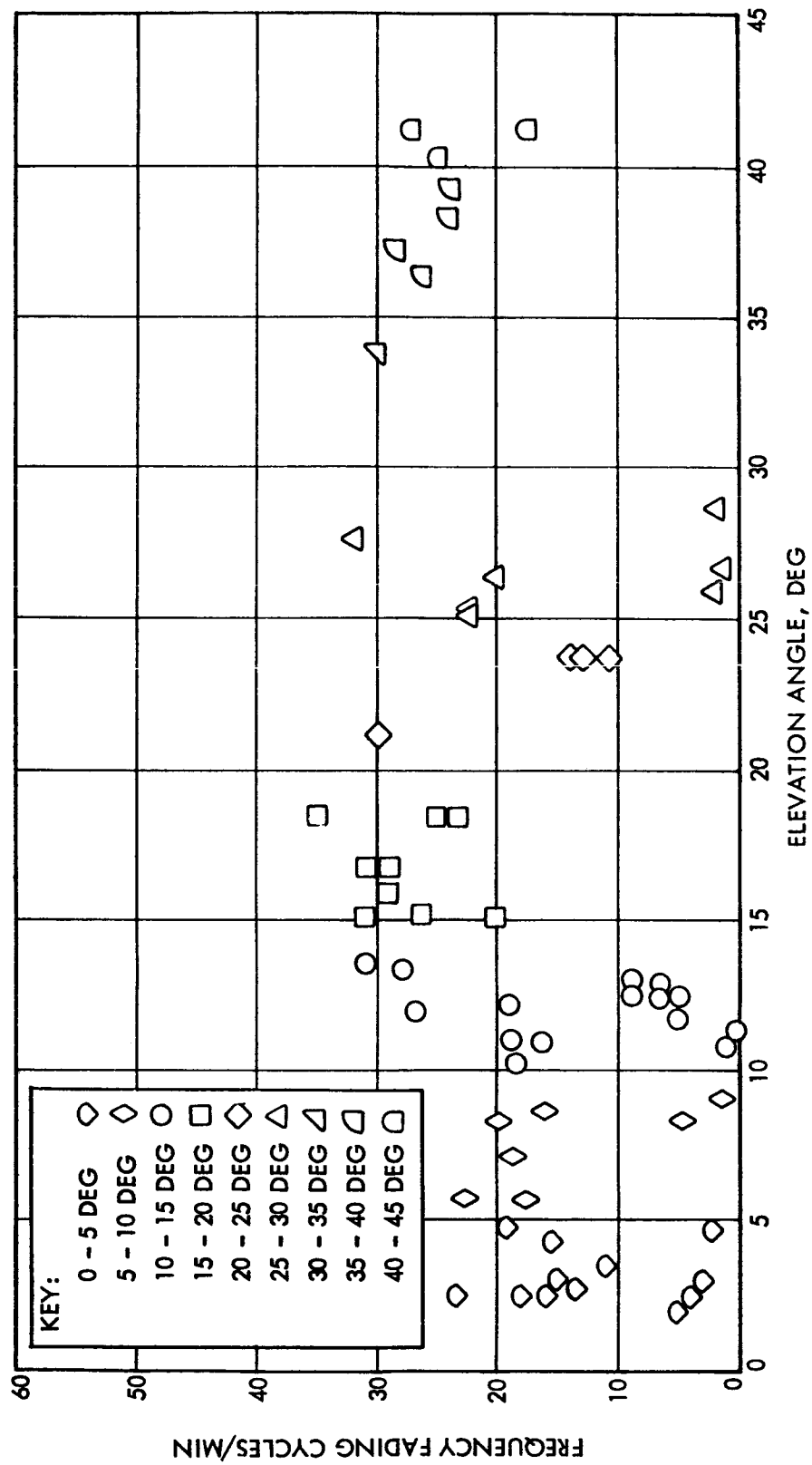


Figure 8. Fading frequency vs elevation angle at time of observation on selected days.

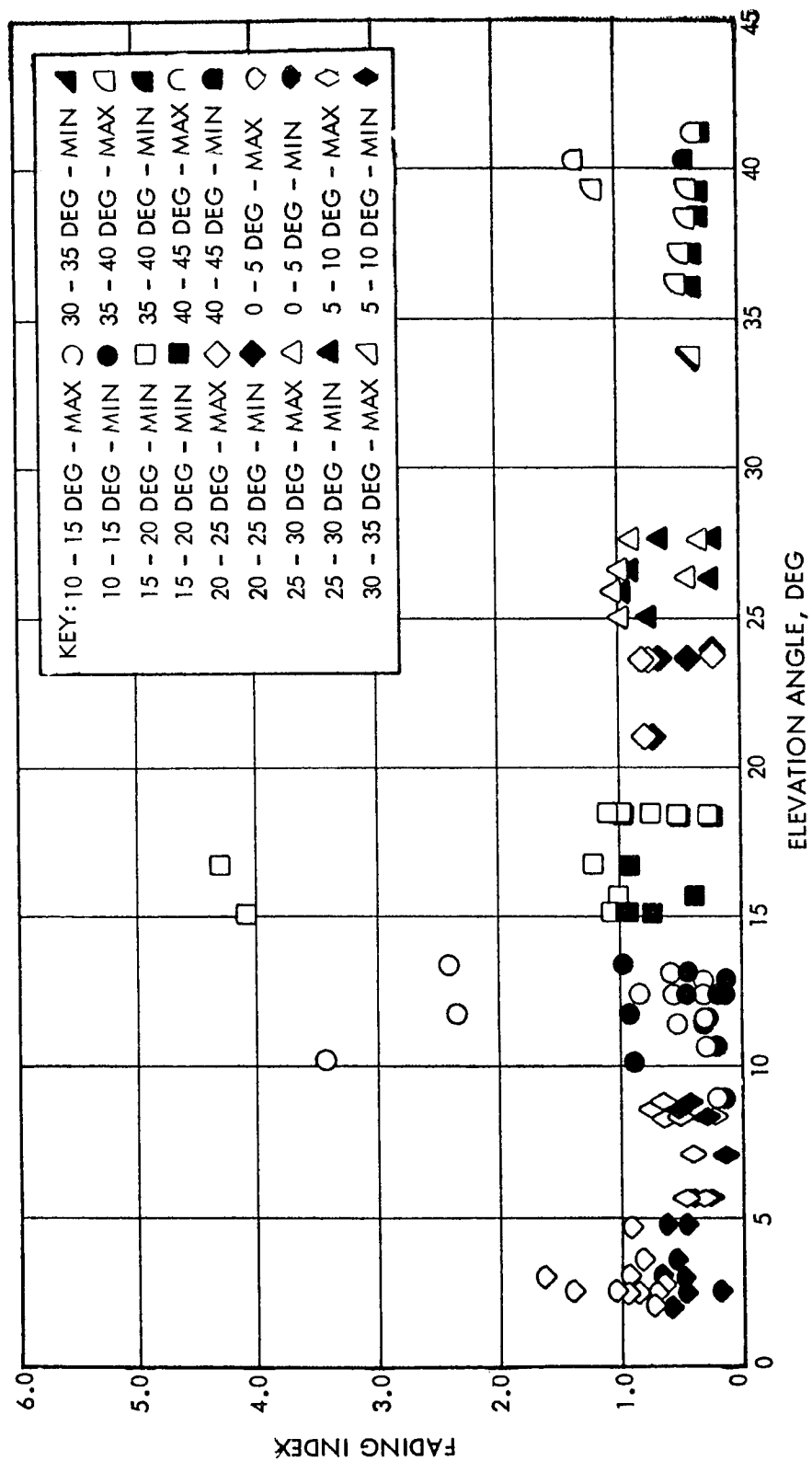


Figure 9. Fading index vs elevation angle at time of observation on selected days.

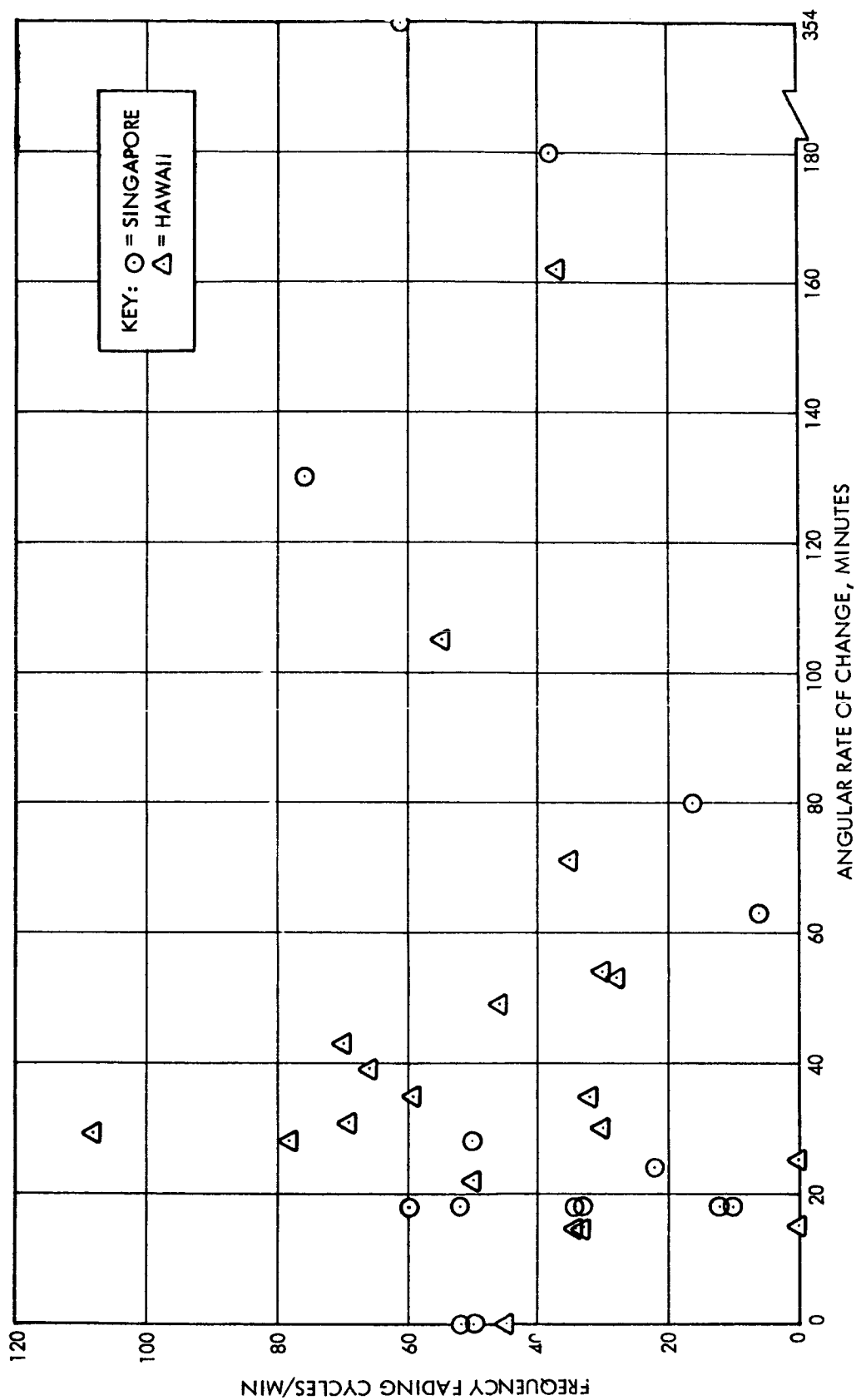


Figure 10. Fading frequency vs geocentric angular rate in minutes of arc/min. x 10.

tracking station is obtained. Periods of fading and no fading were noted on the elevation angle vs azimuth plots to produce Figures 11 and 12. The localization of occurrences of fading in particular regions of the celestial sphere is immediately apparent. The magnetic latitude of a point at a fixed height on the line-of-sight from a given ground station is just a function of the elevation angle and azimuth. Contours for the magnetic latitude of the line-of-sight at 300 km were computed from the relations given in the Appendix and plotted in Figures 11 and 12. The localization of fading occurrences in particular regions of the ionosphere between magnetic latitudes  $15^{\circ}$  and  $25^{\circ}$  is definitely suggested by the results presented for fading at both Hawaii and Singapore.

The associations of the fading with the early evening hours suggested the possibility of comparing the time of sunset in the ionosphere with the time of observation. Using the relations given in the Appendix, the time of sunset  $t_{ss}$ , at the 300 km elevation was computed for the line-of-sight from station to satellite at the time of fading onset for representative days at Hawaii and Singapore. The difference between the time of observation  $t_{obs}$ , and the sunset time is defined as  $\Delta t$ :  $\Delta t = t_{obs} - t_{ss}$ , this  $\Delta t$  was plotted versus the magnetic latitude of the line-of-sight at 300 km at time of onset; the result is given in Figure 13. The points which had a negative  $\Delta t$  represent very brief periods of fading which are similar in severity to other occurrences of fading, but of only 1 to 2 minutes in duration; these sporadic events occurred but rarely. All occurrences of long term fading, at

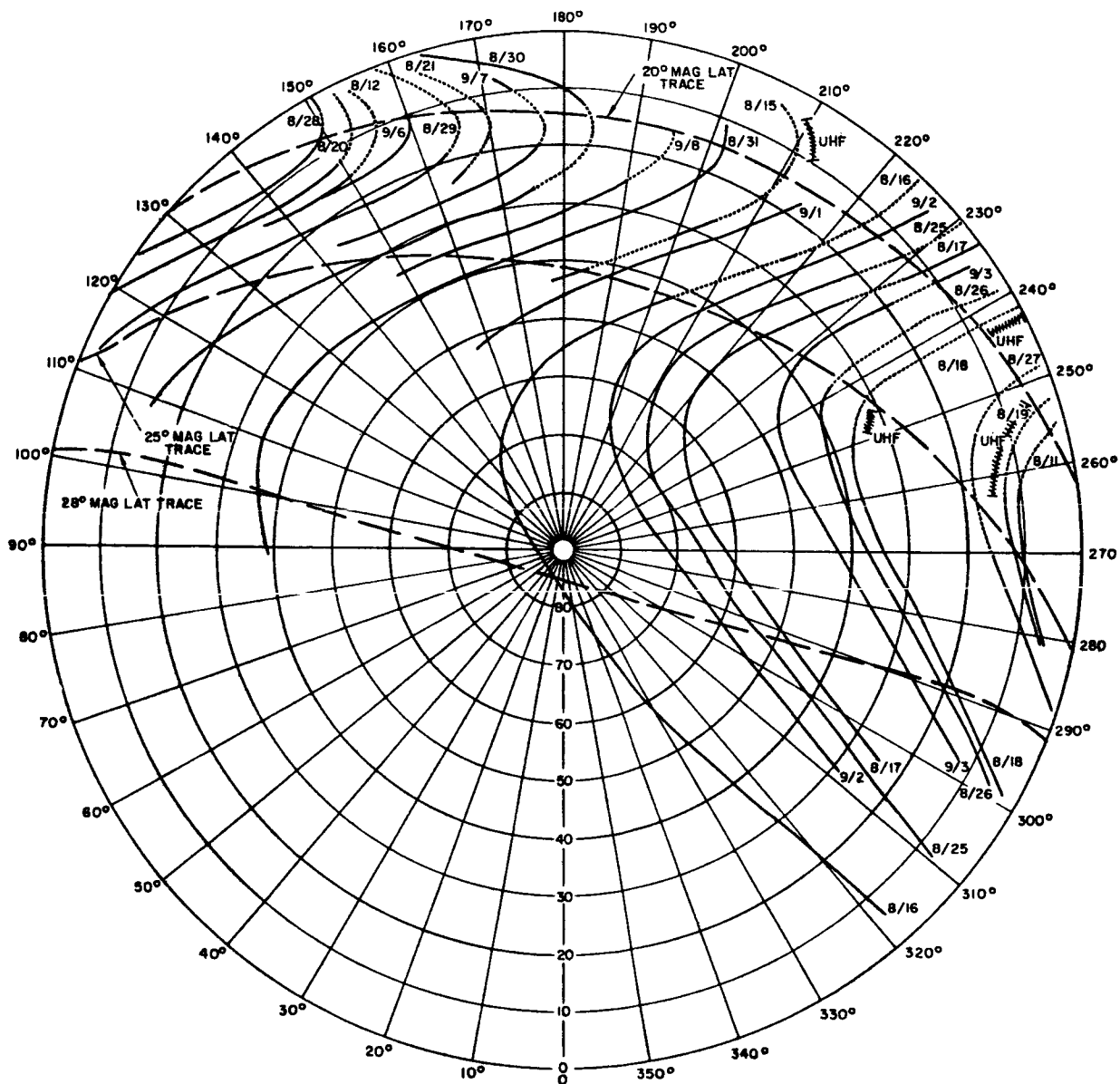


Figure 11. Tracking trace of Explorer VI on celestial sphere centered on Hawaii (dotted lines represent trace during VHF fading; cross-hatched lines adjacent to trace indicate sections of trace when UHF fading occurred.)

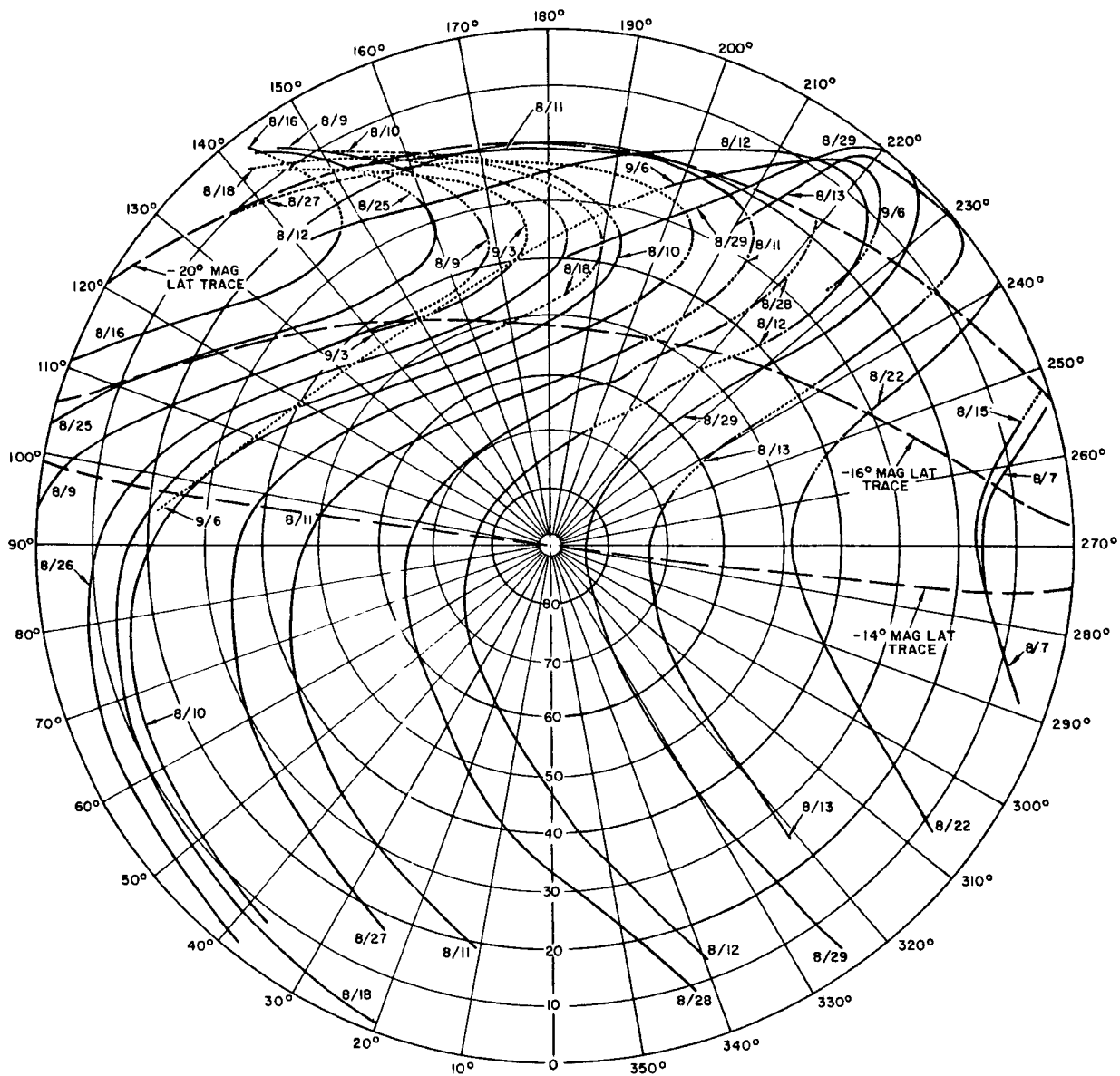


Figure 12. Tracking trace of Explorer VI on celestial sphere centered on Singapore (dotted lines represent trace during VHF fading; cross-hatched lines adjacent to trace indicate sections of trace when UHF fading occurred.)

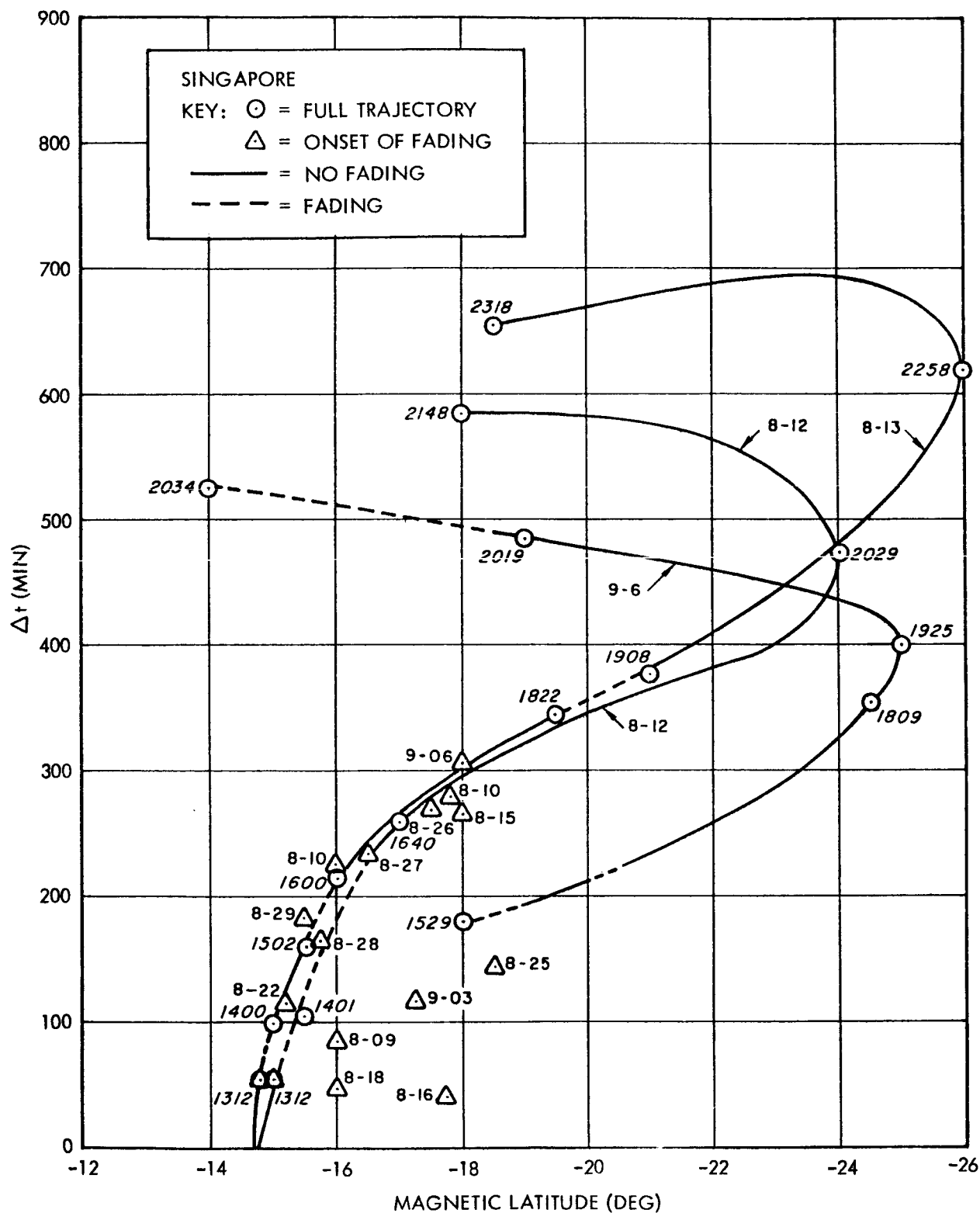


Figure 13.  $\Delta t$  vs magnetic latitude of onset of fading and sample traces observed at Singapore.



onset, had positive  $\Delta t$ 's. For several days, which exhibited intermittent fading.  $\Delta t$ 's and magnetic latitudes were computed for times during the tracking period after the onset. The resulting traces showing periods of fading were also plotted on Figure 13. The inference might be drawn that a suitable magnetic latitude and  $\Delta t$  are necessary but not sufficient conditions for the occurrence of fading.

### III. THEORETICAL CONSIDERATIONS REGARDING THE FADING

The results of the data analysis indicate that a possible mechanism for the generation of this fading might be scattering from inhomogeneities in the electron density distribution in the ionosphere. An alternative possibility might be multipath propagation, or ray bending. However, one would expect a correlation between velocity of the raypath through the medium and fading frequency for multipath propagation; a correlation which was found absent.

The question thus arises as to whether scattering of the electromagnetic signal might reasonably produce signal losses of the magnitude observed. Gordon (1953) has considered the scattering of radio waves by a turbulent medium. His results show that for media in which the scale length,  $\ell$ , of the turbulence is much greater than the wavelength of the signal, the beam angle of the scattered power is smaller than the ratio of wavelength to scale length: most of the scattered signal is scattered into a small forward angle. Using this result, the following simplified model might provide reasonably realistic results. Let a radio source radiate isotropically at frequency,  $f$ , at a large distance from a receiving antenna with large beam width through an isotropically turbulent medium whose dielectric constant's mean square fractional deviation is  $\left(\frac{\Delta E}{E}\right)^2$  and whose correlation function is assumed to be  $\rho(r) = e^{-\left(\frac{r}{\ell}\right)^2}$ . (There is no other a priori reason for assuming such a media than the convenience and the reasonableness of the assumptions, since no data seems available regarding the correlation function in the ionosphere. For this model, Gordon gives the power scattered per unit solid angle per unit incident power-density per unit volume,  $\sigma$ , as:

$$\sigma = \frac{\sqrt{\pi}}{8} \left( \frac{\Delta E}{E} \right)^2 \frac{1}{\lambda} \left( \frac{S}{\lambda} \right)^3 \sin^3 \chi e^{-\left( \frac{S}{\lambda} \sin \frac{\theta}{2} \right)^2}, \quad (1)$$

where  $S = 2\pi l$ ,  $\chi$  is the angle between the incident electric field vector and the scattering direction, and  $\theta$  is the angle between the incident direction of propagation and the scattering direction.

The power scattered out of the beam per unit volume can be obtained in a straightforward fashion from (1). Noting that for

$$\sigma = \frac{dI_s}{I_o V \Omega} : \quad (2)$$

where  $dI_s$  is the scattered power in the solid angle  $\Omega$ ;  $I_o$  is the incident power density on the volume  $V$ . Then for a spherical coordinate system  $(r, \theta, \phi)$  centered on the scattering volume:

$$\Omega = \sin \theta d\theta d\phi, \quad (3)$$

and

$$\sin^2 \chi = 1 - \sin^2 \theta \cos^2 \phi, \quad (4)$$

see Figure 14.

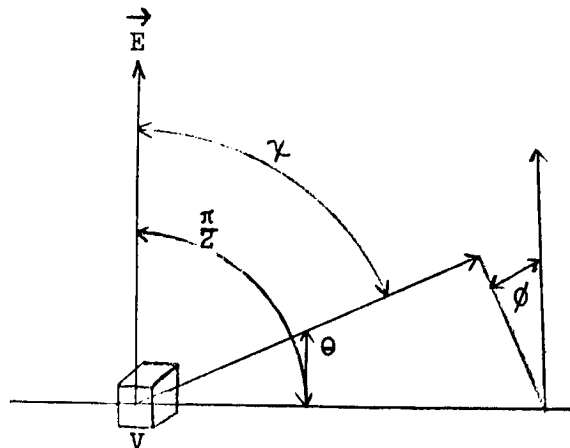


Figure 14. Scattering angles of model.

Substituting (2), (3) and (4) in (1), and utilizing  $\sin^2 \theta = \frac{1 - \cos \theta}{2}$

produces:

$$\frac{dI_s}{I_0 V} = \frac{\sqrt{\pi}}{8} \left( \frac{\Delta E}{E} \right)^2 \left( \frac{s}{\lambda} \right)^3 \frac{e}{\lambda} e^{-\frac{s^2}{2\lambda^2}} (1 - \sin^2 \theta \cos^2 \phi) \sin \theta \exp \left\{ \frac{s^2}{2\lambda^2} \cos \theta \right\} d\theta d\phi$$

For convenience let  $\gamma(\lambda) = \frac{\sqrt{\pi}}{8} \left( \frac{\Delta E}{E} \right)^2 \left( \frac{s}{\lambda} \right)^3 \frac{e}{\lambda} e^{-\frac{s^2}{2\lambda^2}}$ ; then we have,

$$\frac{dI_s(\theta, \phi)}{I_0 V} = \gamma(\lambda) (1 - \sin^2 \theta \cos^2 \phi) \sin \theta e^{\frac{1}{2} \left( \frac{s}{\lambda} \right)^2 \cos \theta} d\theta d\phi. \quad (5)$$

To find the total power, scattered out of the beam by volume V,  $I_s(0)$ ,

Eq. (5) is integrated for  $0 \leq \theta \leq \pi$ ,  $0 \leq \phi \leq 2\pi$  and performing the  $\phi$

integration immediately gives

$$\frac{I_s(0)}{I_0 V} = \gamma(\lambda) \pi \int_0^\pi (2 \sin \theta - \sin^2 \theta) e^{\frac{1}{2} \left( \frac{s}{\lambda} \right)^2 \cos \theta} d\theta. \quad (6)$$

Letting  $\cos \theta = x$ , Eq. (5) transforms easily to

$$\begin{aligned} \frac{I_s(0)}{I_0 V} &= \gamma(\lambda) \pi \int_0^1 (1 + x^2) e^{\frac{1}{2} \left( \frac{s}{\lambda} \right)^2 x} dx \\ &= \gamma(\lambda) \pi \left\{ \frac{2\lambda^2}{s^2} (e^{\frac{1}{2} \left( \frac{s}{\lambda} \right)^2} - 1) + \frac{8\lambda^6}{s^6} \left[ e^{\frac{1}{2} \left( \frac{s}{\lambda} \right)^2} \left( \frac{s^4}{4\lambda^4} - 2 \frac{s^2}{2\lambda^2} + 2 \right) - 2 \right] \right\}. \end{aligned} \quad (7)$$

For the case where  $\lambda \ll s$ , by neglecting terms of order  $\left( \frac{\lambda}{s} \right)^4$  and

higher, (7) becomes directly:

$$\frac{I_s(0)}{I_0 V} = \frac{\pi^{3/2}}{2} \left( \frac{\Delta E}{E} \right)^2 \frac{s}{\lambda^2}. \quad (7')$$

5.  $dr$

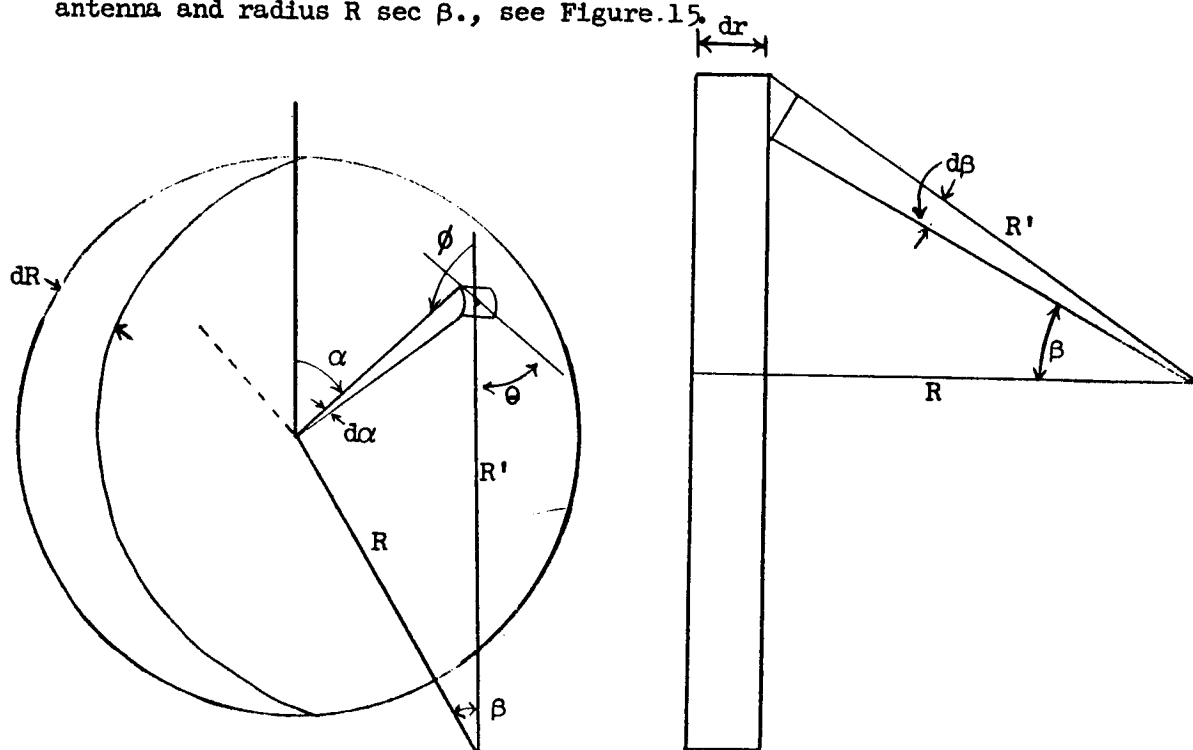


Figure 15. Scattering volume in ionosphere.

An increment of volume  $dV(\alpha, \beta)$  thus becomes

$$dV = R \tan \beta d\alpha R' d\beta \sec \beta dR = R^2 \frac{\tan \beta}{\cos^2 \beta} d\alpha d\beta dR$$

If the area of receiving antenna is  $a$ , then the solid angle subtended by the antenna from the increment of volume is  $\Omega' = \frac{a \cos^3 \beta}{R^2}$ .

The power scattered into the antenna by the increment of volume,  $dI_s^{(1)}$ , becomes

$$\frac{dI_s^{(1)}}{I_0} = dV \Omega' = R^2 \frac{\tan \beta}{\cos^2 \beta} d\alpha d\beta dR \frac{a \cos^3 \beta}{R^2} \sigma = a \sigma \sin \beta d\beta d\alpha dR .$$

Since  $\alpha = \phi$ ,  $\beta = \theta$ , Eq. (1) gives:

$$\frac{dI_s^{(1)}}{I_0} = a \gamma(\lambda) (1 - \sin^2 \beta \cos^2 \alpha) \sin \beta e^{\frac{1}{2} \left( \frac{s}{\lambda} \right)^2 \cos \beta} d\alpha d\beta dR . \quad (8)$$

Noting the similarity of (8) to (5) and (6), (9) follows easily:

$$\frac{dI_s^{(1)}}{I_0} = a \gamma(\lambda) \pi dR \int_0^B (2 \sin \beta - \sin^3 \beta) e^{\frac{1}{2} \left( \frac{s}{\lambda} \right)^2 \cos \beta} d\beta . \quad (9)$$

The integration follows immediately from (7); neglecting terms higher than  $\left( \frac{\lambda}{s} \right)^2$  and noting that  $e^{-\left( \frac{s}{\lambda} \right)^2 \sin^2 \frac{B}{2}} \sim 0$  unless  $B \sim \frac{\lambda}{s}$ , Eq. (9) becomes

$$\frac{dI_s^{(1)}}{I_0} = a \frac{\pi}{2} \frac{3}{2} \frac{s}{\lambda^2} \left( \frac{\Delta E}{E} \right)^2 dR . \quad (10)$$

For a thick inhomogeneous layer, multiple scattering effects must predominate, a fact which renders somewhat doubtful the previous results which implicitly assume single scattering. Correction for multiple scattering may be partially achieved by also considering the incident power upon a volume as that which has already been diminished by scattering in the media between the volume under consideration and the transmitter.

Thus, for the power scattered out of the beam,  $I_s^{(0)}$ , from  $\gamma'$ , we have:

$$I_s^{(0)} = \frac{\pi^{3/2}}{2} i_o(R) V \left( \frac{\overline{\Delta\epsilon}}{\epsilon} \right)^2 \frac{s}{\lambda^2}, \quad (11)$$

and for a small section of a nearly cylindrical beam of radius  $\rho$  and thickness  $dR$ :

$$i_o(R) = \frac{I_o(R)}{4\pi\rho^2}, \quad V = 4\pi\rho^2 dR.$$

So Eq. (11) becomes:

$$dI_s^{(0)}(R) = - I_o(R) \frac{\pi^{3/2}}{2} dR \left( \frac{\overline{\Delta\epsilon}}{\epsilon} \right)^2 \frac{s}{\lambda^2}, \quad (12)$$

and since

$$dI_s^{(0)}(R) = - dI_o(R), \quad \frac{dI_o(R)}{I_o(R)} = - \frac{\pi^{3/2}}{2} \left( \frac{\overline{\Delta\epsilon}}{\epsilon} \right)^2 \frac{s}{\lambda^2} dR. \quad (13)$$

Thus, if the intensity at  $R_o$  is  $I_o^*$  then

$$I_o(R) = I_o^* \exp \left\{ - \frac{\pi^{3/2}}{2} \left( \frac{\overline{\Delta\epsilon}}{\epsilon} \right)^2 \frac{s}{\lambda^2} (R_o - R) \right\}, \quad R_o \geq R \geq R_1; \quad (14)$$

$$I_o(R) = I_o^* \exp \left\{ - \frac{\pi^{3/2}}{2} \left( \frac{\overline{\Delta\epsilon}}{\epsilon} \right)^2 \frac{s}{\lambda^2} (R_o - R_1) \right\}$$

where  $R_o$  is the distance from the receiving antenna to the top of the scattering region and  $R_1$  is the distance to the bottom.

The signal scattered into the beam must also be subject to multiple scattering. Equation (10) should therefore be written:

$$dI_s^{(1)} = a \frac{\pi^{3/2}}{2} \frac{s}{\lambda^2} \left( \frac{\overline{\Delta\epsilon}}{\epsilon} \right)^2 i_o(R') dR'. \quad (10')$$

For the small range of  $\beta$  which contribute significantly to the scattered power the path length  $R'$  is very closely equal to  $R$  and so, noting that  $a_{I_0}(R_0) = I_0^*$ ,

$$a_{I_0}(R') = I_0^* \exp \left\{ - \left( \frac{\overline{\Delta\epsilon}}{\epsilon} \right)^2 \frac{s}{\lambda^2} (R_0 - R) \right\} \quad (15)$$

In addition, the power scattered into the beam will also be scattered out of the beam again so that for small  $\beta$ ,

$$dI_s^{(1)}(R) = \exp \left\{ - \left( \frac{\overline{\Delta\epsilon}}{\epsilon} \right)^2 \frac{s}{\lambda^2} (R - R_0) \right\} dI_s^{(1)}(R) \quad (16)$$

From (10'), (15) and (16), the power scattered into the antenna beam and received is

$$\begin{aligned} I_s^{(1)}(R_1) &= I_0^* \frac{\pi^{3/2}}{2} \frac{s}{\lambda^2} \left( \frac{\overline{\Delta\epsilon}}{\epsilon} \right)^2 e^{-\left( \frac{\overline{\Delta\epsilon}}{\epsilon} \right)^2 \frac{s}{\lambda^2} (R_0 - R_1)} \int_{R_1}^{R_0} dR \\ &= I_0^* \frac{\pi^{3/2}}{2} \frac{s}{\lambda} \left( \frac{\overline{\Delta\epsilon}}{\epsilon} \right)^2 \left( \frac{R_0 - R_1}{\lambda} \right) e^{-\left( \frac{\overline{\Delta\epsilon}}{\epsilon} \right)^2 \frac{s}{\lambda^2} (R_0 - R_1)} \end{aligned} \quad (17)$$

Let

$$\mu(\lambda) = \frac{\pi^{3/2}}{2} \frac{s}{\lambda} \left( \frac{\overline{\Delta\epsilon}}{\epsilon} \right)^2 \frac{1}{\lambda} \quad (18)$$

The power received at the antenna is the sum of the unscattered direct signal plus the scattered received signal; summing (14) and (17) gives:

$$\begin{aligned} I_{\text{rec}} &= I_0^* e^{-\mu(R_0 - R_1)} + I_0^* \mu(R_0 - R_1) e^{-\mu(R_0 - R_1)} \\ &= I_0^* e^{-\mu(\lambda)(R_0 - R_1)} \left[ 1 + \mu(\lambda)(R_0 - R_1) \right] \end{aligned} \quad (19)$$

To obtain numerical estimates  $\left( \frac{\overline{\Delta\epsilon}}{\epsilon} \right)^2$  must be estimated. For an isotropic medium with angular plasma frequency of  $\omega_p$ ,  $\epsilon = 1 - \left( \frac{\omega_p^2}{\omega^2} \right)$ ;



from which  $\epsilon \Delta \epsilon = -\frac{1}{\omega^2} \Delta \omega_p^2$  or  $\frac{\Delta \epsilon}{\epsilon} = -\frac{\Delta \omega_p^2}{2\omega^2 \epsilon} = -\frac{\Delta \omega_p^2}{\omega^2}$  for  $\frac{\omega_p^2}{\omega^2} \ll 1$ .

Now letting  $N$  = electron density and noting that  $N \propto \omega_p^2$  then letting  $\frac{\Delta N}{N} = P$ ,  $\Delta \omega_p^2 = \omega_p^2 P$  is obtained. Hence,  $(\frac{\Delta \epsilon}{\epsilon})^2 = (\frac{\omega_p}{\omega})^4 P^2$  with the assumption that  $\omega_p \ll \omega$  which for VHF propagation in the ionosphere is quite reasonable. From Eq. (18) then, letting  $f_p$  equal the plasma frequency,

$$\begin{aligned} \mu(\omega) &= \frac{\pi^{3/2}}{2} 2\pi \ell \left(\frac{\omega}{2\pi c}\right)^2 \left(\frac{\omega_p}{\omega}\right)^4 \frac{1}{P^2} = \sqrt{\pi} \ell \left(\frac{\omega_p}{c}\right)^2 \left(\frac{\omega_p}{\omega}\right)^2 \frac{1}{P^2} \\ \mu(f) &= \pi^{5/2} \ell \left(\frac{f_p}{c}\right)^2 \left(\frac{f_p}{f}\right)^2 \frac{1}{P^2} \end{aligned} \quad (23)$$

Leaving the justification to later, let  $\ell = 1 \text{ km}$ ,  $f_p = 15 \text{ mc}$ ,  $P = .01$  for the purpose of estimating  $\mu$ . If these numbers are substituted into (23),  $\mu(378 \text{ mc}) = 6.73 \times 10^{-3} \text{ km}^{-1}$ ,  $\mu(108 \text{ mc}) = 8.45 \times 10^{-2} \text{ km}^{-1}$ . Using  $R_0 - R_1 \approx 100 \text{ km}$ , as an example, from (19) the decibels of signal reduction at 108 mc is found to be  $D_{b108} = -26.9$ ; for 378 mc  $D_{b378} = -0.76$ .

By way of justifying the numerical values used, Wright (1960) shows that a region of the F layer, which conforms rather closely with the region in which fading was encountered in this study, in the early evening hours develops a high electron density corresponding to a plasma frequency of approximately 20 mc. This region of high electron density seems to extend rather far above the  $F_2$  layer peak, according to Wright, and the value of 100 km for  $R_0 - R_1$  does not seem to conflict with Wright's results. Several investigators, Ratcliffe (1960) among them, have estimated the scale length for irregularities in the F layer to be approximately 1 km or somewhat greater.  $P = .01$  represents a 1% variation in the electron density; although such a figure has been used by other

investigators, there seems to be little empirical justification for this value and hence this figure is used in this analysis purely by way of illustrating the effects of a small variation.

Although the rather primitive model suggested above seems to predict signal fluctuations of the correct order of magnitude, the question might be raised as to its applicability since no considerations of phase are included and hence the possibility of constructive and destructive interference is not included in the model. The following examination of the relative phase between the direct and scattered signal indicates that the phase difference is sufficiently small to be neglected in this model.

First note that in this model the scattered signal received at the antenna has only undergone signal scattering although certain multiple scattering effects have been included. Referring to Figure 16, where  $WW'$  is the plane wavefront,  $R$  is the distance the direct ray travels,  $R'$  is the distance the scattered wave travels, the scattering blob is approximated by the sphere of radius  $\frac{l}{2}$ , it is apparent that the phase

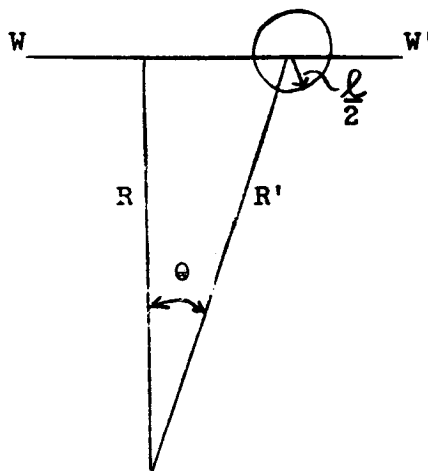


Figure 16. Scattering diagram for phase calculations.

of the scattered signal relative to the direct signal will be altered by two processes: 1) The signal propagates through a longer raypath, 2) The signal phase velocity is altered by propagating through the blob of different dielectric constant. For the case under consideration,  $\lambda \ll s$ , from the scattering cross section it is obvious that significant power is only scattered for  $\theta \leq \frac{2\lambda}{s}$ . Now  $R' \cos \theta = R$  and since  $\theta \ll 1$ ,  $R'(1 - \frac{\theta^2}{2}) \approx R$  or  $R' - R = \Delta R \approx R' \frac{\theta^2}{2} \approx R \frac{\theta^2}{2} \approx \frac{R}{2} (\frac{2\lambda}{s})^2$ . The change in phase  $\Delta\phi$  is  $\Delta\phi = \frac{\Delta R}{\lambda} \approx 2 \frac{R}{s} \frac{\lambda}{s}$ . At 108 mc,  $\lambda = 3\text{m}$  and using  $R \sim 600\text{ km}$ ,  $l \sim 1\text{ km}$ ,  $\Delta\phi \leq 0.1$ .

The phase change for the wave in passing through the blob is approximately

$$\Delta\phi = \frac{\omega}{c} \Delta n x \quad (24)$$

where  $x$  is the distance traveled through the blob and  $\Delta n$  is the average difference in the refractive index between the blob and the medium. For  $n^2 = 1 - \frac{\omega_p^2}{\omega^2}$ ,  $2n\Delta n = -\frac{\Delta\omega_p^2}{\omega^2}$ , therefore,

$$\Delta n = -\frac{1}{2} \frac{\omega_p^2}{\omega^2} \quad (25)$$

Putting (25) into (24) gives

$$\Delta\phi = -\frac{1}{2} \frac{\omega_p}{c} \frac{\omega_p}{\omega} P x \quad (26)$$

Equation (26) upon using  $l = 1\text{ km}$ ,  $f_p = 15\text{ mc}$ ,  $f = 108\text{ mc}$ , and  $P = 10^{-2}$  gives  $\Delta\phi = .03$ . The conclusion seems to present itself that for this model of the signal scattering process and other models similar to it that phase changes will contribute relatively insignificantly to signal strength fluctuations.

#### IV. PIONEER V SIGNAL FADING INVESTIGATION

As a continuation of the investigation of signal fading from the Explorer VI satellite, an investigation was undertaken of the signal strength records from the Pioneer V telemetry transmissions. A qualitative sampling was first taken of the available records and extremely rapid fluctuations were found to be prevalent throughout much of the tracking history and especially during the latter stages of the tracking. The rate of these oscillations was a great deal faster than was observed during the Explorer VI tracking; however, no calibration data was found in the first sampling so no judgment could be made regarding the amplitude of these fluctuations, and hence their nature.

A search was then conducted for signal strength calibrations in the Pioneer V data. The calibration data was found to be irregularly and sparsely distributed through the tracking records. The available calibrations made during the first month after launch were found, approximately 5 or 6 calibrations in all, and examined. Two conclusions were derived from an examination of these calibrations: 1) the calibrations did not remain even reasonably regular in time so that no valid generalized calibration could be obtained for use in analyzing the data accompanied by no calibrations; 2) calibration records at very low signal levels evinced the same behavior observed during regular transmissions, i.e., very rapid fluctuations, and consequently the conclusion was drawn that this rapid fluctuation was instrument

noise. This noise was not immediately identified as such due to the fact that the signal-to-noise ratio was much lower than experienced with the Explorer VI data and not until the calibration data was examined could it be obvious that the average signal level for the Pioneer V was considerably lower than the Explorer VI signal level.

The ground station crews at Manchester had occasionally reported fading in the signal during transmissions from Pioneer V. An examination was made of the signal strength records for the times mentioned by the ground crews. The equipment noise was sufficiently intense to obscure any other type of signal fluctuation on the signal strength recordings; however, the concurrent recordings of the automatic gain control, which behaves analogously to a smoothed signal strength recording, showed average signal level fluctuations of a minute or so in duration with the period of these fluctuations also about a minute. The magnitude of the signal strength reduction was with difficulty estimated to be on the order of 2 - 4 db. An attempt was made to find other occurrences of this type of fading in order to determine if it was a possible ionosphere phenomena. The attempt showed that the identification of this type of phenomenon was such a subjective activity due to the high noise level and small signal strength change that the validity of the results of such an investigation would be highly questionable. In addition, recorded occurrences of instrumental difficulty were found to resemble this "fading". Since nothing but data of questionable validity could be obtained, the investigation was terminated.

## V. CONCLUSION

As a result of the investigation of signal strength fading at 108 mc several conclusions seem indicated. There seems to be little doubt that the strength of the signal received from Explorer VI at the Hawaii and Singapore ground stations actually showed variations in intensity which are attributable to other factors than possible equipment difficulties: the consistent occurrences of the fading in time and place as well as the geographic distribution of occurrences of fading at both Singapore and Hawaii render any explanation based on man-made phenomena at the ground station extremely difficult to sustain, and satellite transmitter difficulties seem to be eliminated as a possible cause by the observation of signal fading at one station simultaneously with regular transmission to another station.

The rather peculiar localization of the fading occurrences in a particular region of magnetic latitude for both northern and southern hemispheres seems to indicate some relationship with the ionosphere. This indication is further substantiated by the fact that occurrences of fading are localized in a portion of the ionosphere which Wright has already described as having an unusually high electron density during the early evening hours. The fact that except for brief periods of fading of from 1 - 2 minutes duration all fading began and continued after the local sunset in the portion of the ionosphere propagating the signal indicates that the causal phenomenon in the ionosphere begins shortly before or at local sunset.

An admittedly crude theoretical model which considers the fading as due to scattering by an irregular distribution of electrons in this high electron density belt indicates that fading of the severity observed could well be expected from such a process. Since the model used predicts only minor changes in phase, the most likely explanation for the fluctuations in signal level under this model would be statistical changes in the number of irregularities encountered by the signal propagating through the medium. Such random changes might result from:

1) the movement of the ray through the ionosphere, i.e., the motion of the source through the sky; 2) the movement of the ionosphere through the ray, i.e., ionospheric winds; 3) the processes creating the irregularities might have time constants brief enough to cause sufficiently rapid temporal variations in the medium. Since no correlation was found between the frequency of fading and the velocity of the ray through the ionosphere, the latter two effects seem to be the most likely explanations for rapid signal level fluctuations for processes similar to this model.

The observations of signal strength fading at 108 mc all seem to be compatible with a model of the ionosphere which postulates a region of high electron density which is maintained by a process which shows a diurnal cycle; after local sunset, irregularities, or blobs, appear in the electron density distribution; a VHF signal propagating through the ionosphere during this time scatters a sufficiently large portion of its energy from the blobs as to suffer attenuation on the order of 20 decibels.

The occurrences of signal strength fluctuation at 378 mc are unfortunately too sparse to provide a definitive description of any UHF fading. The fact that the UHF signal fluctuations occurred only when the VHF signal was fading, lends credence to the belief that the UHF fluctuations are also associated with an ionospheric phenomenon. The data is too scarce to more than indicate the possibility of some ionospheric phenomenon producing fading at UHF. The explanation suggested for the VHF fading is clearly not applicable to the UHF occurrences since the model of scattering used predicts that an ionosphere that would produce the observed level of scattering at UHF would cause the VHF signal to be completely lost; a prediction at variance with the observations. The possibility does exist that some sort of multipath phenomenon might account for the UHF fluctuations since some form of multipath phenomenon is perhaps suggested by the preliminary slow fading noted in the VHF fading. The occurrences of UHF signal fluctuation are not sufficiently numerous or substantiated to provide a basis for a more detailed investigation or explanation.



#### ACKNOWLEDGEMENTS

It is a pleasure to acknowledge the collaboration with Carl D. Graves in the early stages of this investigation. Conversations with and the suggestions of many of the members of the Theoretical Physics Department were extremely helpful; in particular, however, should be noted the aid of William C. Meecham and Paul Molmud. Prof. Nakagami of Kobe University first indicated the possible relevance of Wright's results to the signal fading investigations. Finally, recognition should be given to the considerable contribution made to this investigation by Despina Wilson who performed all the required computation and data reduction.

## REFERENCES

- Gordon, W. E., "Investigation of Air-to-Air and Air-to-Ground Electromagnetic Propagation". Res. Rep. EEL63, 15, Cornell University, Ithaca, N. Y.; September, 1953.
- Ratcliffe, J. A. and Weekes, K., "The Ionosphere" in "Physics of the Upper Atmosphere" edited by J.A. Ratcliffe, Academic Press, New York, 1960; pp. 377 - 470.
- Wright, J. W., "A Model of the F Region above  $h_{\max}$  F2", Jour. of Geophys. Res., Vol. 65, No. 1, Jan. 1960; pp. 185 - 191.

## APPENDIX

In studies of the ionosphere it is quite often useful to know the magnetic latitude  $\ell_m$  of the point at which a straight line (line-of-sight) with given elevation angle  $E$  and azimuth angle  $A$  directed from a point of known latitude  $\ell_{gs}$  and longitude  $\lambda_s$  on the earth's surface attains a given height,  $h$ , above the earth.

Consider, first, the following set of spherical triangles (Figure 1) in which we shall let  $P$  represent the geographic north pole,  $M$  the magnetic north pole,  $T$  the known  $\lambda_s$  and  $\ell_{gs}$ ;  $S$  is now the radial projection onto the earth's surface of the point whose magnetic latitude is desired. Hence  $\widehat{MS}$  is now the desired magnetic latitude and from

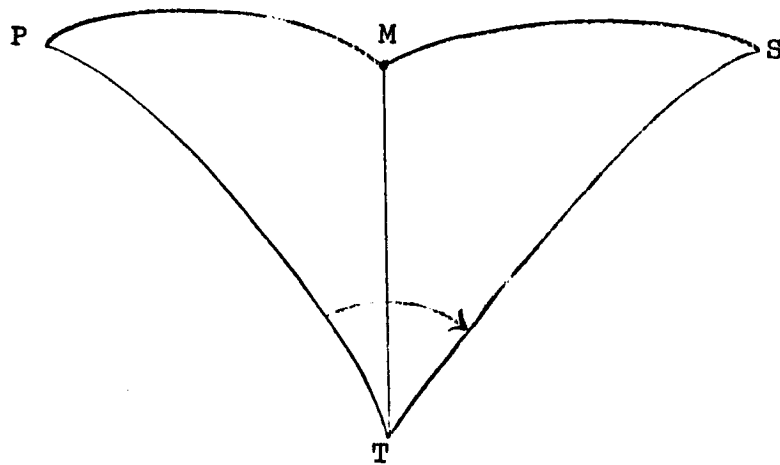


Figure 1.

the cosine law of spherical trigonometry

$$\cos \widehat{MS} = \cos \widehat{MT} \cos \widehat{TS} + \sin \widehat{MT} \sin \widehat{TS} \cos \angle MTS \quad ;$$

similarly  $\widehat{MT}$  may be found from

$$\cos \widehat{MT} = \cos \widehat{PT} \cos \widehat{PM} + \sin \widehat{PT} \sin \widehat{PM} \cos \angle TPM \quad .$$

Now  $\angle MTS = A - \angle PTM$  and from the sine law

$$\frac{\sin \angle PTM}{\sin \angle PMT} = \frac{\sin \angle TPM}{\sin \angle TMT} \quad \cdot$$

The arc length  $\widehat{TS}$  now only needs to be found and that may be easily derived by considering Figure 2, where the line TQ is tangent to the circle at point T. By plane trigonometry, we have

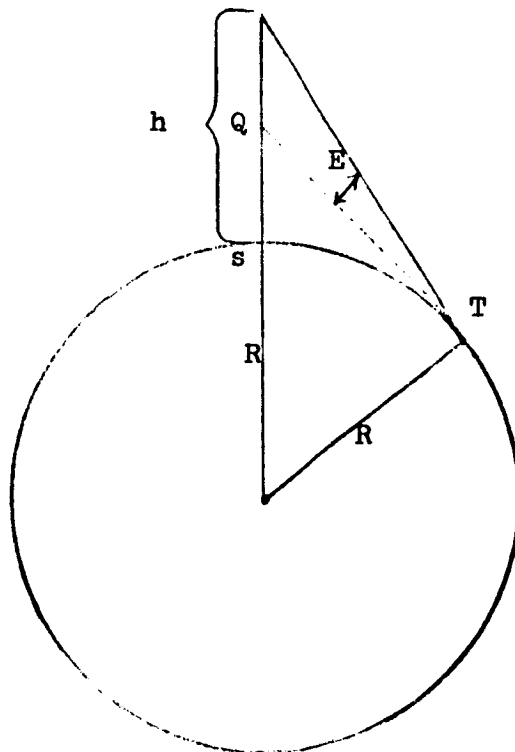


**Figure 2.**

$$\frac{R + h}{\sin \left( \frac{\pi}{2} + E \right)} = \frac{R}{\sin \left( \frac{\pi}{2} - \widehat{TS} - E \right)} \quad \text{or} \quad \widehat{TS} = \cos^{-1} \left\{ \frac{R}{R + h} \cos E \right\} - E .$$

Letting the latitude and longitude of the north magnetic pole be  $l_{gm}$ ,  $\lambda_m$  respectively, we can identify  $\widehat{PT} = \frac{\pi}{2} - l_{gs}$ ,  $\widehat{PM} = \frac{\pi}{2} - l_{gm}$ ,  $\angle TPM = \lambda_s - \lambda_m$ ,  $\widehat{MT}$  = mag. colatitude of point T and angle PTM as the direction of magnetic north from point T.

Thus, we have

$$\sin l_m = \cos \widehat{MT} \cos \widehat{TS} - \sin \widehat{MT} \sin \widehat{TS} \cos \angle MTS ,$$

where

$$\cos \widehat{MT} = \sin l_{gs} \sin l_{gm} + \cos l_{gs} \cos l_{gm} \cos (\lambda_s - \lambda_m)$$

$$\widehat{TS} = \cos^{-1} \left[ \frac{R}{R + h} \cos E \right] - E$$

$$\angle MTS = A - \sin^{-1} \left[ \frac{\cos l_{gm}}{\sin \widehat{MT}} \sin \right] (\lambda_s - \lambda_m)$$

Note that  $\lambda_s$ ,  $\lambda_m$  are measured in west longitude and the azimuth is measured towards the east from north.

Another quantity of interest in ionospheric studies is the time of sunset,  $t_{ss}$ , of a point at height  $h$  above a point of known latitude and longitude.

Consider Figure 3; let P and P' be the north and south poles of the earth, respectively; let T be the point of known latitude and longitude; let S be the point of intersection with the earth's surface of the line directed from the earth's center to the solar center at time  $t_{ss}$ . EBA represents the equator and PAP' represents the prime

meridian; DCF represents the sunset line on the earth at time  $t_{ss}$ .  $\widehat{TCS}$  represents the great circle from T to S. We immediately note that  $\angle APT$  is the west longitude of T and  $\widehat{BT}$  is the latitude of T; also  $\widehat{SE}$ , and consequently  $\widehat{DP}$ , is the apparent declination of the sun,  $\alpha$ .

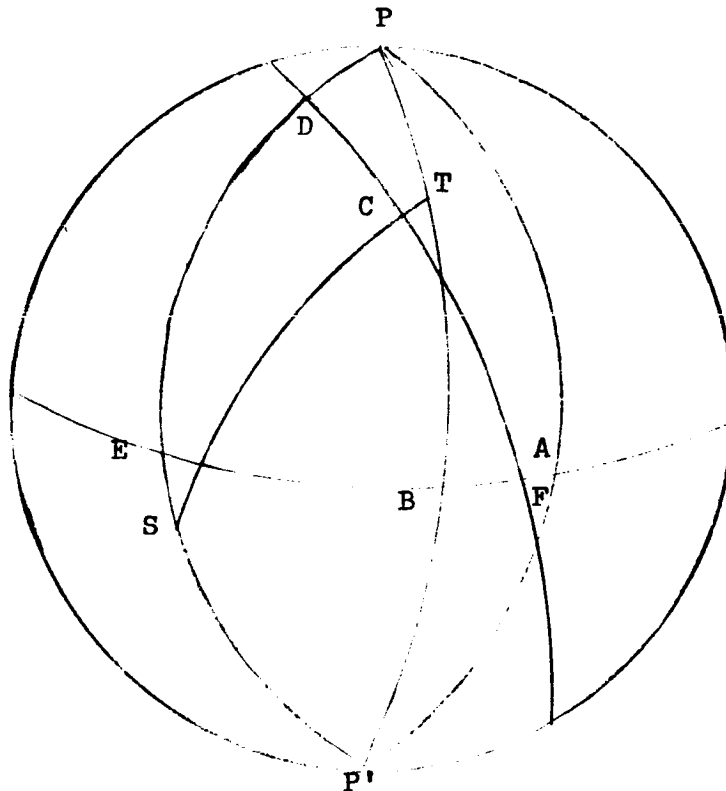


Figure 3.

Letting  $\omega$  represent the angular rate of the earth, we have:

$$t_{ss} = \frac{\angle APE}{\omega} = \frac{\angle APB + \angle BPE}{\omega}. \text{ For simplicity, let the west longitude } \angle APT \text{ be } \lambda_0; \text{ let the latitude } \widehat{BT} \text{ be } \ell, \text{ and let } \angle BPE = \lambda_1. \text{ Now } \lambda_0 \text{ is known and the cosine law gives}$$

$$\cos \widehat{ST} = \cos \widehat{SP} \cos \widehat{PT} + \sin \widehat{SP} \sin \widehat{PT} \cos \angle BPE$$

Arc lengths  $\widehat{SP}$  and  $\widehat{SC}$  are obviously  $\frac{\pi}{2}$ .  $\widehat{SP}$  is thus  $\frac{\pi}{2} + \alpha$ . A cross section through SCT and the center of the earth resembles Figure 2, with  $E = 0$ . Thus  $\widehat{CT} = \cos^{-1} \frac{R}{R+h}$ , where  $R$  is the earth's radius.  $\widehat{ST}$  immediately follows as  $\frac{\pi}{2} + \widehat{CT}$ . Eq. (1), letting  $\widehat{CT} \equiv \beta$ , becomes:

$$\cos\left(\frac{\pi}{2} + \beta\right) = \cos\left(\frac{\pi}{2} + \alpha\right) \cos\left(\frac{\pi}{2} - l\right) + \sin\left(\frac{\pi}{2} + \alpha\right) \sin\left(\frac{\pi}{2} - l\right) \cos,$$

and solving easily for  $\lambda_1$ :

$$\cos \lambda_1 = \tan \alpha \tan l - \frac{\sin \beta}{\cos \alpha \cos l}$$

and

$$t_{ss} = \frac{\lambda_1 + \lambda_o}{\omega}$$

CHAPTER V

SATELLITE SIGNAL FLUCTUATION CAUSED  
BY IONOSPHERIC IRREGULARITY

by

W. C. Meecham



## I. INTRODUCTION

We shall be concerned here with the fluctuations in signal strength observed in signals received from the satellite Explorer VI. The launch date for this satellite (with the international designation 1959 8) was August 7, 1959. The orbit was quite eccentric with a perigee of 115 miles and an apogee of 24,618 miles giving a period of about 754 minutes. The apogee appeared on the night side of the earth. Two signals of importance here were transmitted from the satellite; one, VHF, from a transmitter operating at about 108 megacycles on a power of 500 milliwatts, the other, UHF, at about 378 megacycles on a power of about 5 watts. Transmission continued until October 6, 1959. We are interested here in the two receiving stations located at Hawaii and Singapore. At these stations signals were received and recorded at intervals from August to October. At Hawaii two different reception systems were employed for the most part a parabolic reflector with a dipole element was used. A system of 16 helical end fire antennas was also available. These were arranged in groups of four, each group located on the corner of a square with dimension order of a few hundred meters. Although this latter system was well suited to phase fluctuation measurements, it was little used because of its lower gain. At Singapore one group of four helical end fire arrays was available and used. The helical arrays of course had the advantage (or disadvantage) that they did not register polarization effects. The communication system had a phase lock and most of the information was carried by frequency modulation. We shall limit attention to the fluctuation in signal strength, ignoring all other characteristics. At times the signal fluctuation was so great that the signal dropped out of lock and was lost.

The general characteristics of the signal fluctuation are as follows. First the fluctuation was moderate amounting to a few db until some time in the evening. This fluctuation was due mainly to satellite rotation. Then over a period of a few minutes there was a marked increase in the level of the fluctuation until its extreme values, peak to peak, were 10 to 15 db. This large fluctuation lasted throughout the night. Sometime about sunrise the fluctuation again decreased to its daytime value. The diurnal effect was observed at both equatorial stations. The amount of fluctuation was considerably greater for VHF (the lower frequency) than for UHF. A sample record is reproduced in Figure 1. Further it has been found that the fluctuation was greater for signals which propagated through regions some 10 or 15 degrees north or south of the magnetic equator. For a more detailed description of the experiment as well as of some of the characteristics of the fluctuation see a report by Gore.<sup>1</sup>

A possible explanation for the signal fluctuation is the following.<sup>2</sup> Due to the changing electron density as one passes through the ionosphere, an electromagnetic ray will be refracted. At certain angles, predominantly near grazing incidence, there may be two (or more) rays connecting the satellite source and the receiver located on the earth's surface. These rays would have fluctuating phase, due to the fluctuating electron densities in the ionosphere, and consequently the received signal would fluctuate. The process is usually known as a multipath phenomena. This explanation is rejected for the following reasons, among others. First, the phenomena would not appear for rays significantly above the horizon, which is not observed to be the cause. Secondly, the amplitude probability distribution, assuming the two rays of

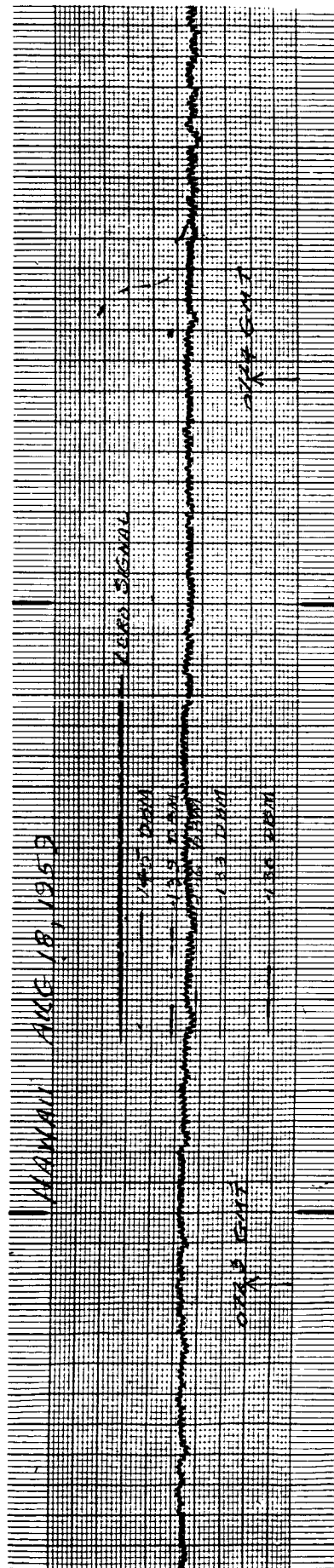


Figure 1. Normal Signal Strength Recording Without Fading.

nearly the same amplitude, would be very far from the modified Rayleigh distribution which is observed. Of course one might propose that the amplitudes of the rays also fluctuate. But then this theory merely begs the question, for if the amplitudes fluctuate significantly a multipath process is not required. Indeed one is left with the problem of explaining that fluctuation.

It is proposed here that the cause of the signal fluctuation is the same as that presumed to cause the fluctuation in signal strength from radio stars, namely the fluctuation is caused by fluctuations in electron density in the ionosphere. It seems reasonable to suppose that the most important fluctuations occur where the electron density is the highest, the F-layer at levels of from 200 to 500 km.<sup>3</sup> In the next section the theory of such signal fluctuations is reviewed.

In Section III the data treatment is discussed. In this work three characteristics of the data have been calculated. The autocorrelation function of the signal amplitude for selected segments of the signal record is presented. Secondly the F. T. (Fourier Transform) of the autocorrelation function, the powerspectrum function, has been computed for the same signal records. Thirdly the amplitude probability density function has been obtained. Finally the major conclusions and suggestions for future work are presented in Section IV.

## II. REVIEW OF THEORY

The theory of the fluctuations in signals produced when propagation occurs in a randomly inhomogeneous medium has been presented elsewhere.<sup>4-7</sup> The salient characteristics and results of this theory will be reviewed here. The treatment is for a scalar field.<sup>8</sup>

A standard problem to be considered is the following. We are given a point source at a single frequency  $\omega_0$  defining a propagation constant  $k_0 \triangleq \omega_0/c_0$  where  $c_0$  is the velocity of propagation. Then the equation to be solved is

$$\left\{ \nabla^2 + k_0^2 [1 + U_{st}(\underline{r})] \right\} \left\{ G_0(\underline{r}, \underline{r}_0) + G_{st}(\underline{r}, \underline{r}_0) \right\} = \delta(\underline{r} - \underline{r}_0) \quad (1)$$

where  $U_{st}$  gives the fluctuation in the medium and  $G_{st}$  gives the fluctuation in the Green's function (point source solution) and  $G_0$  is the average Green's function. We suppose

$$\langle U_{st} \rangle = \langle G_{st} \rangle = 0. \quad (2)$$

To proceed with the solution we first put all terms of (1) on the R. S. (right side) except  $(\nabla^2 + k_0^2) G_{st}$ . Then treating the R. S. as a source and using the Green's function for this operator, the problem of finding  $G_{st}$  is formulated as an integral equation. Next we assume that the fluctuation  $U_{st}$  is small, and save lower order terms. It is emphasized that we in this way obtain only the lowest order solution for the Green's function. After averaging, the equation for  $G_0$  is found to be,

$$(\nabla^2 + k_0^2) G_0(\underline{r}, \underline{r}_0) + \frac{k_0^4}{4\pi} \int d\underline{r}' \frac{e^{ik_0(\underline{r} - \underline{r}')}}{(\underline{r} - \underline{r}')} G_0(\underline{r}', \underline{r}_0) H(\underline{r} - \underline{r}') = \delta(\underline{r} - \underline{r}_0) \quad (3)$$

where

$$H(\underline{r} - \underline{r}') \equiv \langle U_{st}(\underline{r}') U_{st}(\underline{r}) \rangle \quad (4)$$

is the correlation function of the medium fluctuation, which is assumed to be statistically homogeneous. We then take the F. T. of (3) and in this way

find for  $G_o$

$$G_o(\underline{r} - \underline{r}_o) = -\frac{1}{4\pi} \frac{e^{iS_o|\underline{r} - \underline{r}_o|}}{|\underline{r} - \underline{r}_o|}$$

where

$$S_o \approx k_o + \frac{k_o^2}{2} \left\{ \frac{1}{8\pi^2} \int_0^\infty kh(k) \ln \frac{k + 2k_o}{|k - 2k_o|} dk + \frac{i}{8\pi} \int_0^{2k_o} kh(k) dk \right\} \quad (5)$$

with  $h(k)$  the F.T. of  $H$ .

For a specific example we now suppose a Gaussian correlation  $H$ ,

$$H(R) = A^2 e^{-R^2/a^2} \quad (6)$$

where  $A^2$  gives the mean square of the amplitude of the fluctuation and  $a$  is the correlation length. We find from this example that the attenuation,  $\text{Im}\{S_o\}$ , is proportional to  $\frac{(\pi)^{1/2}}{8} k_o^2 A^2 a$  for high frequencies ( $k_o a \gg 1$ ) and to  $k_o^4 A^2 a^3$  for low frequencies ( $k_o a \ll 1$ ). We shall be interested here in the high frequency result. It is worth emphasizing that in either frequency range only the largest scale irregularities are important.

Before proceeding with a discussion of the statistical characteristics of the signal amplitude, we shall estimate from the above results the amount of noise to be expected on satellite signals. The inhomogeneity responsible for the signal fluctuation is most probably the variation in electron density in the F layer. We begin by briefly reviewing the electromagnetic propagation characteristics of ionized media. Magnetic field effects will be neglected. For large frequencies it is well-known that the index of refraction is given by,

$$\mu = 1 - \frac{w_p^2}{w^2} \quad (6a)$$

where

$$w_p^2 = \frac{4\pi e^2}{m} (n_0 + \Delta n) \equiv w_{p0}^2 \left(1 + \frac{\Delta n}{n_0}\right) \quad (6b)$$

with  $n_0$  the average electron density and  $\Delta n$  its fluctuation. Then referring to (1) where we note

$$1 + U_{st} = n^2, \quad (6c)$$

we see

$$k_o^2 = \frac{w^2}{c^2} \left(1 - \frac{w_{p0}^2}{w^2}\right) \approx \frac{w^2}{c^2} \quad (6d)$$

the last relation holding for high frequencies, we see

$$U_{st} = - \frac{4\pi e^2}{mw^2} \Delta n, \quad (6e)$$

$$= - \frac{w_{p0}^2}{w^2} \frac{\Delta n}{n_0} \quad (6f)$$

thus

$$A^2 = \frac{4\pi e^2}{mw^2}^2 \langle \Delta n^2 \rangle, \quad (6g)$$

$$= \frac{w_{p0}^4}{w^4} \langle \Delta n \rangle^2. \quad (6h)$$

Now we refer to the result for the attenuation of the coherent beam given in (5) and (6). Further, it is remarked that the square of the noise field plus the square of the coherent beam must fall off like  $\frac{1}{r^2}$  since the total energy is conserved. Then for high frequencies ( $k_0 a \gg 1$ ), we have

$$\begin{aligned}
E_n^2 &= \left(\frac{1}{4\pi}\right)^2 \frac{1}{|\underline{r} - \underline{r}_0|^2} (-2) \operatorname{Im} \left\{ r_0 \right\} |\underline{r} - \underline{r}_0| \\
&\approx \frac{\pi^{1/2}}{4} \frac{k_o^2 A^2 a}{|\underline{r} - \underline{r}_0|} ,
\end{aligned} \tag{6i}$$

with  $E_n^2$  the mean square noise at  $|\underline{r} - \underline{r}_0|$  and  $E_{no}^2$  the corresponding quantity at unit distance. The coherent signal is given by

$$G_o^2 = \left(\frac{1}{4\pi}\right)^2 \frac{1}{|\underline{r} - \underline{r}_0|^2} \left[ 1 + 2 \operatorname{Im} \left\{ s_o \right\} |\underline{r} - \underline{r}_0| \right] . \tag{6j}$$

The results are given to lowest order only. For the problem under consideration here the source is usually located outside the ionized medium. The signal will be presumed to traverse a path length  $L$  in the inhomogeneous medium. Then the factors  $|\underline{r} - \underline{r}_0|$  in the numerators of (6i) and (6j) should be replaced by  $L$ . The fraction of noise (energy) to coherent signal is given by

$$\frac{N^2}{S^2} = \frac{\text{Noise Energy}}{\text{Signal Energy}} = \frac{\pi^{1/2}}{4} k_o^2 A^2 a L \tag{6k}$$

valid when small. Now substituting from (6g) and (6h) we see

$$\frac{N^2}{S^2} = \frac{\pi^{1/2}}{4 c^2} \left( \frac{4\pi e^2}{mw} \right)^2 a < \Delta n^2 > L , \tag{6l}$$

$$= \frac{\pi^{1/2}}{4} k_o^2 a L \left( \frac{w_{po}}{w} \right)^4 < \left( \frac{\Delta n}{n_o} \right)^2 > . \tag{6m}$$



From (6l) we see the interesting result that the noise to signal is inversely proportional to the frequency squared and directly proportional to

$$\langle \Delta n^2 \rangle L = \int_0^L (\Delta n)^2 dx \quad (6n)$$

where the integral covers the path through the inhomogeneous medium. We may reasonably extend this result to allow the possibility that  $\Delta n$  changes as a function of position, provided the change is slight in a distance  $a$ . It is emphasized from (6l) that  $N^2/S^2$  is proportional to the actual electron density fluctuation, not the relative fluctuation.

We consider as an example, propagation of VHF through the ionosphere. Suppose  $\langle (\frac{\Delta n}{n_0})^2 \rangle \sim 10^{-4}$  and  $a \sim 10^5$  cm. (reasonable values from radio astronomical work);  $\frac{w_{po}}{w} \sim 10^{-1}$  (about right for F layer and VHF with frequency of 100 megacycles) and using  $k_0 = \frac{2\pi}{300} \text{ cm}^{-1}$ , we find the noise is of the same order as the signal for  $L \sim 25$  km. The F layer is actually considerably thicker than this. We conclude that the large fluctuations observed on satellite signals at VHF frequencies are quite reasonable on the basis of a model based on electron density fluctuations as described previously.

It is emphasized, as seen in (6l), that the noise to signal energy falls off inversely as the frequency of the signal squared. Thus the fluctuation of UHF is reduced by a factor of about 1/8. This is in accord with the observation that UHF fluctuations are much smaller in general than VHF.

In the above way we obtain the change in the average or coherent signal. It is seen that such changes, in this information, occur to

lowest order only as a result of double scatterings. The fluctuations about this average are also of interest. These are mainly caused by single scattering. To lowest order it is easily seen<sup>4</sup> that the fluctuation is given by

$$G_{st}(\underline{r}, \underline{r}_0) = -\frac{k_0^2}{(4\pi)^2} \int \frac{e^{ik_0|\underline{r} - \underline{r}'|}}{|\underline{r} - \underline{r}'|} U_{st}(\underline{r}') \frac{e^{ik_0|\underline{r}' - \underline{r}_0|}}{|\underline{r}' - \underline{r}_0|} d\underline{r}'. \quad (7)$$

In the present application  $U_{st}$  is very small, so the scattering is mainly in the forward direction. Hence important elements in the integral lie mainly on and near the line connecting  $\underline{r}$  and  $\underline{r}_0$ .

We wish now to deduce something about the distribution of  $G_{st}$ . If a typical single scattering event is such that the phase shift is of order  $2\pi$  or larger, and if there are many scattering volumes between source and receiver, that is if the correlation length is small compared with the length of path through the inhomogeneous medium,  $G_{st}$  is obtained as the result of a random walk in two dimensions (in the complex plane). Further phase shift of order  $2\pi$  means that the individual contributions are statistically independent. Hence  $G_{st}$  has a Gaussian distribution for its real and imaginary parts. On the other hand if the phase shift at a single scattering is smaller than  $2\pi$  the scattered signal will be correlated with the average signal. One sees an interesting characteristic of the phase shift of the single scattered contribution from (7). For all elements on the line from source to receiver, the phase shift is either 0 or  $\pi$ , depending on the result of the integral over  $U_{st}$ . The signal amplitude would then be Gaussian about the average signal. This is to be compared with the modified Rayleigh expected when both the real and imaginary parts of the scattered signal are

Gaussian distributed. To see that the phase shift is 0 or  $\pi$  note that the phase of the coherent wave is except for a fixed sign, given by

$$\exp \left\{ i k_0 \left[ | \underline{r} - \underline{r}' | + | \underline{r}' - \underline{r}_0 | \right] \right\}$$

regardless of the value of  $\underline{r}'$ , if  $\underline{r}'$  lies on the source-receiver line. These are complications which, after more experimental evidence is in, could bear some theoretical investigation.

We turn now to the amplitude probability distribution for the received signal, composed of an average signal with a noise signal superimposed. We consider here the sum of a constant average signal plus a random noise signal, assumed to have a Gaussian distribution,

$$P_n = \frac{1}{\pi a^2} e^{-A_n^2/a^2} \quad (8)$$

where  $P_n A_n dA_n d\theta_n$  is the probability the noise signal has amplitude in the range  $(A_n, A_n + dA_n)$  and phase in the range  $(\theta_n, \theta_n + d\theta_n)$ . Let the average signal have amplitude  $A_0$ . We wish the probability distribution of the amplitude of the sum of the average signal plus the noise. This is easily found to be,<sup>9</sup>

$$P(A) = \frac{2A}{a^2} e^{-\frac{1}{a^2}(A^2 + A_0^2)} J_0 \left( i \frac{2AA_0}{a^2} \right) \quad (9)$$

where  $A$  is the sum of the average signal plus noise, and with  $J_0$  the zeroth order Bessel function. In the limit where the  $A_0 \rightarrow 0$ , this becomes the Rayleigh distribution,

$$\begin{aligned} P(A) &\rightarrow \frac{2}{a^2} A e^{-A^2/a^2} \\ A_0 &\rightarrow 0 \end{aligned} \quad (10)$$

We are also interested in the moments of  $A$ . The following result is easily found,<sup>10</sup>

$$\begin{aligned} \langle A^{\mu-2} \rangle &= a^{\mu-2} \int_0^\infty \left(\frac{\mu}{2}\right) e^{-(A_0/a)^2} {}_1F_1\left(\frac{\mu}{2}; 1; \left(\frac{A_0}{a}\right)^2\right) \\ &\mu \geq 2, \text{ integer,} \end{aligned} \quad (11)$$

where  ${}_1F_1$  is the Kummer function (see e.g. reference in note 10, p. 86). From (11) we can readily find the ratio of the standard deviation to the average signal to the corresponding quantities,

$$\frac{\langle (A - \langle A \rangle)^2 \rangle^{1/2}}{\langle A \rangle} = \left\{ \frac{4}{\pi} e^{(A_0/a)^2} \frac{{}_1F_1(2; 1; (A_0/a)^2)}{\left[{}_1F_1\left(\frac{3}{2}; 1; (A_0/a)^2\right)\right]^2} - 1 \right\}^{1/2} \quad (12)$$

This relation can be used to deduce the ratio of signal to noise,  $A_0/a$ , from the measured standard deviation and the measured average signal. The relation (12) is plotted in Figure 2.

From (10) one sees that  $a$  is the standard deviation of the noise signal. When the coherent signal  $A_0$  goes to zero one finds the Rayleigh distribution result from (12), which becomes  $(\frac{4}{\pi} - 1)^{1/2}$ .

Before closing this section, it will be helpful to discuss the autocorrelation function and the power spectrum function. The autocorrelation is defined,

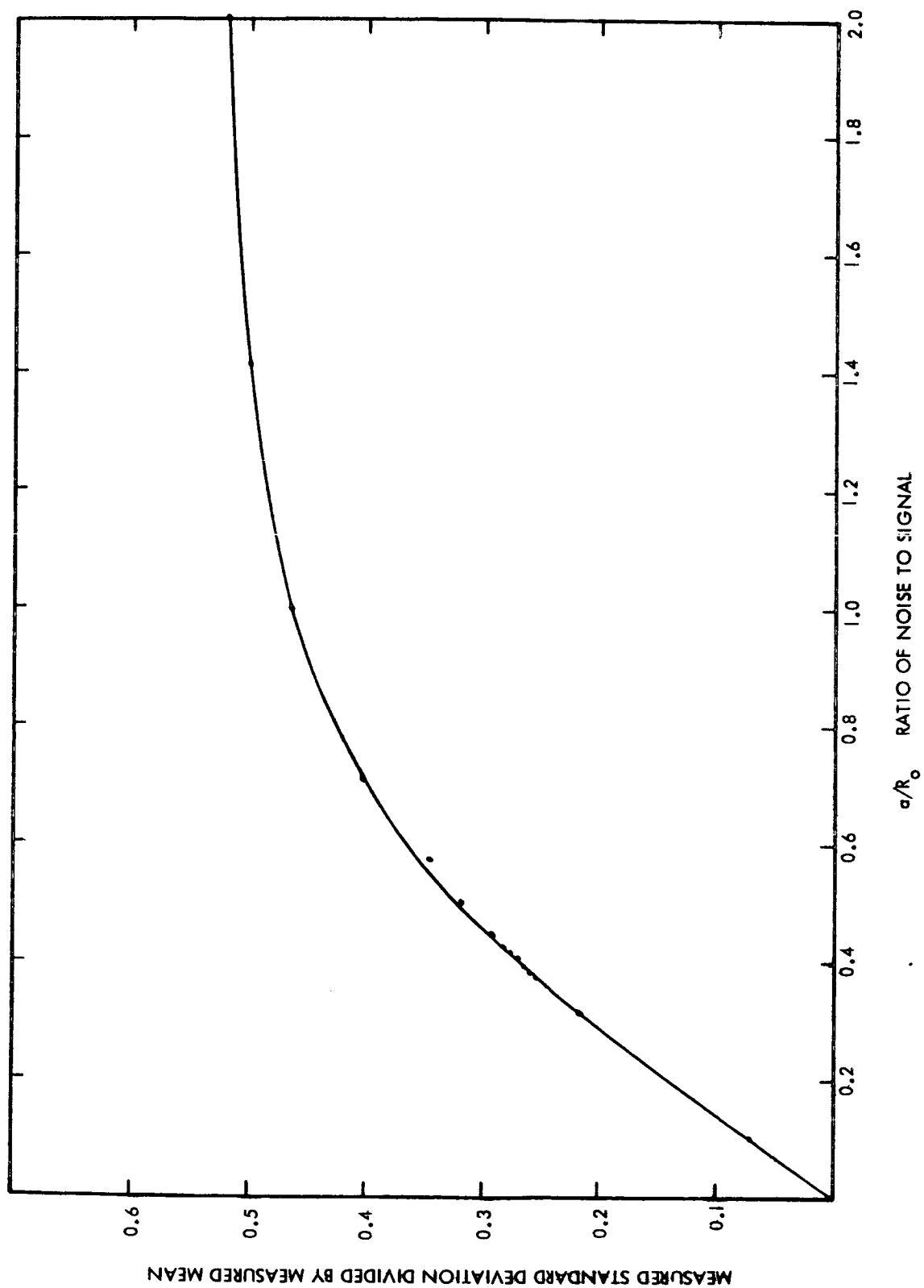


Figure 2. Relation Between Measured Standard Deviation Divided by Measured Signal Mean to Noise Divided by Signal.

$$\langle A(t) A(t + \tau) \rangle = C(\tau) \equiv \frac{1}{T} \int_0^T A(t) A(t + \tau) dt \quad (13)$$

for  $T$  large. Using a well-known relation we have for the power spectrum

$$D(\omega) = \frac{2}{\pi} \int_0^{\infty} C(\tau) \cos \omega \tau d\tau \quad (14)$$

where  $D$  has the meaning,

$$D = \lim_{T \rightarrow \infty} \frac{2\pi}{T} |A_T(\omega)|^2 \quad (15)$$

and

$$A_T(\omega) \equiv \frac{1}{2\pi} \int_0^T e^{-i\omega t} A(t) dt. \quad (16)$$

As remarked earlier, we shall have occasion to consider signals  $A$  containing discrete frequencies. We let

$$A = A_c \cos \omega t + N(t) \quad (17)$$

where  $N$  is the noise signal. Then it is easily seen from (13) that for large  $T$ ,

$$C_{\text{Total}}(\tau) = \frac{1}{2} A_c^2 \cos \omega \tau + C(\tau) \quad (18)$$

with  $C$  the correlation of the noise. In such a case we expect the correlation to become sinusoidal for large delays  $\tau$ . As mentioned, it will be seen that this occurs for signals considered here.

### III. TREATMENT OF DATA

The data considered here were taken at the Hawaii station after 7 A. M. on the morning of August 18, 1959. Identification is given in seconds after that time. The frequency was VHF in every case. We shall designate the record taken from 1794 sec. to 1974 sec. (after 7 A. M.) as Case I; 3354 to 3774 sec. as Case II. A few other signal record segments have been treated; the results presented here are representative.

In Figure 3 the autocorrelation function for Case I can be seen. We note first that the time for the correlation function to fall to half value is about a quarter second, i.e. the characteristic time for the fluctuation is of that order. The sinusoidal variation due to the satellite spin is clearly evident. Using the result given in (18) one finds upon averaging over the correlation curve an amplitude  $A_c = 11$  in the units of the correlation function. The spin frequency is found, again after averaging, to be about 2.67 cycles per second. This frequency is more readily found from the power spectrum function (see below). The lower regular frequency, presumably due to rotation of the satellite about another axis, can also be discerned. An accurate determination of this frequency would require the calculation of the correlation function for longer delay times. Nevertheless one can estimate that the frequency is about 0.5 cps. As mentioned earlier, there is probably a third rotation frequency present, but more calculation is required to determine it. The calculation of the underlying autocorrelation function must be considered unreliable when the value of the function drops much below 300 as a result of the regular frequency contamination. The removal of such regular variation is evidently quite desirable for this and other purposes. The correlation function for Case II is very similar to Case I and is not reproduced here.

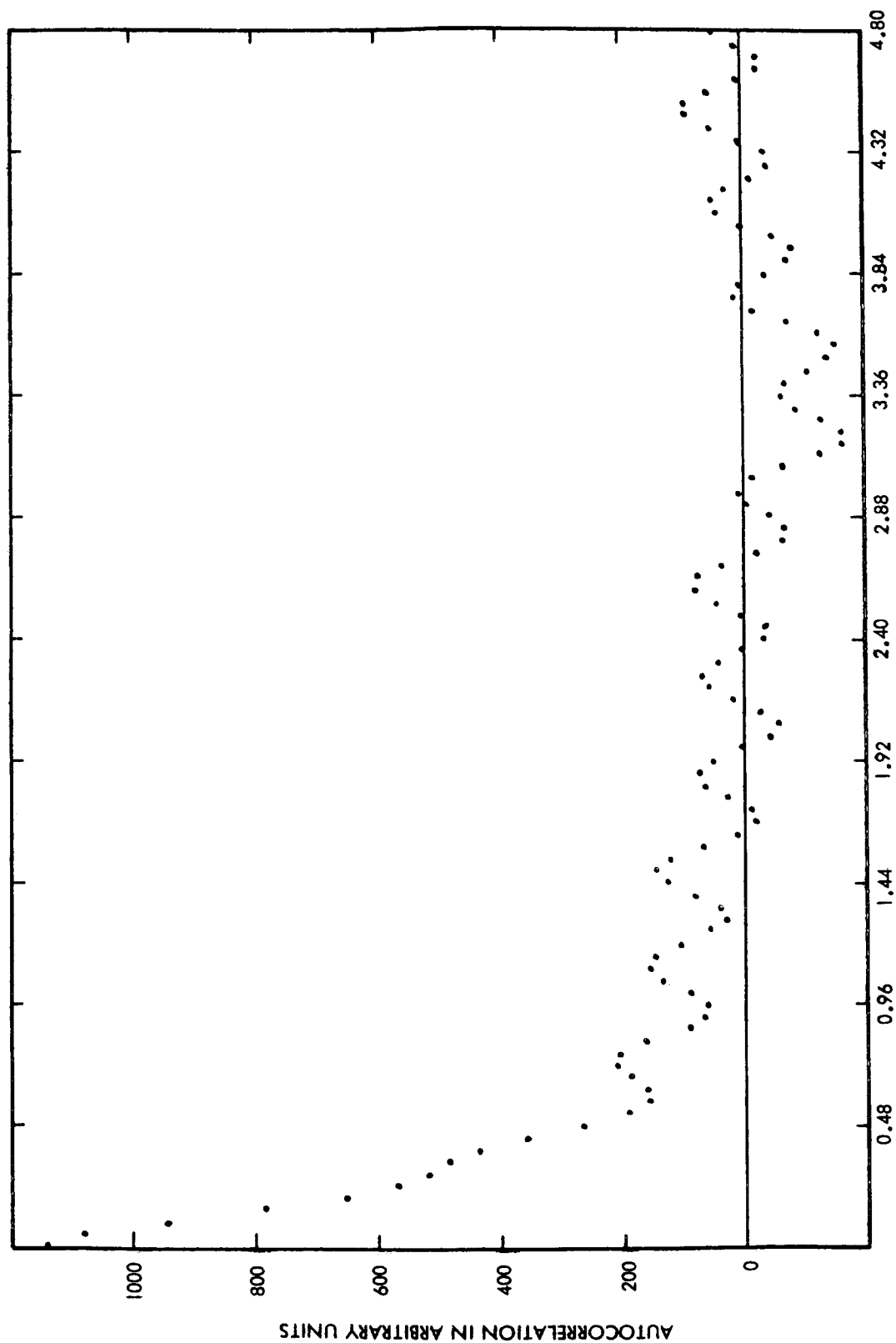


Figure 3. Autocorrelation Function For Case I



The short correlation time is interesting. Let us consider the time which it takes the ray from the satellite to the receiver (on the earth's surface) to cross the blob of size order one kilometer the blob located at a presumed height of 400 km. A typical angular rate for the indicated ray varies from about zero to a maximum of about a radian per hour. The more rapid change occurs only when the satellite is near the earth. The time for the ray to cross the blob is seen to be about 10 sec. This is almost two orders of magnitude too slow to explain the signal correlation time. We conclude tentatively that the signal fluctuation correlation time must be determined by the correlation time for the medium fluctuation. Gore<sup>1</sup> has run correlations between the satellite angular rate and the signal fluctuation rate (determined roughly) and found no correlation, in keeping with these remarks.

We turn now to the power spectrum function, the Fourier Transform of the correlation function [see (14)]. The plot of this function is shown in Figure 4 for Case I. The calculation is not entirely satisfactory, due to a spurious peak at zero frequency. We shall be mainly interested here in the peaks in the power spectrum function, which are believed to be reliable. The most prominent of these is that arising from the spin, at about 2.67 cps. The second peak expected at about 0.5 cps can be imagined at least at a little less than that value (not so much a peak as a halt in the rate of fall-off of the curve). There are other slight peaks which may turn out to be interesting after further computation. For instance there is an indication at  $3/4$  cps, 2 cps, and some which may or may not be reliable at higher frequencies. To check on the persistence of these other peaks, the spectrum function for Case II has been presented in Figure 5. Aside from

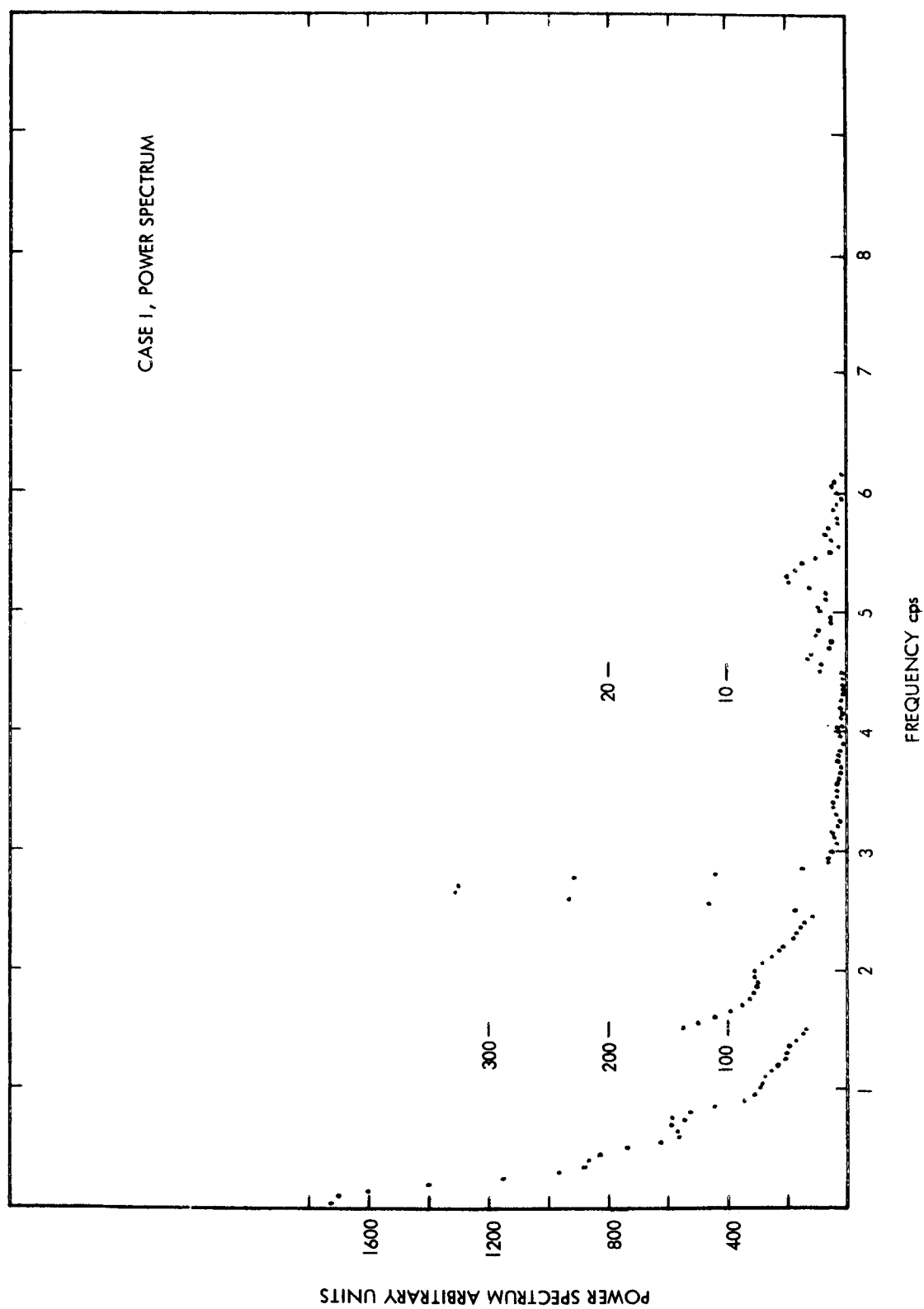


Figure 4. Case I. Power Spectrum.

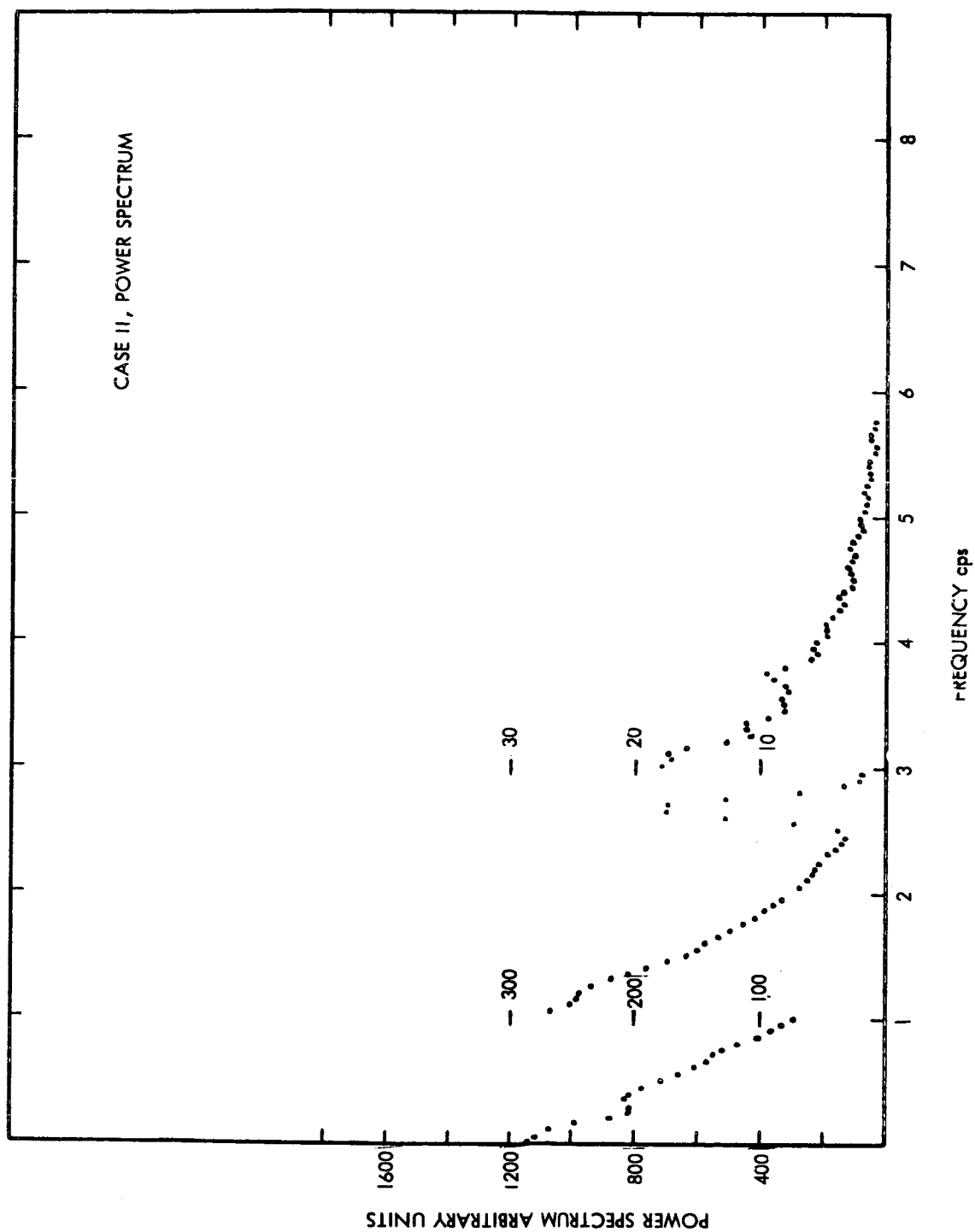


Figure 5. Case II, Power Spectrum

the expected spin frequency we see more evidence of a peak at a little less than 0.5 cps (perhaps the other rotation) almost nothing at  $3/4$  cps, nothing at 2 cps and the higher frequency peaks have shifted in value. In the half hour or so of elapsed time between the two calculations, it is seen that the peaks, other than those due to rotation, have shifted. These peaks offer the intriguing possibility that there are discrete frequency waves in the ionosphere, whose frequencies change in times of order  $1/2$  hour. Of course we must allow the possibility that they are merely random fluctuations in the data. Again further calculations investigating these possibilities would be extremely interesting.

We turn now to the results for the probability distribution of the amplitude of the signal. In Figure 6 the result for Case I is given. The circles give the computed value of the amplitude distribution as obtained from the data. The crosses were obtained from the modified Rayleigh distribution. The value of  $a/R_0$  needed to determine the extent of the modification (see Section II) was obtained as follows. First the value of the ratio of the standard deviation to the mean was taken as calculated from the data; in this case that was found to be 0.28. Then  $a/R_0$  was found from Figure 2 to be 0.44. This value was used to make the plot shown in Figure 6. As mentioned above, the distribution taken from the data is more peaked than the best theoretical distribution, indicating a possible correlation between the noise and the coherent signal, due to phase correlation between the scattered signal and the coherent (or average) signal. Again as has been remarked, the sinusoidal signals would be expected to flatten the distribution. The values for  $a/R_0$  for various times in seconds after 7 A. M. on August 8, are given in Table I.

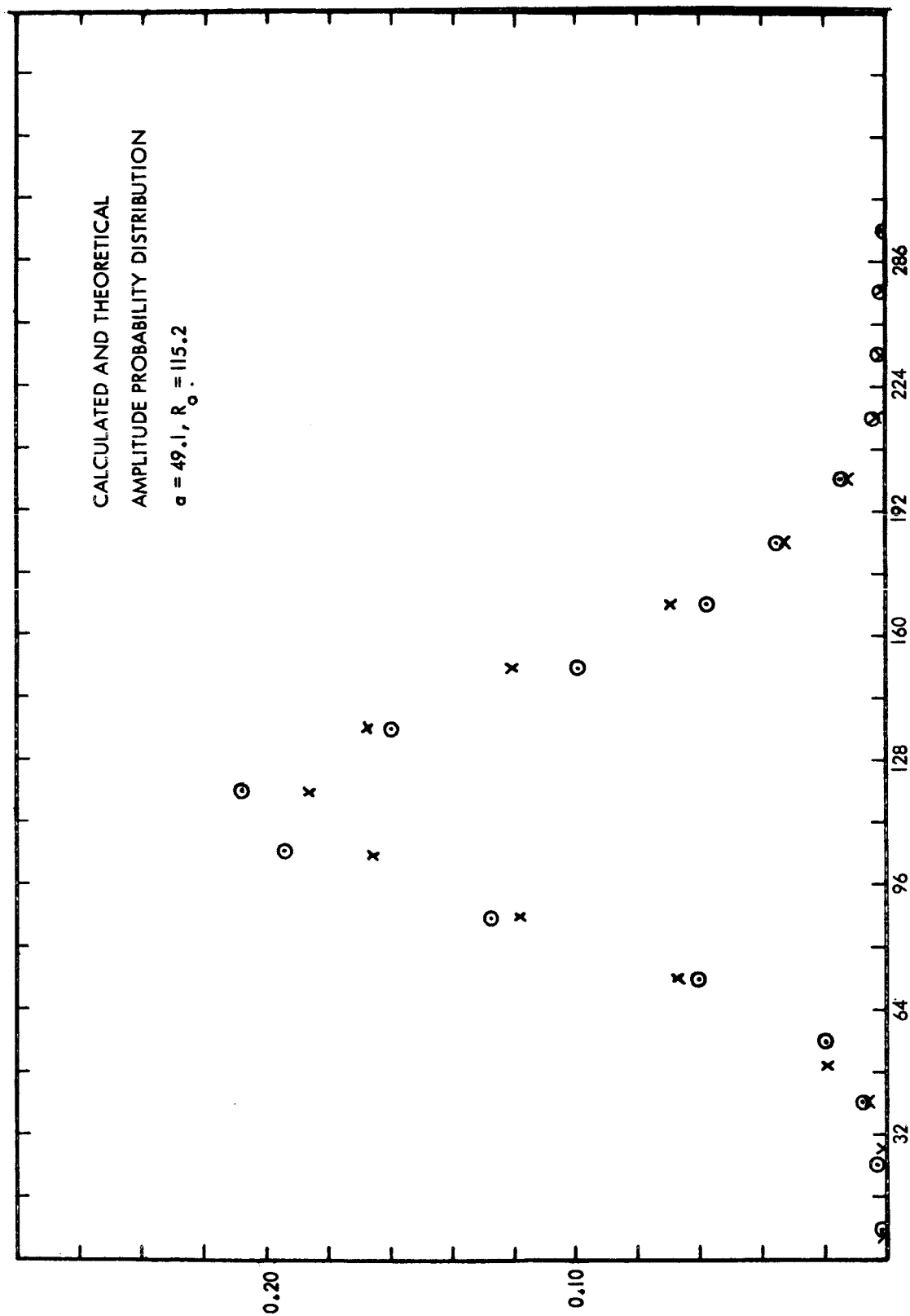


Figure 6. Calculated and Theoretical Amplitude Probability Distribution  
 $a = 49.1, R_0 = 115.2$

TABLE I

	Time	Data Standard Deviation/Mean	$a/R_0$
I.	1794 - 1974	0.28	0.44
	2274 - 2334	0.274	0.41
	2394 - 3054	0.258	0.37
	3174 - 3234	0.455	0.96
II.	3354 - 3774	0.267	0.40

It is difficult to say what is the origin of the large amount of noise observed in the record starting at 3174 seconds. Possibly it is spurious, although there is no real evidence of this. Possibly the ray from satellite to earth was at this time passing through a particularly disturbed region of the ionosphere. Such clouds of disturbance have been reported in the radio astronomical literature.

#### IV. CONCLUSION

The problem of the determination of the cause of the ionospheric disturbances responsible for the signal fluctuations discussed above is a very interesting one. It is possible that these disturbances and the corresponding radio astronomical ones are similar. Differences should however be pointed out. First the periods for astronomical fluctuations are most often reported as minutes, rather than fractions of a second as discussed. Perhaps even more important astronomical fluctuations are usually much smaller than we see here. Possibly this is due to the fact that most such observations are taken at more northerly latitudes. It is known that electron densities at these geographical locations are lower

than nearer the equator.<sup>11</sup> However one of the major outstanding problems for radio astronomers is the cause of the signal fluctuations which they observe. It has been suggested that the cause may be ionospheric turbulence.<sup>12</sup> Unfortunately the Reynold's number in the F layer is far too low, due to the very low density, to expect instabilities and resulting turbulence. In fact experiments<sup>13</sup> involving visual observation of trails left by rockets show that the ionosphere is laminar at altitudes above about 100 miles, the transition occurring quite suddenly. Booker's turbulence suggestion<sup>12</sup> involves regions below the F layer (presumably below 100 miles) in order to meet this difficulty. But then one is faced with electron densities which are very small.

If one rejects turbulence, the question of what other mechanisms are available remains. There is the possibility that acoustic type waves (mechanically coupled waves) excited by Alfven waves generated at great distances from the earth, and presumably arriving from the night side only, may provide an explanation. However there are difficulties, perhaps explainable, such as the expected high attenuation of such waves, in the interesting regions of the ionosphere. Much more work needs to be done, along the lines suggested in earlier parts of this report, before the basic ionospheric mechanism can be said to be determined.

Before closing it should be remarked that satellite signal fluctuations have been found by other investigators.<sup>14</sup> Their conclusions concerning the nighttime occurrence and latitude dependence are in general in keeping with those of this report.

It is a pleasure to acknowledge many helpful discussions with Roger Gore and Drs. S. Altshuler and F. Scarf. The author is indebted to the last named for the ionospheric mechanism suggested above as a tentative explanation of the cause of the observed signal fluctuations.

Space Technology Laboratories, Inc.  
Redondo Beach, California  
November 1962



## FOOTNOTES

1. R. Gore, Space Technology Laboratories, Report No. 8626-6005-RU-000.
2. D. C. Brennan, Some Remarks on Space Propagation, to appear as a chapter in Lectures on Space Communication, A. V. balakrishnan, editor, McGraw-Hill.
3. A recent report, (K. C. Yeh and G. W. Swenson, Journal Geophys. Res. 64, 2281 (1959).) gives direct evidence for this assertion. It was found that satellite signal fluctuation showed a marked reduction when the satellite descended through the Flayer.
4. W. C. Meecham, On Radiation in a Randomly Inhomogeneous Medium, STL Report September 1961.
5. W. C. Meecham, On Sound Propagation in Randomly Inhomogeneous Media, Fourth International Congress on Acoustics, Copenhagen, 21-28 August 1962.
6. J. B. Keller, Proc. of Syrup in Appl. Math., 13, 227 (1962).
7. W. S. Ament, Modification of a Ray-Tracer for Monte Carolo Prediction of Multiple-Scattered Radio Fields, Statistical Methods of Radio Wave Propagation, p. 184, (Pergamon Press, New York, 1960).
8. The corresponding treatment for a vector field is not conveniently available. It would be interesting in particular to have some quantitative knowledge of the statistics of the electromagnetic polarization.
9. W. B. Davenport and W. L. Root, Random Signals and Noise, p. 166, McGraw-Hill Book Company, Inc., New York, 1958.
10. The moments are given by,

$$\langle A^\lambda \rangle = \int_0^\infty A^\lambda P(A) dA.$$

The integrals are given in W. Magnus and F. Oberhettinger, Special Functions of Mathematical Physics, p. 35, Chelsea Publishing Company, New York, 1949.

11. J. W. Wright, A Model of the F Region Above  $h_{\max}$  F2, Journal of Geophys Res., 65, 190, 1960.
12. H. G. Booker, Proc. IRE, January 1958, p. 298.
13. J. E. Blament and C. deJager, Upper Atmospheric Turbulence Determined by Means of Rockets, Journal of Geophys. Res. 67, 3113 (1962).
14. G. S. Kent, J. Atmosph. and Terrestr. Phys., 16, 10 (1959).